MULTIPLE OBJECTIVE OPTIMIZATION DESIGN OF THE MAGNETIC BEARING SUPPORTED ROTORDYNAMIC SYSTEM

A Dissertation

by

WAN ZHONG

Submitted to the Office of Graduate and Professional Studies of
Texas A&M University
in partial fulfillment of the requirements for the degree of

DOCTOR OF PHILOSOPHY

Chair of Committee,	Alan Palazzolo
Committee Members,	Bryan Rasmussen
	Thomas Strganac
	Yong-Joe Kim
Head of Department,	Andreas A. Polycarpou

August 2015

Major Subject: Mechanical Engineering

ABSTRACT

Magnetic bearings have been widely used in turbomachinery field due to their advantages from the non-contact mechanism and the absence of a lubrication requirement. This study focuses on modeling and predicting the rotordynamic and thermal performances of the nonlinear active magnetic bearing supported rotordynamic system with flexible rotor and flexible foundation effects, and then optimizing the design of the magnetic bearing actuator and the control law to achieve the multiple goals simultaneously. Nonlinearities, including the nonlinear magnetic bearing force with respect to the rotor displacement and the control current, the flux saturation, and the power amplifier current and voltage saturation, are analyzed to improve the prediction of the rotordynamic system. Two-dimensional finite element method is used to determine the temperature distribution on the actuator and predict the hot spot temperature during rotor steady state operations. A multiple-input multiple-output (MIMO) flexible support model effects on rotordynamic behavior of the system are addressed. Multiple system properties and performances, like the bearing actuator mass, the maximum vibration amplitude, the power loss, and the external static load, are set as goals to be optimized. Genetic algorithms, including Non-dominated Sorting Genetic Algorithm-II (NSGA-II) and Neighborhood Cultivation Genetic Algorithm (NCGA), are selected as the main optimization strategies due to their advantages in solving complicated optimization problems.

DEDICATION

To my parents and sisters for all their love and encouragement.

ACKNOWLEDGEMENTS

I would like to thank my advisor, Dr. Palazzolo, who gave me a lot of guidance, brilliant ideas, encouragements, and support during the years, and who sets an example to me by having a passion for his research and work.

Thank you to my committee members, Dr. Kim, Dr. Strganac, and Dr. Rasmussen, for their guidance and support throughout the course of this research.

Thanks also go to my friends and colleagues and the department faculty and staff for making my time at Texas A&M University a great experience. I also want to extend my gratitude to the Turbomachinery Research Consortium, which financially supported the project.

TABLE OF CONTENTS

Page

Page

Page

LIST OF FIGURES

Page

Page

Page

Page

Page

Page

LIST OF TABLES

Page

1. INTRODUCTION

1.1 Overview

This dissertation presents the optimization design of the active magnetic bearing (AMB) supported rotordynamic system. The first objective of the research is to improve the reliability of the prediction of the rotordynamic performances of the AMB supported system by including a flexible rotor, flexible foundation effects, and system nonlinearities. The second objective is to incorporate the thermal modeling and hot spot temperature prediction into the rotrodynamic analysis, to serve for the high temperature applications of the AMB supported system. The third objective is to optimize the design of this AMB supported system to achieve multiple system performance related goals simultaneously. Genetic Algorithm, an optimization algorithm inspired by the biological processes of genetics and evolution, is selected to simultaneously optimize the design objectives. Finite Element Method (FEM) is used to determine the thermal distribution on the actuator and find the hot spot temperature when the rotor is in steady state operation. The dynamic flexibility of the support is described by the Frequency Response Function Matrix (FRFM), and its effect on the rotordynamic behavior of the AMB supported system is studied. A two-controller strategy, which utilize a set of controller parameters at startup stage, and another set of controller parameters at the steady state operation of the rotor, is demonstrated to give a further optimized AMB supported system with smaller actuator mass and lower vibration amplitude without too much sacrifice in the power loss.

1.2 Contributions and Novelties

The contributions and novelties of the research include:

1) Nonlinear magnetic bearing analysis and simulation. While most of the current researches on magnetic bearing system use a linear model, which linearize the magnetic bearing force into a bearing displacement stiffness and a bearing current stiffness, our current study greatly improves the prediction of the magnetic bearing system rotordynamic performances by including the system nonlinearities. Firstly, the magnetic bearing force is nonlinear with respect to the rotor displacement and the control current, and the linearization of the force induces error into the accuracy of the prediction. Secondly, the magnetic bearing material is nonlinear, which means that the relationship between the magnetic flux density B and the magnetic field H is nonlinear and the maximum achievable magnetic flux intensity is limited. Thirdly, there are voltage and current limits on the power amplifier output voltage and current, which is called power amplifier voltage saturation and current saturation. Without considering the saturation from the amplifier, the control law might generate a control signal demanding a power amplifier voltage or current exceeding its limits, and the predicted magnetic bearing force cannot actually be achieved. Besides, the nonlinear catcher bearings, which are installed to prevent the unexpected contact between the rotor and the magnetic bearing stator in the cases of overload or magnetic bearing failure, induce another nonlinearity into the system.

2) Rotordynamic stability, harmonic response to unbalance, and transient analysis with the effects of the cross-coupled MIMO dynamic flexibility in the foundation. In this study, a state space representation form of the magnetic bearing support with dynamic flexibility is developed, and assembled with the equation of motion of the rotor, to predict the rotordynamic behavior under the effects of the flexibility of the support.
3) Numerical analysis and optimization of the power losses of the bearing-rotor system in the dynamic process. Most of the power losses studies of the magnetic bearing system focus on heteropolar magnetic bearing system, calculating the iron loss caused by the bias current only, ignoring the control current induced iron loss. This study numerically determines the power loss of the AMB system, for both the heteropolar magnetic bearing actuators and the homopolar magnetic bearing actuators. Two dynamic process of the rotor, one of the levitation in which the rotor is lifted from an initial position, and the other of the rotor steady state operation with rotor unbalance induced force, are simulated. The study detects the flux intensity and the control current when the system is in the steady state operation, and then numerically determines the power losses of the AMB system from both the magnetic bearing stator and the spinning rotor. The obtained power loss is set one of the minimization objectives for the system optimization.
4) The 2D thermal model is coupled into the spinning rotor, and the hot spot temperature can be detected to prevent the bearing from too high temperature. In

the steady state operation of the rotor, the thermal field of the actuator is determined numerically with the two dimensional finite element method (FEM). The highest temperature, which is called the hot spot temperature, is detected and set as a constraint of the designed system.

5) The bandwidth limits of the electronics, including the sensors, controllers, power amplifiers and other compensators are taken into consideration.
6) The optimization of the homopolar magnetic bearing actuator and the controller simultaneously is unique. Most of the current magnetic bearing system optimizations are plant based optimization, which focus on the optimization of the actuator parameters only. In this study, the closed loop, including the actuator and the controller, are optimized simultaneously. The optimization detects and tunes the controller of the system automatically. The optimization techniques solve the design problem of the homopolar magnetic bearings, which is one of the main challenges facing homopolar magnetic bearings due to their complex geometry.
7) Numerically calculate the vibration amplitude and determine the stability margin of the AMB supported system according to the API617/ISO14839 standard. In ISO 14839, stability margin are experimentally determined without numerical analysis. In this study, open loop transfer function and sensitivity function of the system, including the rotor, the sensors, the controllers, the power amplifiers and the actuators can be numerically determined. The system stability margin can be determined and checked with the standards.

1.3 Present Status of Magnetic Bearing

Magnetic bearings have various advantages over conventional bearings like fluid film bearing or rolling bearing. Its non-contact nature makes magnetic bearing has the minimal friction and wear, which allows magnetic bearings have higher efficiency and higher running speeds of the rotor. Since no lubrication is required in AMB system, there is no oil contamination. As a result, magnetic bearings can be used in harsh environment, including extremely high and low temperatures, vacuums, gravity free conditions, and subsea environments. High temperature magnetic bearings have been used on aircrafts, jet engines and drilling equipment, with a temperature limit up to 538°C, while current roller bearings and squeeze dampers are limited to 260°C. Another difference between magnetic bearings and conventional bearings is that magnetic bearings are active controlled and have high static stiffness, which can provide precise control of the nominal shaft center.

Due to these advantages, the use of magnetic bearings increases dramatically in a wide range of applications, for example, energy storage flywheels, turbo-molecular vacuum pumps, high speed milling machines, turbo expanders, oil free motors, aircraft gas turbine engines, and so on. For example, NASA Glenn Research Center has developed a high temperature, high load magnetic bearing system for aircraft engine, which can be operated under a temperature as high as 1000 degrees Fahrenheit. In the recent years, magnetic bearings attract further more attention for the successful application in the subsea area. The compressors and high speed motors of the Åsgard Subsea Gas Compression System, which is expected to start to operate in 2015, uses

magnetic bearing systems for their oil-free, frictionless, high efficiency, long service life and low maintenance properties in the remote conditions on the seabed floor. High-performance, high-speed magnetic bearings have been applied to aerospace and defense applications where precision is vital and operating conditions challenging. For example, magnetic bearings are applied to neutron choppers, which operate in vacuum and speed up to 36,000 rpm.

However, magnetic bearings have their limits. Here we listed the main concerns about magnetic bearings.

1) Magnetic bearings load capacity and specific load are limited by the saturation in magnetic material. The best magnetic conducting medium (iron cobalt alloy) has a saturation flux intensity of about 2.3 Tesla.
2) Control of many modes, even beyond the operating speed range, is required.
3) Time, cost, and advanced knowledge of both mechanical engineering and electrical engineering are required for the magnetic bearing/ rotor and control system design.
4) Catcher bearings have to be installed near the magnetic bearing to avoid unexpected contact between the rotor and the bearing stator in cases of overload or magnetic bearing failure from the controller or power supply.[1]

Many of these challenges of magnetic bearings are in the design stage, so optimization is significant to design a compact, high efficient and reliable magnetic bearing system.

In the research of the nonlinear magnetic bearings, Chinta and Palazzolo[2] studied the nonlinear forced response with two methods: one using imbalance force, and the other using non-imbalance harmonic force. The periodic motions' local stability and bifurcation behavior are obtained by Floquet theory. Ahmed and Ouladsine [3] proposed a nonlinear model for magnetic levitation systems and validated with experimental measurements. A nonlinear control law based on differential geometry was synthesized with the model. Kang and Palazzolo [4] analyzed the nonlinear dynamics of a permanent magnet-biased homopolar magnetic bearing system with a flexible rotor. They proposed a modified Langmuir method with the correction terms for the weak flux region to form an analytical model of the experimental magnetization curve (BH curve) of Hiperco 50. The response of the rotor-bearing system showed that limit cycle stability can be achieved due to the magnetic flux saturation or current saturation in the amplifier.

The genetic algorithms have been used in the optimization design of the heteropolar magnetic bearings. Carlson-Skalak and Maslen et al. [5] presented the single objective optimization design of HEMB actuator using genetic algorithms. The concept of catalog selection was used, which made the optimization more amenable to commercial design. Shelke et al. [6]used multi-objective genetic algorithms to optimize both the actuator weight and the copper power loss in the coil of the HEMB actuator. They included only the ohmic loss in the coil as the power loss and set it as one of the two optimization goals. Chang et al. [7] designed the HEMBs with minimum volume according to the static load, dynamic load and the equivalent stiffness with genetic algorithms. In the research of active magnetic bearing supported systems, genetic

algorithms have also been applied to optimize the control strategies of the systems. Schroder et al. [8] used the genetic algorithms to optimization the robust control strategy of the 5-axis controlled HEMBs supported rotordynamic system with both radial bearing and axial bearing. Chen and Chang et al. [9-11] optimized the PID controller of the HEMBs system. Jastrzębski et al. [12] discussed a closed-loop centralized optimal position control strategy for a multi-input multi-output HEMBs system. The controller parameters are optimized with genetic algorithms and the system performance was compared with the one controlled by the classical PID controller. However, these optimizations of the controllers did not address the design of the magnetic bearing actuator. Other than genetic algorithms, Hsiao et al. [13] used the goal programming as the search method and finite difference to calculate the objectives and constraints in the optimization design of the HEMB supported rotor-bearing system controlled with a PD controller.

In the optimization design of HOMB, Lee et al. [14] studied the performance limits of the permanent magnet biased HOMB, including the maximum static bearing force, the force slew rate, and the displacement sensitivity. Fan et al. [15]proposed design procedures for a type of permanent magnet biased HOMB in the rotor-bearing system. However, the procedure simply searches for feasible solutions without minimizing any objective functions. Optimization of the HOMB design remains a novelty due to the complexity of the HOMB actuator construction, the additional flux circuit due to the permanent magnet bias flux and the more complex flux path of the electromagnetic induced flux relative to a HEMB design.

Various multi-objective genetic algorithms (MOGAs) techniques have been developed by previous researchers. The Non-dominated Sorting Genetic Algorithm-II (NSGA-II) optimization techniques by Deb et al. [16] have been applied to many different design problems and work as a standard that other algorithms are compared with. Strength Pareto Evolutionary Algorithm (SPEA) by Zitzler and Thiele [17] also received a lot of attention because of its simplicity and effectiveness. Neighborhood Cultivation Genetic Algorithms (NCGA) by Watanabe et al. [18], which are developed based on NSGA-II and demonstrated to have better solutions than NSGA-II, have also been widely used. Other than genetic algorithms, other multiple objective algorithms have also been developed, for example Multi-objective Particle Swarm Optimization (MOPSO) by Coello et al. [19], Multi-objective Simulated Annealing (MOSA) [20] , etc. MOPSO has been used to solve various optimization problems. However, other than the simplicity of programming, there is no significant of the MOPSO over genetic algorithms. If given enough time, genetic algorithms demonstrate better Pareto solutions than MOSA. But MOSA is faster than genetic algorithms in speed, so given the same time, MOSA gives better results.

1.4 Practical Significance

The standard rotordynamic code for magnetic bearing systems is linear based, which does not include saturation feature of the power amplifier, and there is no bandwidth limitation on the electronics. Besides, the linear magnetic bearing software does not have the model of the actuator. It uses the position stiffness and the current

stiffness to estimate the actuator generated magnetic force, while the magnetic bearing force is actually nonlinear with respect to the rotor displacement and control current. In this study, the full nonlinear analysis of the magnetic bearing supported system with flexible rotor and flexible support, considering saturation features of the system components (power amplifier and actuator), the bandwidth of the electronics, and with the modeling of the actuator, is conducted. The nonlinear analysis of the magnetic bearing- rotor system improves the prediction of system performance.

The optimization design of the magnetic bearing system solved two of the main challenges of the magnetic bearings, one of the actuator design, and the other of the control system design. The design of the magnetic bearing system is very complicated, with the following considerations:

1) The optimization involves large number of design variables, coming from both the actuator dimension parameters and controller gains.
2) Several objectives are optimized simultaneously in a multi-objective optimization. Trade-offs among the objectives should be balanced. “Good” solutions need to be defined for all the objectives and selected from the pools.
3) The constraints of the system should be taken carefully to avoid any physical confliction, to supply enough dynamic load capacity, to suppress excessive vibration, to prevent too high temperature, to satisfy the ISO/API standards, and a lot of others to consider to make the design really practical. Some of these constraints might be computationally expensive, especially in the optimization iteration. For example, the hot spot temperature as a constraint may involve a

thermal modeling of the system. The dynamic load capacity and vibration amplitude require a transient simulation of the rotor motion.

4) The system matrix equation is complicated, which describes not only the motion of the rotor, but also the flexible support, the nonlinear actuator, and the electronics with finite bandwidth. The system matrix equation is nonlinear with large dimension.
5) The initial solutions of the optimization might be mostly infeasible, since it is time consuming to find a set of feasible solutions as initial solutions to start the optimization. For this type of complicated optimization, randomly selected initial solutions from a range are an easy way to start the optimization. However, these randomly generated solutions are possibly infeasible, especially for nonlinear problems.

All these make the optimization of the AMB system a complicated task, which requires complex numerical algorithms to solve.

2. SYSTEM COMPONENTS AND OPTIMIZATION ALGORITHMS

The main components in a closed loop controlled AMB system include a rotor, sensors, controllers, power amplifiers, and magnetic bearing actuators. Figure 1 depicts a simplified closed loop of the system. A sensors measure the displacement of the rotor from its reference position; a PD controller receives the sensor signal, compares the signal to a desired sensor signal according to the target rotor position, calculates corrections required to return to the desired position, and derives a control signal accordingly; a power amplifier transforms this control signal into a control current; and the control current generates magnetic forces in the magnetic bearing actuator to suspend the rotor to the desired position.

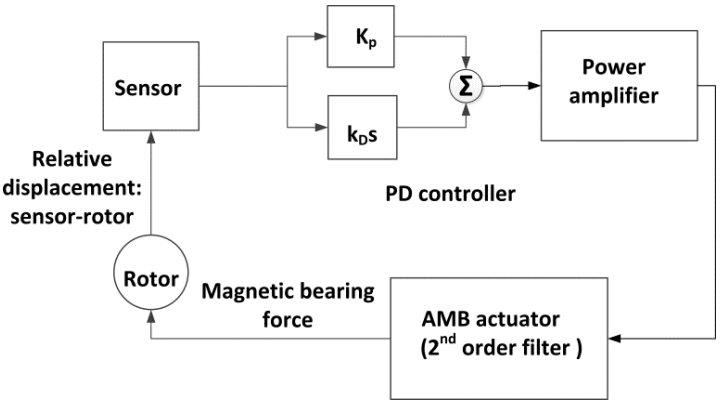

Figure 1 Simplified control loop and main components of the HOMB supported rotor system

Two representative types of radial magnetic bearings, one of the heteropolar type and the other of the homopolar type, are introduced in this section. Simplified one

dimensional magnetic circuit, and the calculation and linearization of the magnetic bearing forces are presented. This section also talks about the modeling of the flexible rotor with the finite element method (FEM). Other system components, including the sensors, controllers, and power amplifiers, are introduced.

2.1 Radial Magnetic Bearing Actuators

Generally, radial magnetic bearings are classified into two groups based on the structural configurations: heteropolar magnetic bearings (HEMB) and homopolar magnetic bearings (HOMB). In the HEMB bearings, the magnetic poles alternate in polarity in the plane perpendicular to the rotor axis, while in the HOMB, all the poles in the given rotational plane have the same polarity, as shown in Figure 2 and Figure 3. In Figure 2 and Figure 3, a catcher bearing is installed as backup bearing next to the magnetic bearing. In the figures, l_g is the air gap clearance of the magnetic bearing, C_r is the catcher bearing clearance, N represents the north pole, and S represents the south pole.

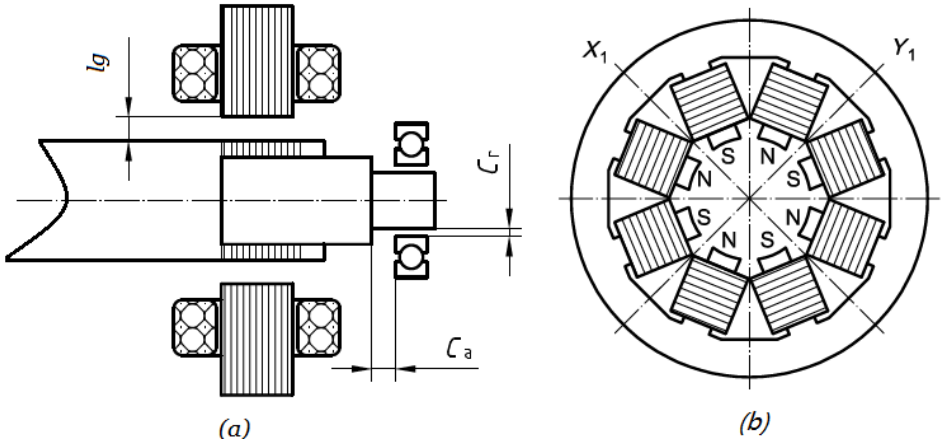

Figure 2 Heteropolar active magnetic bearing with alternating poles

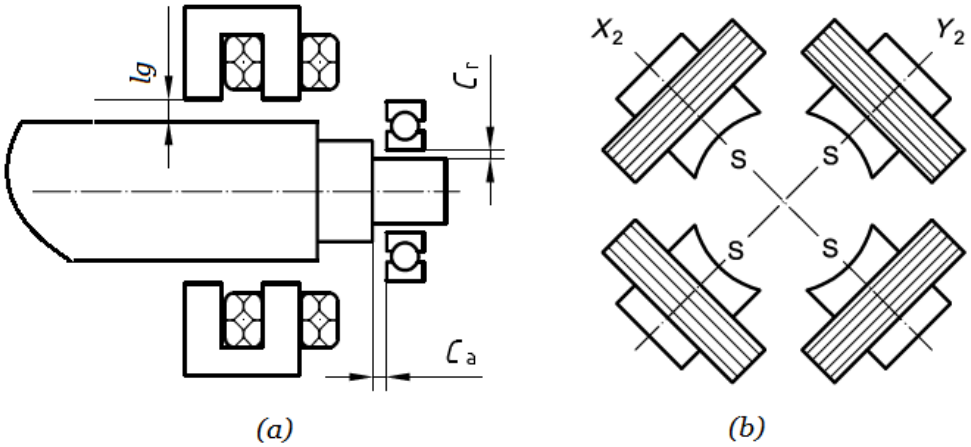

Figure 3 Homopolar radial magnetic bearing actuator

In general, the heteropolar magnetic bearings have the simpler structure and lower cost, thus are the most commonly used ones. Homopolar magnetic bearings have a much more complicated structure with two stators and in most cases permanent magnets, and thus are more expensive. However, the homopolar magnetic bearings have much lower power loss due to the configurations with less field variation around the

circumference of the rotor. [21] In vacuum applications, power loss is a major concern since there is no convection or conduction that all the heat on the rotor must be dissipated by radiation to the housing. As a result, homopolar magnetic bearings have been used for vacuum applications such as satellites.

2.1.1 Homopolar radial magnetic bearing actuator

HOMB bearings are mostly used with permanent magnets to supply bias flux. In this study, the permanent magnet biased 4 poles HOMB actuator and the magnified coils are displayed in Figure 4.

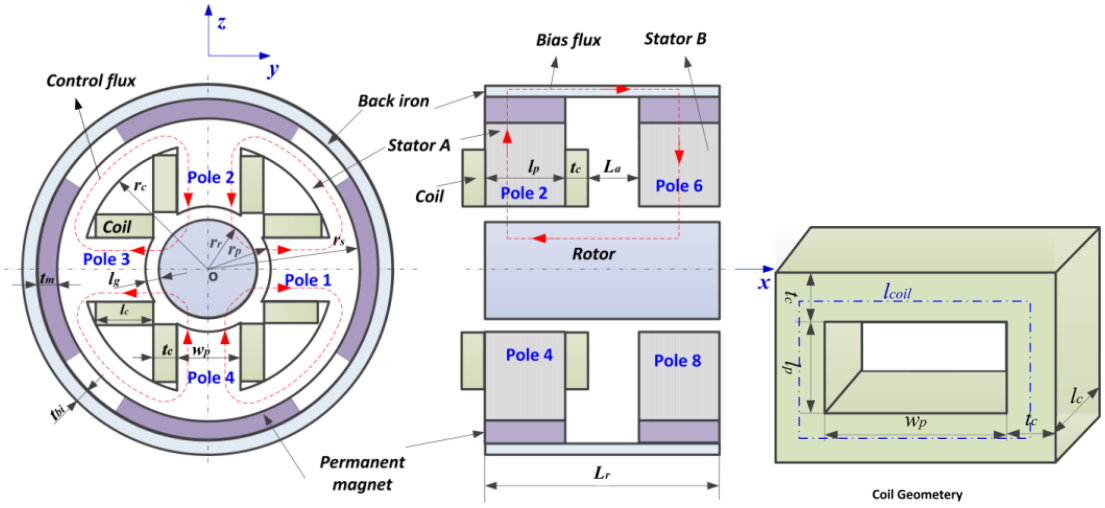

Figure 4 Homopolar radial magnetic bearing actuator (a) and the magnified coil geometry (b)

Stator A is an active plane with coils on each of the 4 active poles, including pole 1 in y-axis direction, pole 2 in z-axis direction, pole 3 in negative y-axis direction, and

pole 4 in negative z-axis direction. The y-axis control current i_{cy} goes through the coils on pole 1 and pole 3, and the z-axis control current i_{cz} goes through the coils on pole 2 and pole 4. Control currents on the stator A generate control flux that conducts radially. Stator B is a dead plane without coils, thus there is no control flux in the radial directions on stator B. There are also 4 poles on the stator B, including pole 5 in y-axis direction, pole 6 in z-axis direction, pole 7 in negative y-axis direction, and pole 8 in negative z-axis direction. A back iron ring that conducts the bias flux axially is used. In the Cartesian coordinate system, the x-axis direction indicates the axial direction of the rotor, and the negative z-axis direction indicates the direction of the static load induced by weight. The radial magnetic bearings generate radial forces in y- and z- axis directions. The definitions of the variables in Figure 4 are as follows: l_g - air gap length, t_c -thickness of the coil, l_c -radial length of the coil, r_c -coil space radius, r_s - radius of the stator, r_r -radius of the rotor, r_p - pole tip radius, t_{bi} - thickness of the back iron, w_p - width of the pole, t_m -thickness of permanent magnet, L_r - length of the rotor under the magnetic bearing, l_p - length of the pole along the rotor axis, L_a - length of the gap between two stators. The thickness of the coil is

$$t_c = r_p \tan(\pi / n_p) - w_p / 2 \tag{1}$$

where n_p is the number of poles on each of the stator. In this case, $n_p = 4$. The length of rotor under the bearing L_r is expressed by

$$L_r = (2l_p + t_c) / (1 - \gamma_a) \tag{2}$$

where γ_a is the ratio of the length of empty space to length of rotor under the bearing. In this model,

$$\gamma_a = L_a / L_r = 0.1 \tag{3}$$

The equivalent electric circuit of the HOMB bearing is shown in Figure 5. The model is based on the following assumptions: 1) No flux leakage; 2) The permeability of the pole, the rotor, the stator and the back iron is much bigger compared with the air, thus the reluctances from the pole, rotor and the back iron can be ignored compared with the air reluctance; 3) The cross sectional area of the flux path in the pole is the same with the air gap area.

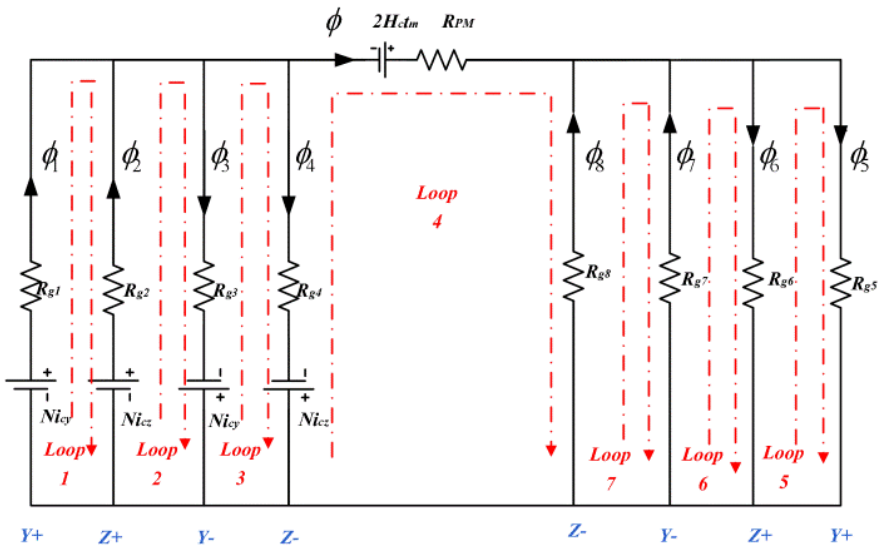

Figure 5 1D magnetic circuit of the homopolar magnetic bearing actuator

According to the Ampere's Law, the line integral of the magnetic field around a closed loop is proportional to the electric current flowing through the loop:

$$
\begin{aligned}
&\text{Loop1: } H_{g1}l_{g1} - H_{g2}l_{g2} = N(i_{cy} - i_{cz}) \\
&\text{Loop2: } H_{g2}l_{g2} + H_{g3}l_{g3} = N(i_{cy} + i_{cz}) \\
&\text{Loop3: } H_{g3}l_{g3} - H_{g4}l_{g4} = N(i_{cy} - i_{cz}) \\
&Loop4: H_{g4}l_{g4} + H_{g8}l_{g8} - R_{pm}\phi = Ni_{cz} - 2H_c t_m \\
&Loop5: H_{g5}l_{g5} - H_{g6}l_{g6} = 0 \\
&Loop6: H_{g6}l_{g6} + H_{g7}l_{g7} = 0 \\
&Loop7: H_{g7}l_{g7} - H_{g8}l_{g8} = 0 \\
&flux: \phi = \phi_1 + \phi_2 - \phi_3 - \phi_4 = \phi_5 + \phi_6 - \phi_7 - \phi_8
\end{aligned}
\tag{4}
$$

where H_{gi} is the magnetic field intensity of the i^{th} air gap for *i=1~6*; l_{gi} is the air gap length of the i^{th} pole with the rotor centered for *i=1~6*; R_{gi} is the air gap length of the i^{th} pole with the rotor centered; ϕ_i is the flux in the i^{th} air gap; H_c is the coercive field intensity of permanent magnet; t_m is the thickness of the permanent magnets, R_{pm} is the total reluctances of the two magnets in a flux loop.

For linear analysis, the Ampere's Law can be written in the form of

$$H_{gi}l_{gi} = R_{gi}\phi_i \tag{5}$$

for $i = 1, 2, 3, ..., 8$. The equation (4) can be written into the matrix form as:

$$
\begin{pmatrix}
R_{g1} & -R_{g2} & 0 & 0 & 0 & 0 & 0 & 0 \\
0 & R_{g2} & R_{g3} & 0 & 0 & 0 & 0 & 0 \\
0 & 0 & R_{g3} & -R_{g4} & 0 & 0 & 0 & 0 \\
-R_{pm} & -R_{pm} & R_{pm} & R_{pm}+R_{g4} & 0 & 0 & 0 & R_{g8} \\
0 & 0 & 0 & 0 & R_{g5} & -R_{g6} & 0 & 0 \\
0 & 0 & 0 & 0 & 0 & R_{g6} & R_{g7} & 0 \\
0 & 0 & 0 & 0 & 0 & 0 & R_{g7} & -R_{g8} \\
1 & 1 & -1 & -1 & -1 & -1 & 1 & 1
\end{pmatrix}
\cdot
\begin{pmatrix}
\phi_1 \\ \phi_2 \\ \phi_3 \\ \phi_4 \\ \phi_5 \\ \phi_6 \\ \phi_7 \\ \phi_8
\end{pmatrix}
=
\begin{pmatrix}
N(i_{cy} - i_{cz}) \\ N(i_{cy} + i_{cz}) \\ N(i_{cy} - i_{cz}) \\ Ni_{cz} - 2H_c t_m \\ 0 \\ 0 \\ 0 \\ 0
\end{pmatrix}
\tag{6}
$$

where

$$R_{g1} = R_{g5} = \frac{l_g - y}{\mu_0 A_g}, R_{g2} = R_{g6} = \frac{l_g - z}{\mu_0 A_g}$$
$$R_{g3} = R_{g7} = \frac{l_g + y}{\mu_0 A_g}, R_{g4} = R_{g8} = \frac{l_g + z}{\mu_0 A_g} \quad (7)$$

and

$$R_{pm} = \frac{2t_m}{\mu_{pm} A_m} \quad (8)$$

where μ_{pm} is the permeability of the permanent magnet, A_m is the cross sectional area of the permanent magnet, $2t_m$ indicates the total thickness of the two permanent magnets in one flux loop. By solving equation (6), the flux ϕ_i in each pole can be obtained and (y, z) is the displacement of the rotor. Then the flux intensity in each pole ignoring the leakage can be determined in the form of

$$B_{gi} = \frac{\phi_i}{A_g} \quad (9)$$

The Maxwell stress tensor formula determines the force exerted by the magnetic field in the form of

$$F_{MBi} = \frac{{B_{gi}}^2 A_g}{2\mu_0} \quad (10)$$

The total magnetic bearing force is obtained from (6), (9), and (10) as:

$$F_{MBy} = \frac{A_g}{2\mu_0}(B_{g1}{}^2 - B_{g3}{}^2 + B_{g5}{}^2 - B_{g7}{}^2)$$
$$F_{MBz} = \frac{A_g}{2\mu_0}(B_{g2}{}^2 - B_{g4}{}^2 + B_{g6}{}^2 - B_{g8}{}^2) \tag{11}$$

Linearize the force and expression for the centered rotor case and define the position stiffness K_p and current stiffness K_i as

$$K_{py} = \left.\frac{\partial F_{MBy}}{\partial y}\right|_{icy=0,y=0}, \quad K_{pz} = \left.\frac{\partial F_{MBz}}{\partial z}\right|_{icz=0,z=0}$$
$$K_{iy} = \left.\frac{\partial F_{MBy}}{\partial i_{cy}}\right|_{icy=0,y=0}, \quad K_{iz} = \left.\frac{\partial F_{MBz}}{\partial i_{cz}}\right|_{icz=0,z=0} \tag{12}$$

In this case, due to the symmetry of the actuator, $K_{py} = K_{pz} = K_p$ and $K_{iy} = K_{iz} = K_i$. The linearized force expression for the centered rotor case is:

$$\begin{Bmatrix} F_{MBy} \\ F_{MBz} \end{Bmatrix} = K_i \begin{Bmatrix} i_{cy} \\ i_{cz} \end{Bmatrix} + K_p \begin{Bmatrix} y \\ z \end{Bmatrix} \tag{13}$$

where the position and current stiffness are:

$$K_p = \frac{(t_m H_c)^2}{A_P \mu_0 l_g [l_g / (2\mu_0 A_P) + R_{pm}]^2} \tag{14}$$

$$K_i = \frac{2N t_m H_c}{A_P \mu_0 [(l_g / \mu_0 A_P)^2 + 2R_{pm} l_g / \mu_0 A_P]} \tag{15}$$

For nonlinear analysis, in the stator and the rotor, the saturation of the ferromagnetic core material is counted and the nonlinear magnetization B-H curve is approximated by a piece-wise B-H curve

$$B=\begin{cases} -B_2 & H<-(\dfrac{B_2-B_1}{\mu_2}+\dfrac{B_1}{\mu_1}) \\ -B_1+(H+\dfrac{B_1}{\mu_1})\mu_2 & -(\dfrac{B_2-B_1}{\mu_2}+\dfrac{B_1}{\mu_1})\le H<-\dfrac{B_1}{\mu_1} \\ \mu_1 H & -\dfrac{B_1}{\mu_1}\le H<\dfrac{B_1}{\mu_1} \\ B_1+(H-\dfrac{B_1}{\mu_1})\mu_2 & \dfrac{B_1}{\mu_1}\le H<\dfrac{B_2-B_1}{\mu_2}+\dfrac{B_1}{\mu_1} \\ B_2 & H\ge\dfrac{B_2-B_1}{\mu_2}+\dfrac{B_1}{\mu_1} \end{cases} \tag{16}$$

where $\mu_1 = 0.0006285(\text{H/m})=500\mu_0$, $\mu_2 = 0.00005028(\text{H/m})=4\mu_0$ are the magnetic permeability in the ferromagnetic core material, $B_1 = 2.0Tesla, B_2 = 2.3Tesla$. The curve fitted B-H curve is shown in Figure 6.

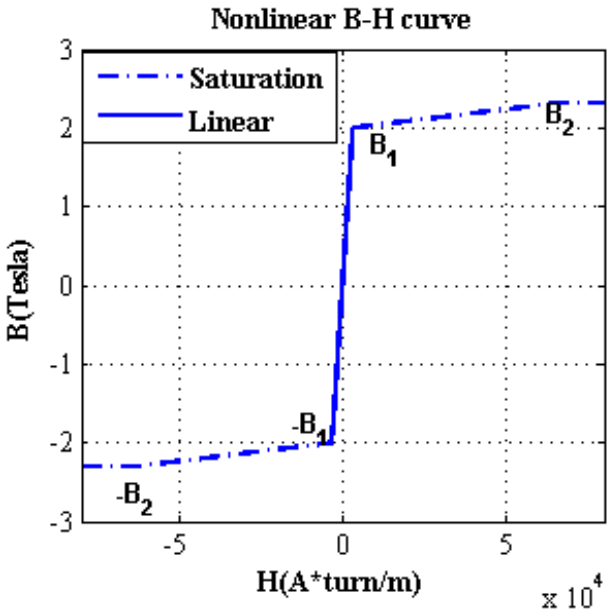

Figure 6 Piece-wise B-H Curve of the ferromagnetic core material in the stator and the rotor

By solving equation (4) and (16), the flux intensities in each of the pole can be obtained, and thus the magnetic bearing force can be obtained by equation (11).

2.1.2 Heteropolar magnetic bearing actuator

Figure 7 shows an 8-pole heteropolar magnetic bearing actuator with alternating configuration (NSNSNSNS) used in the optimization design. The flux loops clearly shows the alternation of the polarities in the poles. The 2D FEM thermal analysis is based on the assumption that the flux fringing and leakage are neglected and the flux is constrained in the radial direction, which means that there is no flux in the axial direction and that the temperature is constant along the axial direction.

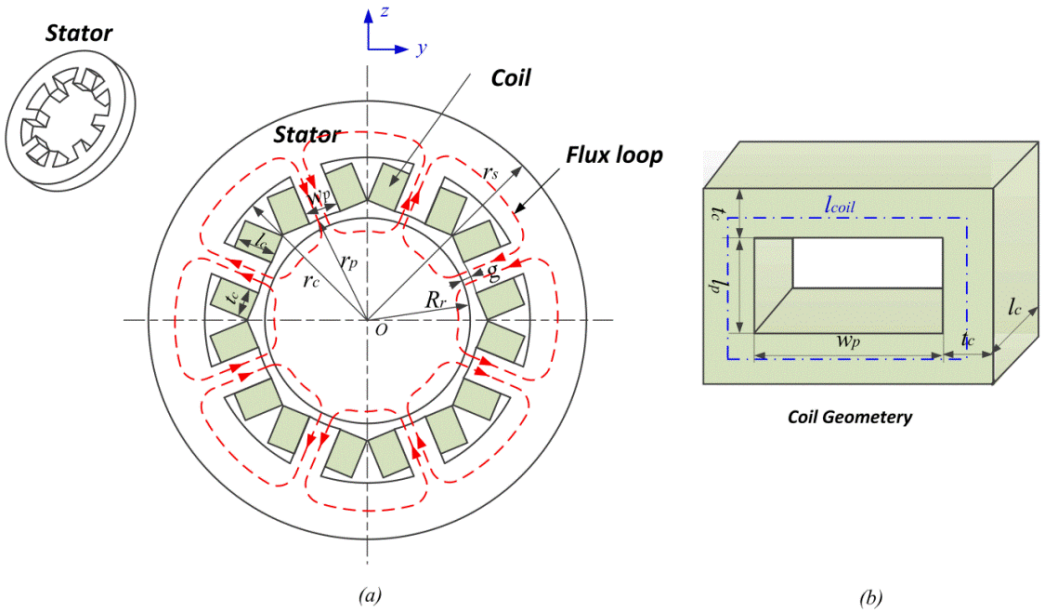

Figure 7 8-pole magnetic bearing stator (a) and exaggerated coil geometry (b)

Magnetic bearings operate in accordance with Ampere's law, Gauss's law, Faraday's law and constitutive relations. Application of Ampere's law to the flux paths yields

$$H_{si}L_{si} + H_{ri}L_{ri} + 2H_{gi}L_{gi} = N(I_b + i_{ci}) \tag{17}$$

where $i = 1, 2, 3, 4$ for the 4 flux paths, H_{si}, H_{ri} and H_{gi} are the magnetic field intensity in the stator, rotor, and air gap of the i^{th} flux path loop, L_{si}, L_{ri} and L_{gi} are the flux path length in the stator, rotor and air gap of the i^{th} flux path loop, I_b is the bias current in the coil, i_{ci} is the control current in the coil of the i^{th} flux path loop, N is the number of the coil turn.

For linear analysis, in the air gap, the magnetic flux intensity B_{gi} and flux field density H_{gi} are related by the constitutive law:

$$B_{gi} = \mu_0 H_{gi} \tag{18}$$

where $\mu_0 = 4\pi \times 10^{-7} (H/m)$ is the permeability of the free space.

In the stator and rotor, same law applies:

$$B_{si} = \mu_{si} H_{si} \tag{19}$$

$$B_{ri} = \mu_{ri} H_{ri} \tag{20}$$

Leakage is ignored so that flux is conserved around the loop yielding:

$$\phi_i = B_{si}A_{si} = B_{ri}A_{ri} = B_{gi}A_{gi} \tag{21}$$

where A_{si}, A_{ri}, A_{gi} represent the cross sectional area of the i^{th} flux path in the stator, the rotor and the air gap respectively. Then the equation (17) becomes

$$(R_{si} + R_{ri} + 2R_{gi})\phi_i = N(I_b + i_{ci}) \tag{22}$$

where R_{si}, R_{ri}, R_{gi} are the reluctances in the stator, rotor and air gap respectively and are defined by

$$R_{si} = \frac{L_{si}}{\mu_{si} A_{si}}, R_{ri} = \frac{L_{ri}}{\mu_{ri} A_{ri}}, R_{gi} = \frac{L_{gi}}{\mu_{gi} A_{gi}} \tag{23}$$

where A_{si}, A_{ri}, A_{gi} are the flux path area in the stator, rotor and air gap in the i^{th} flux path loop. By solving equation (22), the fluxes can be obtained and are then utilized to determine the x- and y- direction magnetic bearing forces.

$$F_i = \frac{(d_B \phi_i)^2}{\mu_0 A_{gi}}, i = 1,2,3,4 \tag{24}$$

$$F_{MBx} = F_1 - F_3, F_{MBy} = F_2 - F_4 \tag{25}$$

where the flux derate factor d_B accounts for leakage and fringing effects and is typically taken as about 0.85.

For the 8-pole case,

$$\begin{aligned} F_{MBx} &= \frac{{d_B}^2 N^2}{\mu_0 A_g} \left(\frac{(I_b + i_{cx})^2}{(R_s + R_r + 2\frac{l_g - x}{\mu_0 A_g})} - \frac{(I_b - i_{cx})^2}{(R_s + R_r + 2\frac{l_g + x}{\mu_0 A_g})} \right) \\ F_{MBy} &= \frac{{d_B}^2 N^2}{\mu_0 A_g} \left(\frac{(I_b + i_{cy})^2}{(R_s + R_r + 2\frac{l_g - y}{\mu_0 A_g})} - \frac{(I_b - i_{cy})^2}{(R_s + R_r + 2\frac{l_g + y}{\mu_0 A_g})} \right) \end{aligned} \tag{26}$$

Linearization of the magnetic bearing force at the centered position and when there is no control current $x=0, y=0, i_{cx}=0, i_{cy}=0$ yields,

$$\begin{aligned} F_{MBx} &= K_{px}x + K_{ix}i_{cx} \\ F_{MBy} &= K_{py}x + K_{iy}i_{cy} \end{aligned} \tag{27}$$

where

$$\begin{aligned} K_{px} = K_{py} &= \frac{{d_B}^2 N^2}{\mu_0 A_g} \frac{4I_b}{(R_s + R_r + 2\frac{g}{\mu_0 A_g})^2} \\ K_{ix} = K_{iy} &= (\frac{d_B N}{\mu_0 A_g})^2 \frac{8{I_b}^2}{(R_s + R_r + 2\frac{g}{\mu_0 A_g})^3} \end{aligned} \tag{28}$$

For nonlinear analysis, in the stator and the rotor, the saturation of the ferromagnetic core material is counted and the nonlinear magnetization B-H curve is approximated by a piece-wise B-H curve

$$B = \begin{cases} -B_2 & H < -(\frac{B_2 - B_1}{\mu_2} + \frac{B_1}{\mu_1}) \\ -B_1 + (H + \frac{B_1}{\mu_1})\mu_2 & -(\frac{B_2 - B_1}{\mu_2} + \frac{B_1}{\mu_1}) \le H < -\frac{B_1}{\mu_1} \\ \mu_1 H & -\frac{B_1}{\mu_1} \le H < \frac{B_1}{\mu_1} \\ B_1 + (H - \frac{B_1}{\mu_1})\mu_2 & \frac{B_1}{\mu_1} \le H < \frac{B_2 - B_1}{\mu_2} + \frac{B_1}{\mu_1} \\ B_2 & H \ge \frac{B_2 - B_1}{\mu_2} + \frac{B_1}{\mu_1} \end{cases} \tag{29}$$

where $\mu_1 = 0.0006285(\text{H/m}) = 500\mu_0$, $\mu_2 = 0.00005028(\text{H/m}) = 4\mu_0$ are the magnetic permeability in the ferromagnetic core material, $B_1 = 2.0 Tesla, B_2 = 2.3 Tesla$. By solving

(29) and (17), the flux intensities in the poles can be obtained, and then the magnetic bearing forces can be determined by equation (21) and (24).

2.2 Finite Element Model of the Flexible Rotor

A flexible rotor has a much wider mechanical bandwidth than a rigid rotor, which resulting in a much larger response to high frequency forces. Thus for flexible rotors, the controller design at high frequencies is much more important than for rigid rotors. Besides, when there are non-collocated sensors and actuators, there will be flexible modes with a node between a sensor-actuator pair. If these modes have frequencies within the bandwidth of the controller, then the stability of the system might be altered by additional zeros induced by the non-collocation, thus the control of flexible rotor systems generally requires a more elaborate control design approach.

Finite element method (FEM) is used to model the flexible shaft, with the 6 degrees of freedom (DOFs) Timoshenko beam element.

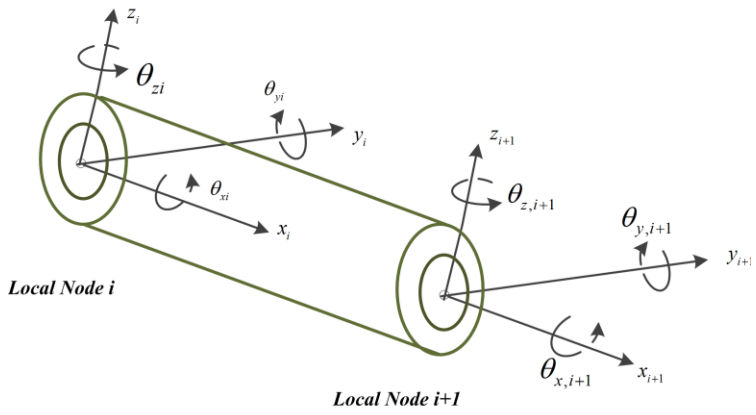

Figure 8 Timoshenko beam element with 6 degrees of freedom

Figure 8 shows a Timoshenko beam element with two local nodes and 6 DOFs at each node. The degree of freedom vector for the i^{th} element is

$$U_e = [x_i y_i z_i \theta_{x,i} \theta_{y,i} \theta_{z,i} x_{i+1} y_{i+1} z_{i+1} \theta_{x,i+1} \theta_{y,i+1} \theta_{z_{,i+1}}]^T \tag{30}$$

2.2.1 Finite element matrices of the element

For a symmetric cylindrical beam, the mass matrix of the element is built with the lumped mass method in the form of

$$M_e = \begin{bmatrix} m_i & & & & & & & & & & & \\ & m_i & & & & & & & & & & \\ & & m_i & & & & 0 & & & & & \\ & & & I_{pi} & & & & & & & & \\ & & & & I_{ti} & & & & & & & \\ & & & & & I_{ti} & & & & & & \\ & & & & & & m_{i+1} & & & & & \\ & & 0 & & & & & m_{i+1} & & & & \\ & & & & & & & & m_{i+1} & & & \\ & & & & & & & & & I_{p,i+1} & & \\ & & & & & & & & & & I_{t,i+1} & \\ & & & & & & & & & & & I_{t,i+1} \end{bmatrix} \tag{31}$$

where

$$\begin{aligned} m_i &= \frac{\pi}{4}(D_{O,i}^2 - D_{I,i}^2) L_i \rho \\ I_{pi} &= \frac{m_i}{8}(D_{O,i}^2 + D_{I,i}^2) \\ I_{ti} &= \frac{m_i}{48}(3D_{O,i}^2 + 3D_{I,i}^2 + 4{L_i}^2) \end{aligned} \tag{32}$$

I_p is the polar moment of inertia, I_t is the transverse moment of inertia, $D_{O,i}$ is the outside mass diameter of the element, $D_{I,i}$ is the inner diameter of the element, L_i is the length of the element, and ρ is the mass density of the rotor material.

The stiffness of the element is based on the linear elastic assumption and in the form of

$$K_e = \begin{bmatrix} a_1 & 0 & 0 & 0 & 0 & 0 & -a_1 & 0 & 0 & 0 & 0 & 0 \\ & a_2 & 0 & 0 & 0 & b_1 & 0 & -a_2 & 0 & 0 & 0 & b_1 \\ & & a_3 & 0 & b_2 & 0 & 0 & 0 & -a_3 & 0 & b_2 & 0 \\ & & & c_1 & 0 & 0 & 0 & 0 & 0 & -c_1 & 0 & 0 \\ & & & & c_2 & 0 & 0 & 0 & -b_2 & 0 & d_2 & 0 \\ & & & & & c_3 & 0 & -b_1 & 0 & 0 & 0 & d_3 \\ & & & & & & a_1 & 0 & 0 & 0 & 0 & 0 \\ & & & & & & & a_2 & 0 & 0 & 0 & -b_1 \\ & & & \textit{symmetric} & & & & & a_3 & 0 & -b_2 & 0 \\ & & & & & & & & & c_1 & 0 & 0 \\ & & & & & & & & & & c_2 & 0 \\ & & & & & & & & & & & c_3 \end{bmatrix} \quad (33)$$

where

$$a_1 = \frac{AE}{L},\ a_2 = \frac{12EI_{t\_a}}{L^2\beta_z},\ a_3 = \frac{12EI_{t\_a}}{L^2\beta_y}$$

$$b_1 = \frac{6EI_{t\_a}}{L\beta_z},\ b_2 = -\frac{6EI_{t\_a}}{L\beta_y}$$

$$c_1 = \frac{I_{p\_a}G}{L},\ c_2 = \frac{EI_{t\_a}(4+\Phi_y)}{\beta_y},\ c_3 = \frac{EI_{t\_a}(4+\Phi_z)}{\beta_z}$$

$$d_2 = \frac{EI_{t\_a}(2-\Phi_y)}{\beta_y},\ d_3 = \frac{EI_{t\_a}(2-\Phi_z)}{\beta_z}$$

$$\beta_y = L\left(1+\Phi_y\right),\ \beta_z = L\left(1+\Phi_z\right)$$

$$\Phi_y = \frac{12EI_{t\_a}\alpha_y}{GAL^2},\ \Phi_z = \frac{12EI_{t\_a}\alpha_z}{GAL^2}$$

α_y and α_z are the transverse shear form factors in the y- and z- directions, G is the elastic shear modulus of the rotor material, E is the Young's modulus of the rotor material, L is the length of the element, A is the cross sectional area of the element,

$I_{t\_a} = \frac{\pi}{64}(D_{O,i}^4 - D_{I,i}^4)$ is the transverse area moment of inertia, and

$I_{p\_a} = \frac{\pi}{32}(D_{O,i}^4 - D_{I,i}^4)$ is the polar area moment of inertia.

The disk gyroscopic effects are taken into consideration in this study. The gyroscopic matrix is in the form of

$$G_i = \begin{bmatrix} 0 & 0 & 0 & 0 & 0 & 0 \\ 0 & 0 & 0 & 0 & 0 & 0 \\ 0 & 0 & 0 & 0 & 0 & 0 \\ 0 & 0 & 0 & 0 & 0 & 0 \\ 0 & 0 & 0 & 0 & 0 & I_{pi}\omega \\ 0 & 0 & 0 & 0 & -I_{pi}\omega & 0 \end{bmatrix} \begin{matrix} \leftarrow x_i \\ \leftarrow y_i \\ \leftarrow z_i \\ \leftarrow \theta_{xi} \\ \leftarrow \theta_{yi} \\ \leftarrow \theta_{zi} \end{matrix} \quad (34)$$

$$\begin{matrix} \uparrow & \uparrow & \uparrow & \uparrow & \uparrow & \uparrow \\ x_i & y_i & z_i & \theta_{xi} & \theta_{yi} & \theta_{zi} \end{matrix}$$

The gyroscopic matrix represents the angular velocity dependent torques due to the simultaneous shaft spin and disc tilting motion. The gyroscopic moments couple the dynamics in the two radial directions of motion, thus a change in the vertical state of the rotor affects the horizontal dynamics, and vice versa. Due to these two cross coupled

term in the radial directions, gyroscopic moments cause the critical speeds of the system to drift from their original predictions at zero spin speed.

2.2.2 Assembly of the finite element matrices

Since the element mass matrices are diagonal, the assembled global mass matrix is also diagonal in the form of

$$M = diag([m_1 m_1 m_1 I_{p1} I_{t1} I_{t1} ... m_i m_i m_i I_{pi} I_{ti} I_{ti} ... m_N m_N m_N I_{pN} I_{tN} I_{tN}]) \qquad (35)$$

where i indicates the number of the node. For a rotor with N nodes, the dimension of the mass matrix is 6NX6N.

For the 1^{st} node and the N^{th} node,

$$m_1 = \frac{1}{2} m_1^e,\ I_{p1} = \frac{1}{2} I_{p1}^e,\ I_{t1} = \frac{1}{2} I_{t1}^e$$

$$m_N = \frac{1}{2} m_N^e,\ I_{pN} = \frac{1}{2} I_{pN}^e,\ I_{tN} = \frac{1}{2} I_{tN}^e$$

where m_1^e and m_N^e are the mass of the 1^{st} node and the N^{th} node, I_{p1}^e and I_{pN}^e are the polar moment of inertia of the 1^{st} and the N^{th} node, and I_{t1}^e and I_{tN}^e are the transverse moment of inertia of the 1^{st} and the N^{th} node.

For node number $i = 2, 3, ..., N-1$

$$m_i = \frac{1}{2}(m_i^e + m_{i-1}^e),\ I_{ti} = \frac{1}{2}(I_{ti}^e + I_{t,i-1}^e),\ I_{pi} = \frac{1}{2}(I_{pi}^e + I_{p,i-1}^e)$$

where m_i^e and m_{i-1}^e are the mass of the i^{th} node and the $(i-1)^{th}$ node, I_{pi}^e and $I_{p,i-1}^e$ are the polar moment of inertia of the i^{th} node and the $(i-1)^{th}$ node, and I_{ti}^e and $I_{t,i-1}^e$ are the transverse moment of inertia of the i^{th} node and the $(i-1)^{th}$ node.

The global stiffness matrix of the rotor is assembled from the 12X12 element stiffness matrices $K^1, K^2, K^3, \ldots, K^{E-1}, K^E$ in the form shown in Figure 9. E is the total number of elements of the shaft.

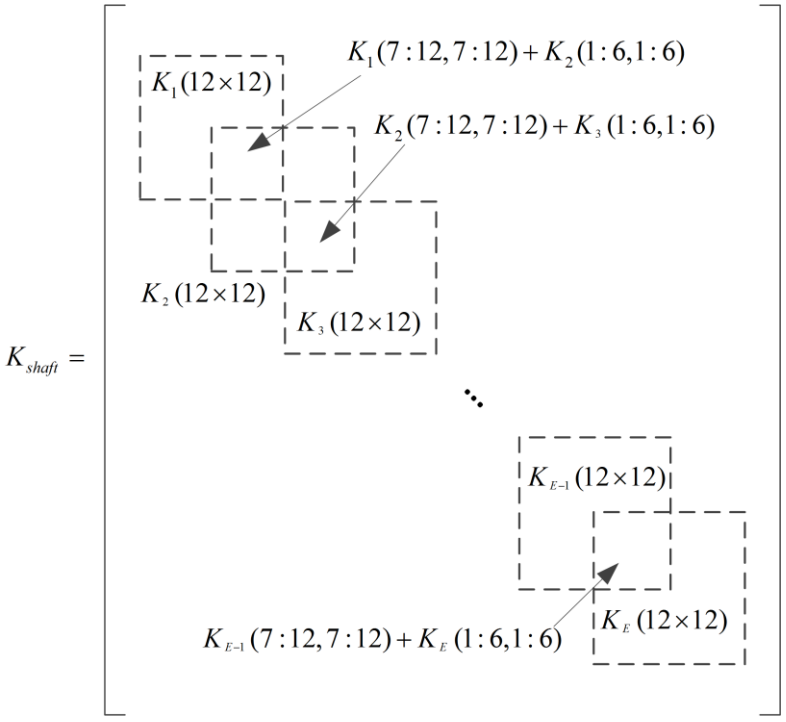

Figure 9 Assembly of the shaft stiffness matrix

For the first 6X6 components in the global stiffness matrix corresponding to the 1^{st} element, and the last 6X6 components in the global stiffness matrix corresponding to the E^{th} (last) element, the values remain same with the element matrices, i.e.

$$K_{shaft}(1:6,1:6) = K_1(1:6,1:6)$$

$$K_{shaft}(6E+1:6E+6,6E+1:6E+6) = K_E(7:12,7:12)$$

For elements $i = 2,3,...,(E-1)$, the global shaft stiffness matrix is assembled by

$$\begin{aligned} &K_{shaft}(6(i-1)+1:6(i-1)+12,6(i-1)+1:6(i-1)+12) \\ &= K_i(1:12,1:12)+\begin{bmatrix} K_{i-1}(7:12,7:12) & 0_{6\times6} \\ 0_{6\times6} & 0_{6\times6} \end{bmatrix}+\begin{bmatrix} 0_{6\times6} & 0_{6\times6} \\ 0_{6\times6} & K_{i-1}(1:6,1:6) \end{bmatrix} \end{aligned} \quad (36)$$

2.3 Sensors, Controllers, Power Amplifiers and Filters

In this study, the system components with finite bandwidth are described by transfer functions. In the field of control systems, the dynamics of the system can be written in terms of a transfer function, which is a mathematical representation for fit or to describe inputs and outputs of black box models. Figure 10 shows a simple block diagram of a transfer function, in which Y(s) is the input and X (s) is the output.

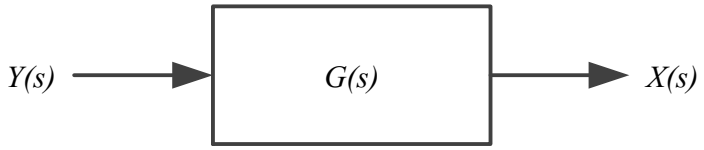

Figure 10 Block diagram of a transfer function

The transfer function is G(s), which is the ratio of the output of the system over the input of the system in the form of

$$G(s) = \frac{X(s)}{Y(s)} \tag{37}$$

The input, output, and transfer function are complex quantities since they contain both amplitude and phase information. Bode plots, which describes the amplitude and the phase with respect to the frequency, are used to describe the transfer functions.

2.3.1 Sensors

Displacement sensors are used in the closed loop to measure the position of the rotating rotor and convert the physical displacement into voltage signal. The sensitivity of a sensor is the ratio of the output signal over the input. For a displacement sensor, the sensitivity is the output voltage over input displacement in $mV/\mu m$. Sensor runouts are noise disturbances caused by the uneven rotating surfaces, geometry errors, and electrical or optical inhomogeneity at the sensor locations. A larger sensitivity by using electronic amplification can be obtained for a larger output. However, this amplification also amplifies the sensor runouts induced noise. Generally, the sensitivity is bounded by the signal-to-noise (SNR) ratio.

The sensor used in the system is a typical displacement model, which has a sensitivity (DC gain) and a 1st order filter of high bandwidth. The high bandwidth is set to avoid large sensor effects on system stability and performance. The transfer function of the sensor is

$$TF_{sen}(s) = \frac{G_{sen}}{\tau_{sen} s + 1} \tag{38}$$

where G_{sen} is the sensitivity or gain of the sensor, and τ_{sen} is the time constant of the 1st order filter in the sensor.

2.3.2 Power amplifiers

In a lot of the linear simulations for AMB systems, power amplifiers are simply described as DC gains with low pass filters. However, real amplifiers are limited by power supply voltage and maximum coil current. To include these power amplifier saturation effects, a nonlinear power amplifier model with a current and voltage limit are used in this study. Figure 11 is the block diagram of a typical power amplifier with voltage and current limits. It shows the current feedback control loop from the input voltage to the output current in the power amplifier. In the feedback loop, the instantaneous commanded current is compared with the measured current in the magnetic bearing coils. Typical efficiencies of this power amplifier are generally greater than 90%, thus the power amplifier loss is ignored.

In the linear stage, the power amplifier transfer function from the input voltage to the output current is

$$\frac{I_{out\_i}}{V_{in\_i}} = \frac{K_{amp}}{L_{amp} s + R_{amp} + K_{amp} \gamma} \tag{39}$$

where the resistance $R_{amp} = R_{coil}$, and the reluctance L_{amp} is approximated by the coil parameters in the form of

$$L_{amp} = \frac{\mu N^2 A_g}{l_c} \tag{40}$$

where μ is the free space permeability, N is the number of coil turns, A_g is the air gap area, and l_c is the coil length in Figure 7. The resistance and the reluctance of the coil change with design variables since the coil geometry varies with different designs in the optimization. K_{amp} and γ_{amp} are the gains in the forward loop and the feedback loop respectively.

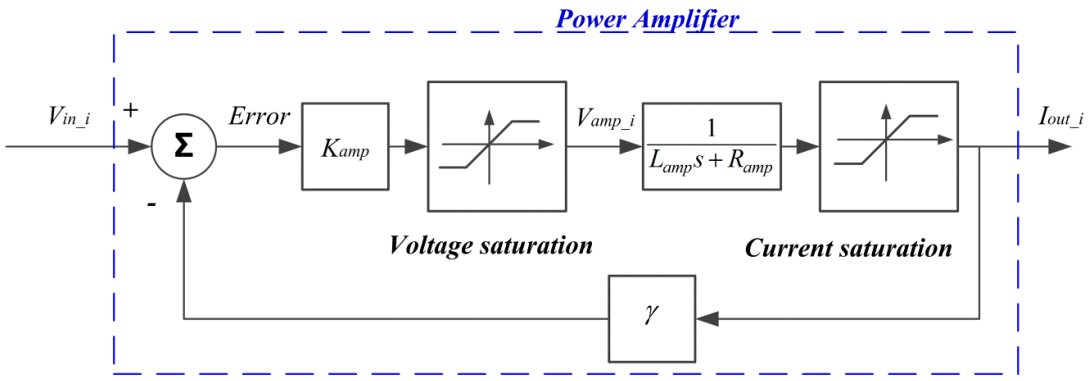

Figure 11 Nonlinear power amplifier model with voltage and current saturation

From Figure 11,

$$V_{amp\_i} = (L_{amp}s + R_{amp})I_{out\_i} \tag{41}$$

$$V_{amp\_i} = (V_{in\_i} - I_{out\_i}\gamma)K_{amp} \tag{42}$$

Given the DC gain G_{dc} and bandwidth of the power amplifier w_{bd}, the transfer function from the input voltage to the output current is

$$\frac{I_{out\_i}}{V_{in\_i}} = \frac{G_{dc}}{\frac{s}{w_{bd}} + 1} \tag{43}$$

Solving (41), (42) and (43) gives

$$K_{amp} = L_{amp} w_{bd} G_{dc} \tag{44}$$

$$\gamma = \frac{L_{amp} w_{bd} - R_{amp}}{L_{amp} w_{bd} G_{dc}} \tag{45}$$

When there is voltage saturation, the output current is $I_{out\_i} = \frac{V_{sat}}{L_{amp} s + R_{amp}}$;

when there is current saturation, the output current is $I_{out\_i} = i_{sat}$, where V_{sat} and i_{sat} are the saturation voltage and saturation current of the power amplifier.

2.3.3 Controllers and compensators

PD controllers are used in this study to control the closed loop system. The transfer function of the PD controller is written as

$$TF_{con}(s) = \frac{G_p + G_d s}{(\tau_p s + 1)(\tau_d s + 1)^2} \tag{46}$$

where G_p is the proportional gain of the PD controller, G_d is the derivative gain of the controller, τ_p and τ_d are the time constants of the proportional gain and derivative gain respectively.

Figure 12 shows the closed-loop step response of a 2nd order system controlled by PD controllers with different controller gains. The transfer function of the 2nd order system is in the form of

$$TF_{plant}(s) = \frac{1}{s^2 + 5s + 6} \tag{47}$$

Increasing the proportional gain can decrease the rise time to the target, and decrease the steady state error. However, large proportional gains increases the overshoot and degrade the system stability. Derivative gain does not have too much impact on the rise time or the steady state error. However, an increase in derivative gain can decrease the overshoot, and improve the stability when the derivative gain is small.

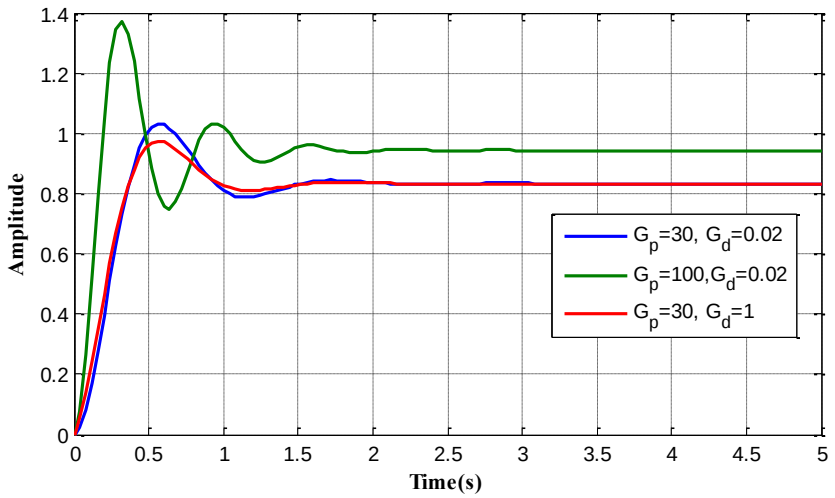

Figure 12 Response of the PD controller to step reference input with different controller gains

The system dynamics could be of a nature that a satisfactory stable design cannot be obtained through adjustment of proportional gain alone. In such cases, compensation of the dynamics is indicated. Three simple and effective compensation methods, lead, lag, and notch compensations are used in this study.

A phase lead compensation stage may be utilized for improving phase stability-margin. A form of the transfer function for a phase lead stage is

$$TF_{lead}(s) = K_{lead}\frac{s+z}{s+p},\ z < p \tag{48}$$

Figure 13 shows a bode plot of a lag compensator with a transfer function in the form of

$$TF_{lead}(s) = \frac{s+1}{s+1.2} \tag{49}$$

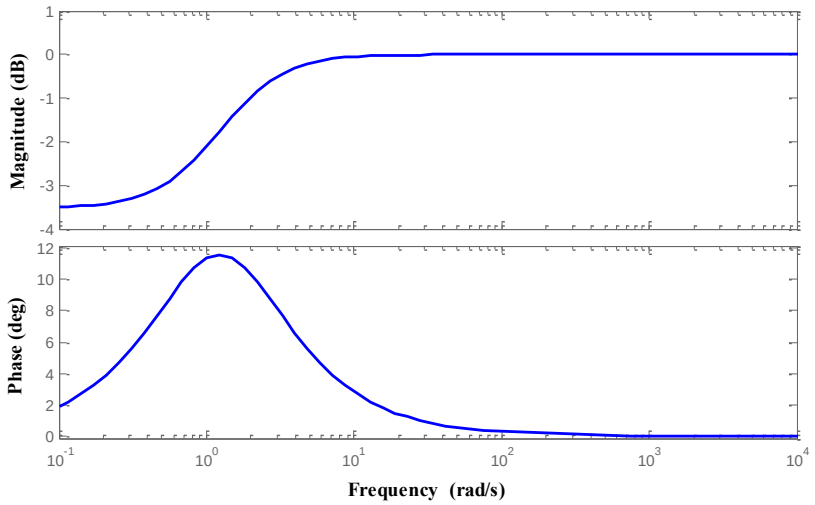

Figure 13 Bode plot of a lead compensator

A phase lag stage is very useful for providing low frequency (DC) gain to reject errors due to static, typically weight, loading acting on the magnetic bearing. A form of the phase lag stage is

$$TF_{lag}(s) = K_{lag}\frac{s+z}{s+p},\ z > p \tag{50}$$

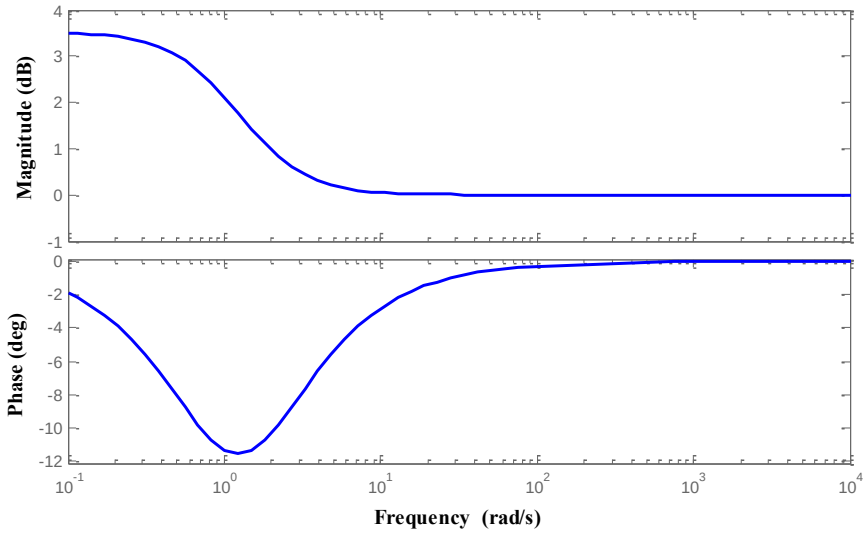

Figure 14 Bode plot of a lag compensator

Figure 14 shows a bode plot of a lag compensator with a transfer function in the form of

$$TF_{lead}(s) = \frac{s+1.2}{s+1} \tag{51}$$

A notch filter is utilized to reduce the gain at the high frequency, which is called gain stabilization. A typical transfer function of a notch filter is in the form of

$$TF_{notch}(s) = \frac{s^2 + 2\zeta\omega_0 s + \omega_0{}^2}{(s+\omega_0)^2} \tag{52}$$

Figure 15 is the bode plot of a notch filter with the transfer function in the form of

$$TF_{notch}(s) = \frac{s^2 + 0.8s + 3600}{(s+60)^2} \tag{53}$$

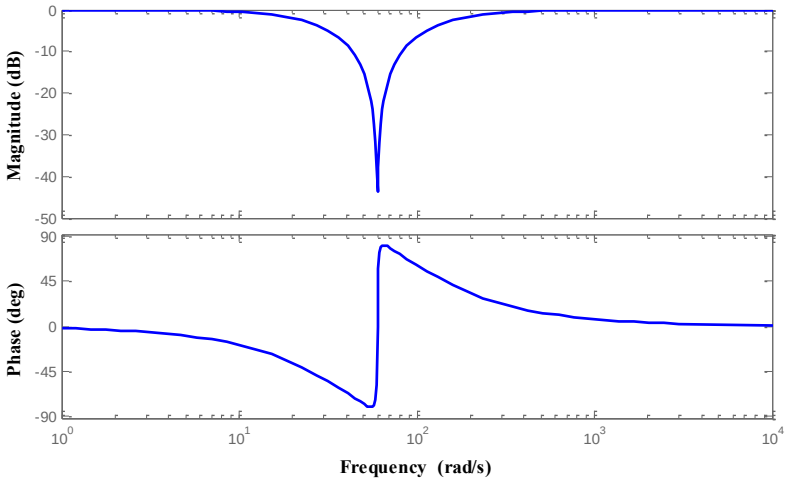

Figure 15 Bode plot of a notch filter

The choice of the notch center frequencies is targeted to remove the respective harmonic disturbance from the imbalance and the sensor runouts, thus alleviating the control efforts.

3. MULTIPLE-OBJECTIVE OPTIMIZATION AND GENETIC ALGORITHMS

Multiple-objective optimization, in which multiple objective functions need to be optimized simultaneously, has received a lot of interest from researchers with different backgrounds. Multiple-objective optimization arises because in the real design problems, determining which solutions are best in a multidimensional solution space can be difficult, especially when one does not understand the tradeoffs among the solutions. A mathematical definition of multiple objective optimization problem can be addressed as:

Minimize (or maximize)

$f_i(x_1,x_2, \ldots,x_n), i=1,2 \ldots p$

such that

$h_j(x_1,x_2, \ldots,x_n) < 0, j=1,2, \ldots q$

where $(x_1,x_2, \ldots,x_n)$ are the n design variables, $f_i(x_1,x_2, \ldots,x_n)$ are the p objective functions, $h_j(x_1,x_2, \ldots,x_n)$ are the q inequality constraints.

3.1 Pareto Solutions of Multiple Objective Optimization

In multi-objective optimization problems, because of the incommensurability and confliction among multiple objectives, there does not necessarily exist a solution that is best for all objectives. A solution might be the best in one of the objectives but the worst in the other objectives. Therefore for the multi-objective optimization cases, there usually exists a set of solutions that none of the objective functions can be improved in value without impairment in some of the other objective values. Such solutions are

called Pareto solutions or non-dominated solutions, which are usually displayed in the form of Pareto's frontier. [22] Figure 16 shows an example of the Pareto optimal points in an optimization with two minimization type objectives. These points form a Pareto frontier, on which objective 1 can only be minimized with the sacrifice of a larger objective 2 value and vice versa.

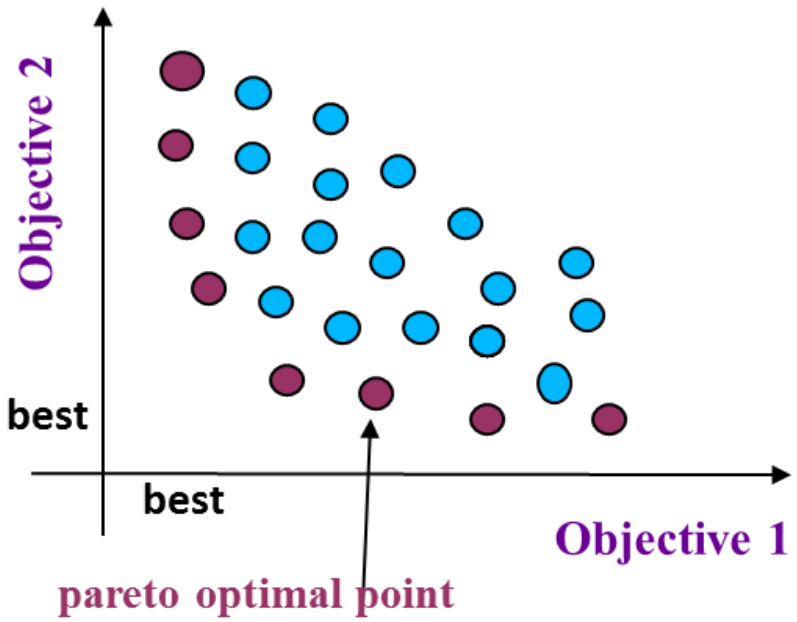

Figure 16 Pareto's frontier and Pareto solutions in optimization with two objectives

The x_A solution is said to dominate another solution x_B , and write as $x_A \circ x_B$, if both the following two conditions are met:

1) x_A is no worse than x_B in all objectives;

2) x_A is strictly better than x_B in at least one of the objectives.

In the minimization type optimization problem, the mathematical expression is

$$x_A \circ x_B \text{ iff } \begin{cases} f_i(x_A) \le f_i(x_B) & \forall i \in 1,2,...,N_{obj} \\ \exists j \in 1,2,...,N_{obj} \ \ s.t. \ \ f_i(x_A) < f_i(x_B) \end{cases} \tag{54}$$

where N_{obj} is the number of optimization objectives. If any of the above two conditions is violated, then the solution x_A does not dominate the solution x_B. All the Pareto solutions are non-dominated solutions.

3.2 Genetic Algorithms and Multiple Objective Genetic Algorithms

Genetic Algorithms (GAs) are adaptive heuristic search algorithms based on the evolutionary ideas of natural selection and genetics. [23] During the past decades, GA has been applied on diversity areas ranging from biology to engineering optimizations. GA has a lot of advantages over other optimization techniques, and the main advantages that we are choosing them for this study include that it [24]

1) Works with a large number of variables that many parameters can be optimized inside the magnetic bearing system.
2) Simultaneously searches from a wide sampling of the cost surface.
3) Provides a list of optimum parameters, not just a single solution.
4) Is welled suited for parallel computer.

Figure 17 shows the flow chart of the genetic algorithms. In GAs, the evolution starts from a population of randomly generated individuals which is called initial generation. The fitness of every individual in the population, which is usually the objective function value, is evaluated in each generation. The more fit individuals are

stochastically selected from the current population as parents to crossover and mutate to reproduce offspring as a new generation. In the crossover, new child populations are generated by combining the parts from the parent populations. In the mutation, the new child populations are generated by changing parts in the parent populations. The new generation is then used in the next algorithm iteration. The iteration terminates when either a maximum number of generations has been produced of a satisfactory level of fitness is reached for the population.

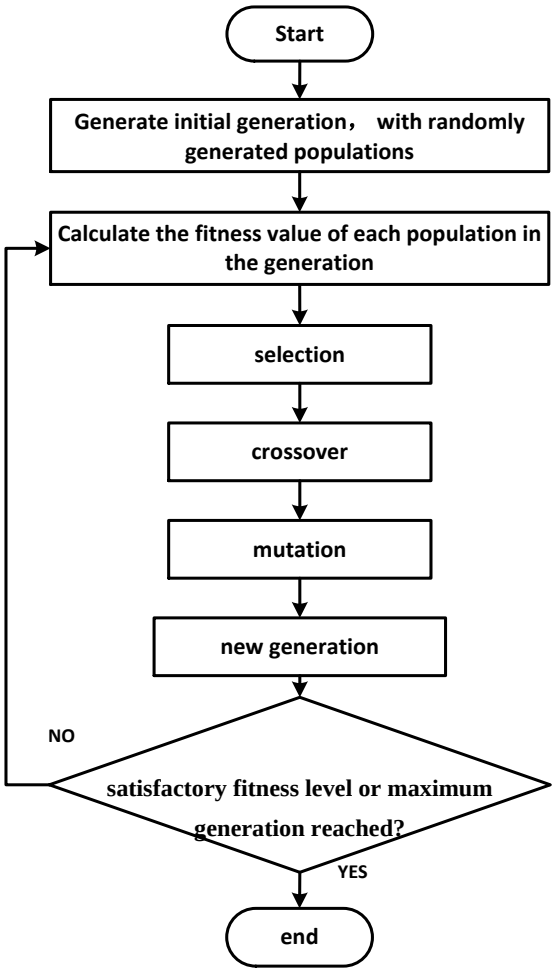

Figure 17 Flow chart of genetic algorithms

Following is a few simple examples of the encoding, selection, crossover and mutation in the case of binary string.

1) Encoding and creating an initial population

Binary encoding is the most common, mainly because first works about GA used this type of encoding. In binary encoding every population is a string of bits, 0 or 1. A typical 8 bit binary encoded population is in the form of

(1 1 1 0 1 0 1 0)

2) Evaluating fitness and selection

The populations are passed to the cost function for evaluation. The cost function is based on the objective function values.

In selection, the most fitted parents are assigned the highest probability of being selected to generation off springs. The two most common ways of selection are roulette wheel and tournament selection.

In roulette wheel selection, the populations are firstly sorted for the selection. Each population is assigned a probability of being selected based on either its rank in the sorted population of its cost.

Figure 18 is the roulette wheel probabilities that the parents are selected for the cases with four parents and eight parents. The populations with the low costs have a higher probability of being selected. The roulette wheel shows that with four parents, the first and the best parent population has a 40% chance of being selected. As the population number grows, the percent chance changes. In the case with eight parents, the best parent has a 22% chance of being selected.

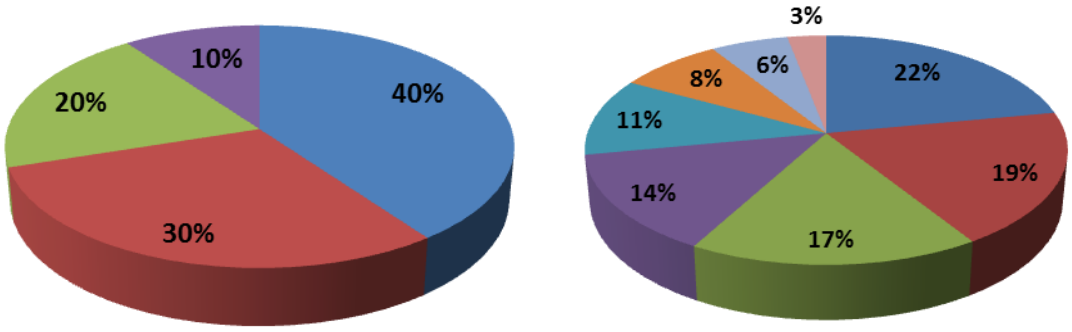

(a) *(b)*

Figure 18 Roulette wheel probabilities for (a) four parents (b) eight parents

In this study, the NSGA-II and NCGA algorithms are finally selected as the optimization techniques. These two algorithms use the tournament method for selection. The block diagram in Figure 19 shows the tournament selection process of the i^{th} tournament. In tournament selection, the populations are divided into different groups (usually two or three groups), and each group is called a tournament. The cost or fitness of each population is evaluated. A probability of being selected as a parent for crossover is assigned to the population according to the evaluation. The populations with lower cost or higher fitness are more likely to be selected for crossover.

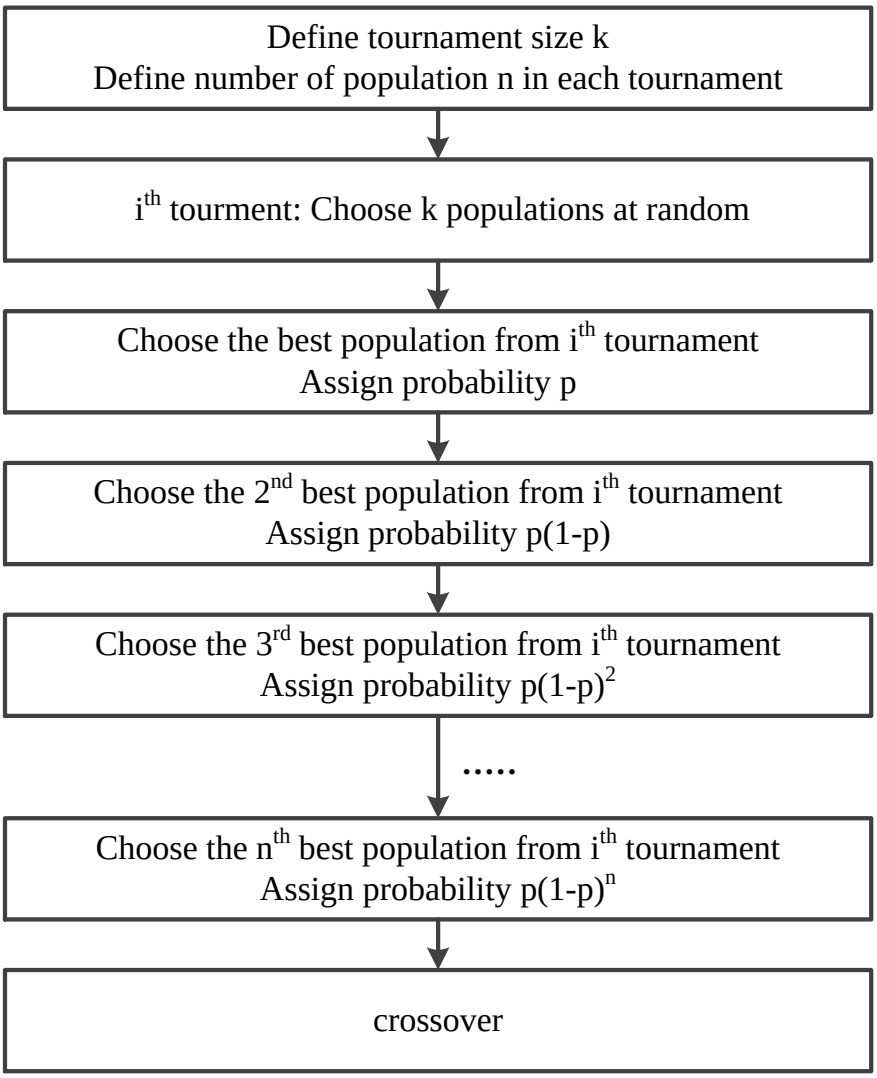

Figure 19 Block diagram of the tournament selection process

In deterministic tournament selection, only the population with the lowest cost in each group is selected as a parent ($p = 1$). Figure 20 shows a simplified example of the deterministic tournament selection: the unsorted populations are divided into different tournaments, then the fitness of each population is calculated, and only the best fitted population in each tournament is selected as parent to create more generations.

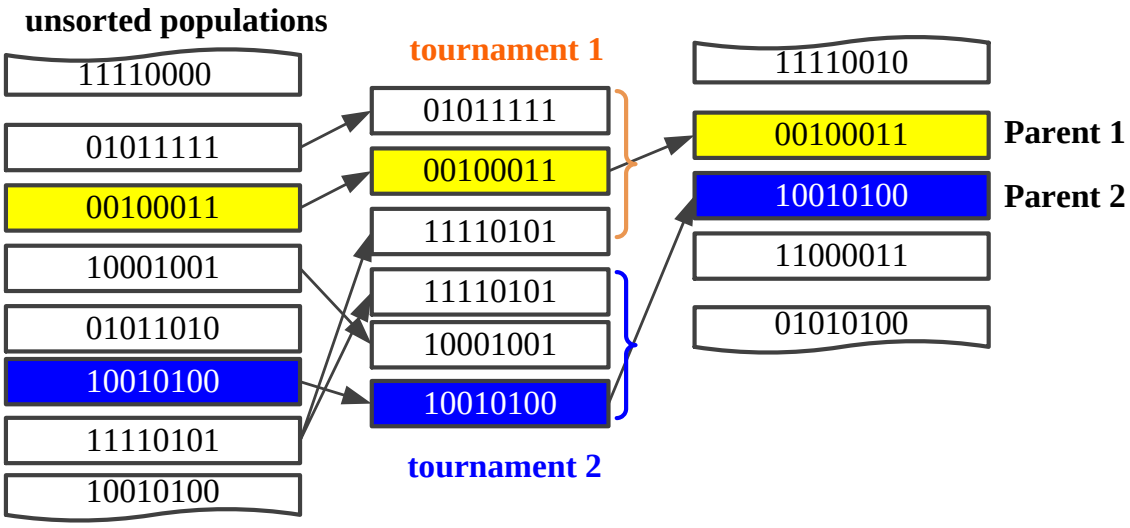

Figure 20 Deterministic tournament selection

3) Crossover

In crossover, the selected parents are recombined. Crossover replaces the genes of one parent by the genes of the other. Figure 21 shows an example of crossover of the two parents represented by binary strings at crossover point of 3.

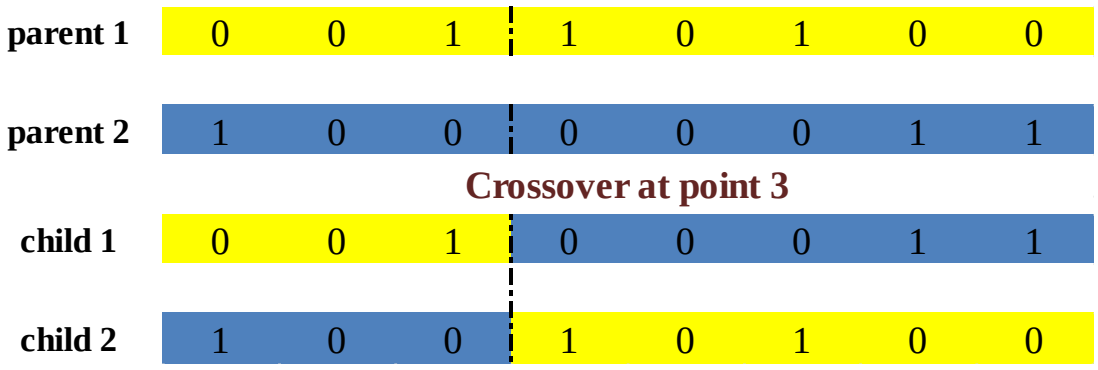

Figure 21 Binary strings crossover example

4) Mutation

In mutation, a gene or a subset of genes is chosen randomly and the value of the chose gene is changed. In the case of binary string, mutation is simply achieved by alternation of the selected bit or bits. For example, the string

(1 1 1 0 1 0 1 0)

with mutation at genes 2 and 4, becomes

(1 0 1 0 0 0 1 0)

In this optimization, NSGA-II and NCGA are the two selected multiple-objective optimization algorithms to optimize the design of the magnetic bearing supported rotordynamic system.

3.2.1 Non-dominated Sorting Genetic Algorithm II (NSGA-II)

NSGA-II is widely used and has become a de facto standard that other algorithms are compared with. The NSGA-II algorithm uses the simulated binary crossover (SBX) and the polynomial mutation for real coded variables. The selection, crossover, and mutation are same with the standard genetic algorithms. The difference is that it sorts the populations by "nondominated sorting" and "crowding distance sorting" before the selection.

Simulated Binary Crossover simulates the binary crossover observed in nature, and is described as

$$\begin{aligned} c_{1,k} &= \frac{1}{2}[(1-\beta_k)p_{1,k} + (1+\beta_k)p_{2,k}] \\ c_{2,k} &= \frac{1}{2}[(1+\beta_k)p_{1,k} + (1-\beta_k)p_{2,k}] \end{aligned} \tag{55}$$

where $c_{i,k}$ is the i^{th} child of the k^{th} component, $p_{i,k}$ is the selected parent, and β_k is a sample from a randomly generated number. The density of β_k is

$$p(\beta) = \begin{cases} \frac{1}{2}(n+1)\beta^n, if\ 0 \le \beta \le 1 \\ \frac{1}{2}(n+1)\frac{1}{\beta^{n+2}}, if\ \beta > 1 \end{cases} \tag{56}$$

where n is crossover distribution index. The probability distributions are plotted in Figure 22, which shows that a large index value gives a higher probability for creating solutions near the parents.

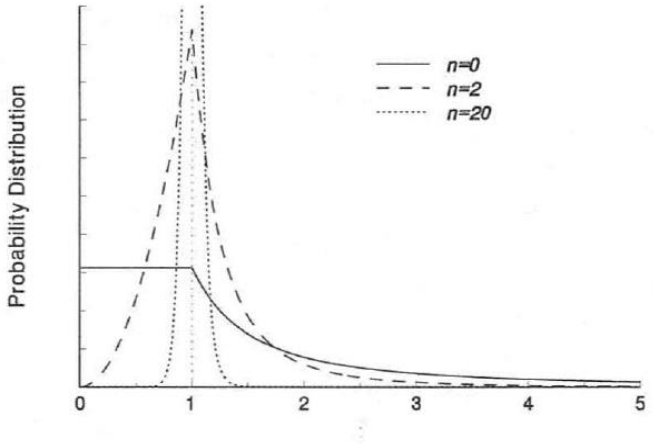

Figure 22 Probability distributions used in the SBX crossover operators with different crossover index n

Polynomial mutation used in NSGA-II can be expressed in the form of

$$c_k = p_k + (p_k^u - p_k^l)\delta_k \tag{57}$$

where c_k is the child mutated from the parent p_k, p_k^u and p_k^l are the upper and lower bounds of the parent, and δ_k is a small variation calculated from a polynomial distribution in the form of

$$\delta_k = \begin{cases} (2r_k)^{\frac{1}{m+1}} - 1, if\ r_k < 0.5 \\ 1 - \{2(1-r_k)\}^{\frac{1}{m+1}}, if\ r_k \geq 0.5 \end{cases} \quad (58)$$

where r_k is an uniformly sampled random number between (0,1) and m is mutation distribution index.

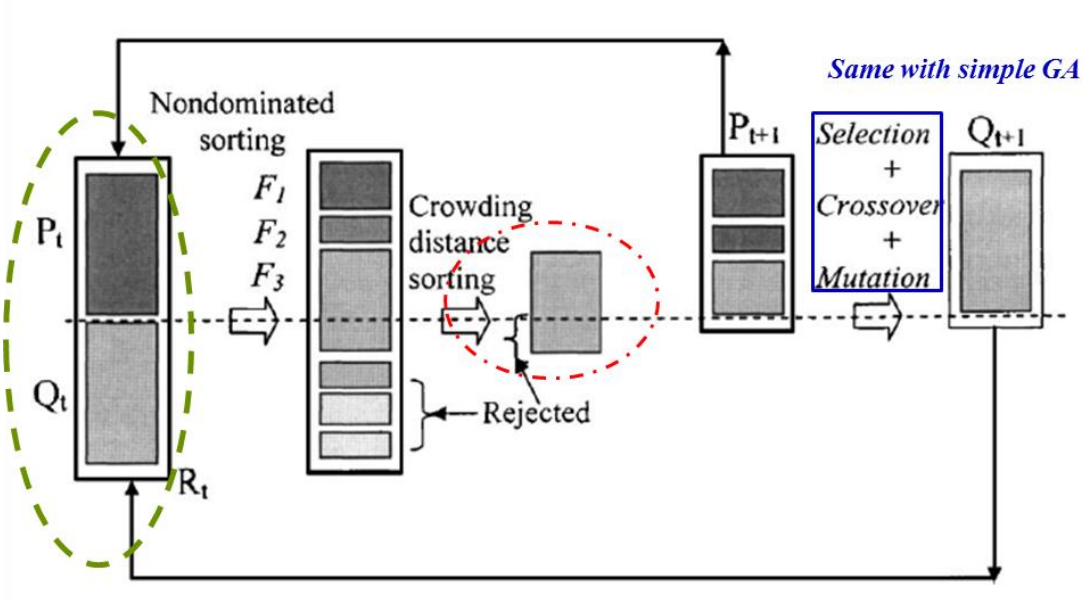

Figure 23 Schematic of NSGA-II algorithms

The algorithms of the NSGA-II are shown in Figure 23. F_1, F_2, F_3 in the figure indicate the different fitness levels by non-dominated sorting, t represents current generation, *t+1*represent next generation, P_t represents current parent populations, Q_t

represents current child populations, P_{t+1} represents new parent populations after sorting, Q_{t+1} represents new child populations, R_t represents mating pool combining the parent population P_t and the child population Q_t.

The non-dominated sorting ranks parent populations into different fitness levels $F_1, F_2, F_3 \ldots$ to ensure a higher probability for "good" parent populations to create more child populations.

Crowding distance sorting is introduced in NSGA-II. For two solutions with different non-domination ranks, the solution with the lower (better) rank is preferred. Otherwise, if the two solutions belong to the same non-domination rank, then the solution located in a less crowded region is a preferred solution. This crowding distance sorting ensures the diversity preservation. Circled with red dashed line is an example of crowding distance sorting, in which solutions in both the lower part and the upper part are of the 3rd fitness level, but the solutions in the upper part are selected because they are from the less crowded region.

In NSGA-II, an elitism operator is also introduced to speed up the performance of the GA and to prevent the loss of good solutions once they are found. An example of elitism is given as circled in green dashed line. The elitism strategy allows the excellent parent populations P_t join and compete with their child populations Q_t to form a now pool R_t to create new generations. The result demonstrated that elitism helps in speeding up the performance of the GA significantly and in preserving good solutions from the parent populations.

Constraint Handling: The binary tournament selection is used for constraint-handling in the NSGA-II algorithms, in which two solutions are picked from the population and the better one selected. There are three possible situations depending on whether or solution is feasible or infeasible:

1) Both solutions are feasible;
2) One is feasible and the other is infeasible;
3) Both are infeasible.

For single objective optimization, the rule to select a better solution is easy for each of these cases: For case 1), where both solutions are feasible, select the solution with better objective function value; For case 2), where only one solution is feasible, select the feasible solution; For case 3), where both are infeasible, select the solution with smaller constraint violation.

For multiple objective optimization, according to Deb etc, a solution i is said to constrained-dominate a solution, if any of the following conditions is true:

1) Solution i and solution j both feasible and solution i dominates solution.
2) Solution i is feasible and solution j is not;
3) Solution i and solution j are both infeasible, but solution i has a smaller overall constraint violation.

Under this definition, all the feasible solutions have a better nondomination rank than the infeasible solutions. All the feasible solutions are ranked based on the objective function values. All the infeasible solutions are ranked in the way that a solution with a smaller constraint violation has a better nondomination rank.

The NSGA-II algorithms do not use any penalty function, so that either the value of the objective function or the measure of the constraint violation is sufficiently reduced in each iteration.

The iteration is terminated when the number of maximum generations is reached. The number of the maximum generation should be large enough to ensure the convergence of the solutions from the last generation.

3.2.2 Neighborhood Cultivation Genetic Algorithm (NCGA)

The NCGA algorithms include the mechanisms of NSGA-II with standard genetic operation of mutation and crossover included. What makes the NCGA unique is the mechanism of neighborhood crossover, in which the parents are selected from populations with values close to one of the objectives while in normal crossover the parents are chosen randomly from the populations. The exploration and exploitation concepts are used to explain the benefits of neighborhood crossover. By exploration, an optimum solution can be found around the elite solution. By exploitation, an optimum solution can be found in a global area. In neighborhood crossover, the child populations generated after the crossover may be close to the parent populations. The exploitation factor of the crossover is enforced through this. Therefore, the precise exploitation is expected. According to the example cases by Watanabe, the mechanism of neighborhood crossover helps both the exploration and exploitation. The example cases demonstrated the accuracy of the solutions of NCGA is improved compare with those of the NSGA-II with the neighborhood crossover.

4. LINEAR AND NONLINEAR ROTORDYNAMIC ANALYSIS

In this section, the synthesis of the system equations for linear analysis is talked. Rotordynamic analysis of the linear magnetic bearing system, including the stability analysis, levitation simulation, and unbalance transient analysis is presented with examples. Nonlinearities and nonlinearities induced rotordynamic performaces are introduced.

4.1 Synthesis of Linear Rotordynamic System

The mechanical system of a spinning shaft can be described by the equation [25]:

$$M\ddot{U} + (C + G)\dot{U} + KU = F_{ext} \tag{59}$$

where Timoshenko beam element is used and for each node there are 6 degree of freedom (dof). For each of the radial bearing, there are two displacement sensors, one for each of the y- and z- component. The nodal displacement vector U has the form:

$$U = [x_1 y_1 z_1 \theta_{x1} \theta_{y1} \theta_{z1} \ldots x_n y_n z_n \theta_{xn} \theta_{yn} \theta_{zn}]^T \tag{60}$$

where n is the number of nodes. The M, C, K, G are the mass, damping, stiffness, and gyroscopic matrices respectively of the rotor and bearing system. The assembly of the mass matrix, Gyrosopic matrix and stiffness matrix from the finite element has been introduced in section 2.2. F_{ext} is the external force exerted on the rotor, including gravity force, force from magnetic bearing, rotor unbalance force (in the unbalance analysis) and other possible forces induced by sensor runout etc.

In rotordynamic system, the equation (30) is generally written as first order ordinary differential equation (ODE) expressions as

$$\frac{d}{dt}\begin{bmatrix}\dot{U}\\ U\end{bmatrix}=\begin{bmatrix}-M^{-1}C & -M^{-1}K\\ I & 0\end{bmatrix}\begin{bmatrix}\dot{U}\\ U\end{bmatrix}+\begin{bmatrix}M^{-1}F_{ext}\\ 0\end{bmatrix} \tag{61}$$

For linear magnetic bearing analysis, the magnetic bearing force is linearized with respect to displacement and control current, and is represented by the bearing position stiffness and current stiffness, as has been talked in section 2.1. For example, the radial magnetic bearing force in y and z directions can be written as

$$\begin{aligned}F_{MBy} &= K_{py}y + K_{iy}i_{cy}\\ F_{MBz} &= K_{pz}z + K_{iz}i_{cz}\end{aligned} \tag{62}$$

The bearing position stiffness values K_{py} and K_{pz} are added into the entries in the shaft stiffness matrix K. Assume there is a radial magnetic bearing is located at node i, the global stiffness matrix K will be augmented as

$$\begin{aligned}K\left(6(i-1)+2,6(i-1)+2\right) &= K\left(6(i-1)+2,6(i-1)+2\right)+K_{py}\\ K\left(6(i-1)+3,6(i-1)+3\right) &= K\left(6(i-1)+3,6(i-1)+3\right)+K_{pz}\end{aligned} \tag{63}$$

The bearing current stiffness values are used as DC gains in the actuator model with 2nd order low pass filters, in the form of

$$TF_{actuator}(s)=\frac{K_i\omega_n^2}{s^2+2\zeta\omega_n s+\omega_n^2} \tag{64}$$

The actuator is then transformed into the state space form and assembled into the equation (48).

Assemble the state space forms of the sensors, controllers, power amplifiers and filters in the system, and write the equation in a more compact form,

$$\dot{W}_{sys} = A_{sys} W_{sys} + B_{sys} u_{sys} \tag{65}$$

where A_{sys} is the system matrix that includes the structural stiffness matrix, the mass matrix, the gyroscopic matrix, the damping matrix, and the controller dynamic parameters. B_{sys} is the input matrix. u_{sys} is the input of the system. W_{sys} is a system vector composed of structural variables and states of controllers, power amplifiers, sensors, filters and compensators in the form of

$$W_{sys} = [\dot{U}^T \; U^T W_{sen} W_{con} W_{pa} W_{act} W_{filter}]^T \tag{66}$$

where W_{sen} includes the state variables of the sensors, which are modeled as a DC gain with a first order filter. W_{con} includes the state variables of the PD controllers. W_{pa} includes the state variables of the power amplifiers modeled as a DC gain with a 1st order filter with an output current and voltage limit in the linear range. W_{act} includes the state variables of the actuator with 2nd order filters. W_{filter} includes the state variables of the additional low pass filters or any lead compensators and lag compensators.

4.2 Linear Rotordynamic Analysis with Example

In this example case, the rotor model used is given as in Figure 24. The rotor has 21 nodes, and with homopolar radial magnetic bearings placed at node 6 and node 16. At each of the magnetic bearing location, there are two sensors, in the horizontal direction

and vertical direction respectively. The total length of the rotor is 1m, and the total weight of the rotor is 61.1kg.

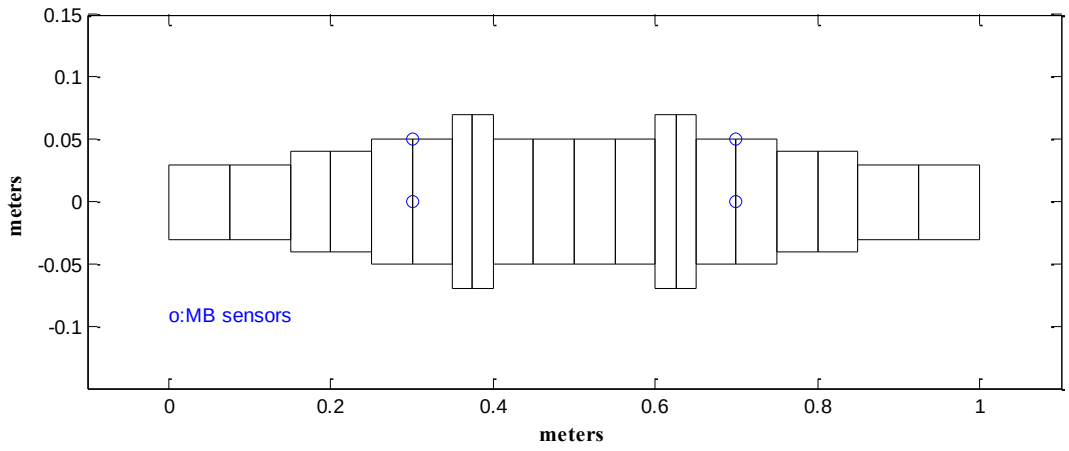

Figure 24 Plot of the finite element model of the rotor profile

The parameters of the homopolar magnetic bearing actuator are listed in Table 1. According to the equations in chapter 2, the resulting position stiffness in the y and z directions is -1.35e6 N/m, and the current stiffness in the y and z directions is 302.8 N/Amp.

The sensor used in the model has a DC gain of 1181V/m, and the time constant is 1e-5. Resulting transfer function of the sensor is

$$TF_{sen} = \frac{1181}{1E-5s+1} \tag{67}$$

The proportional gain of the PD controller is 20, and the derivative gain of the PD controller is 0.02, resulting transfer function of the PD controller is

$$TF_{con}(s) = \frac{20 + 0.02s}{(1E-5s+1)^3} \tag{68}$$

Table 1 Parameters of the homopolar magnetic bearing actuator

Parameter	Value
Coil turns, N	100
Air gap area, $A_g(m^2)$	0.01
Air gap length, $L_g(m)$	0.0005
Rotor material permeability, μ_r (H/m)	0.000628
Flux path length in rotor, L_r (m)	0.15
Flux area in rotor, $A_r(m^2)$	0.008
BI material permeabilty, $\mu_{bi}(H/m)$	0.000628
Flux path length in back iron, $L_{bi}(m)$	0.1
Flux area in back iron, $A_{bi}(m^2)$	0.008
Permanent magnet permeability, $\mu_{pm}(H/A)$	1.35E-06
Flux path length in Permanent magnet, $L_{pm}(m)$	0.05
Flux area in Permanent magnet, A_{pm} (m^2)	0.008
Coercive field intensity of magnet, H_c (A/m)	633000
Pole material permeabilty, μ_p (H/m)	0.000628
Length of pole, L_p (m)	0.05

4.2.1 Stability and modal analysis

The system stability is determined by the eigenvalue of the system matrix. The system is stable if all the eigenvalues has negative real parts. In this modal analysis, eigenvalues are filtered, only eigenvalues with positive imaginary part are counted.

As shown in Figure 25, that all the eigenvalues are on the left plane of the plot, which means that the system is stable. The rigid mode and the 1st and 2nd bending mode shapes are plotted in Figure 26~Figure 28.

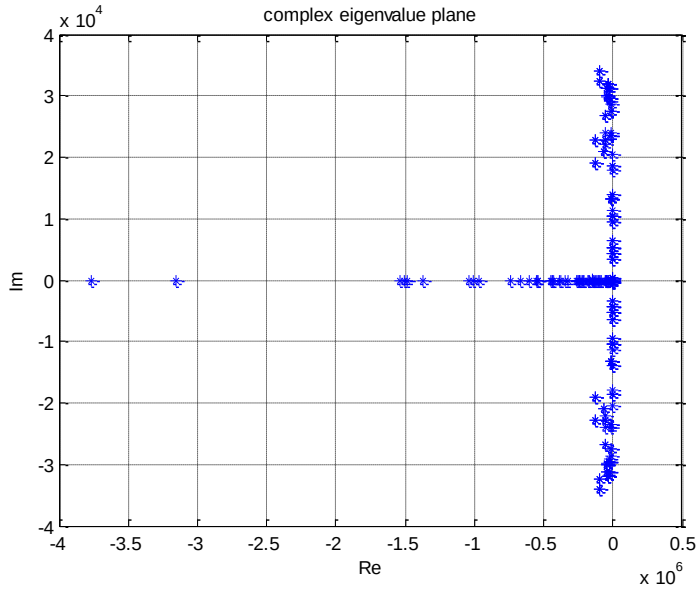

Figure 25 Eigenvalues of the system

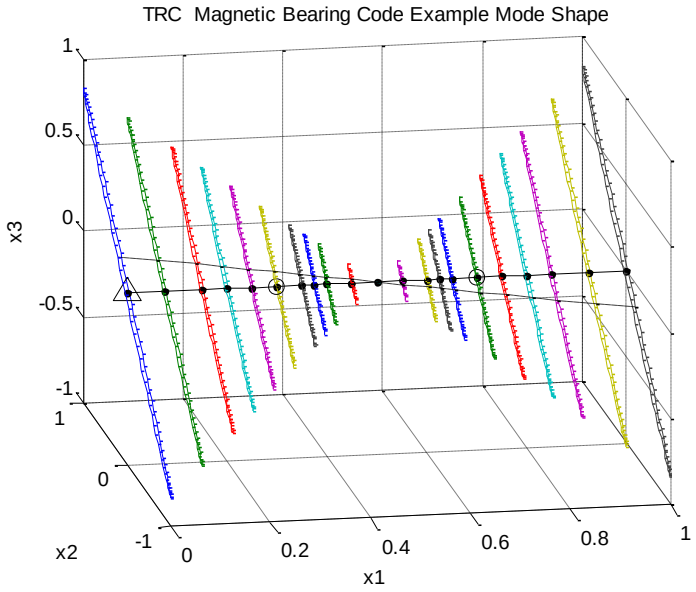

Figure 26 Mode shape of the rigid mode

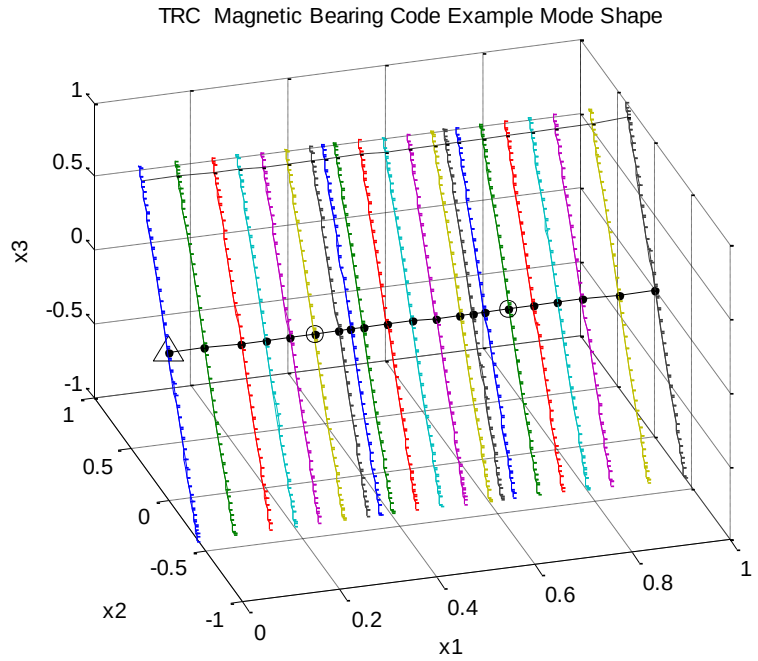

Figure 27 Mode shape of the bending mode

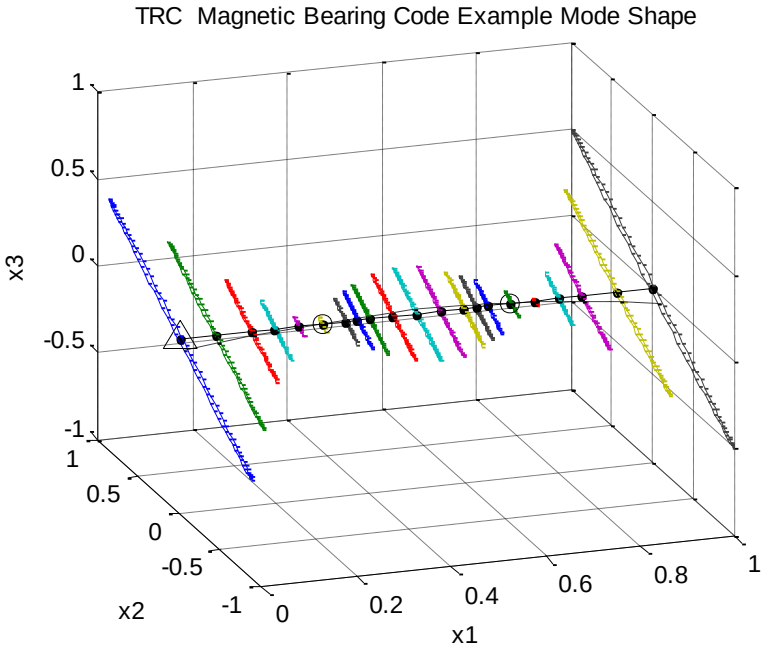

Figure 28 Mode shape of the bending mode_2

4.2.2 Unbalance response

The most important excitation in rotating machinery is due to unbalance forces. According to the API617, a separate damped unbalance rotor response analysis shall be conducted. The unbalance shall be placed at the locations that affect the particular mode most adversely. In this example case, the unbalance is located at the center of the symmetric bearing, and phased at 90° to excite most of the mode shape.

For a rotor with the equation of motion,

$$\frac{d}{dt}\begin{bmatrix}\dot{U}\\ U\end{bmatrix}=\begin{bmatrix}-M^{-1}C & -M^{-1}K\\ I & 0\end{bmatrix}\begin{bmatrix}\dot{U}\\ U\end{bmatrix}+\begin{bmatrix}M^{-1}F_{ext}\\ 0\end{bmatrix} \tag{69}$$

let $W_r=\begin{bmatrix}\dot{U}\\ U\end{bmatrix}$, $A_r=\begin{bmatrix}-M^{-1}C & -M^{-1}K\\ I & 0\end{bmatrix}$, $B_r=\begin{bmatrix}M^{-1}\\ 0\end{bmatrix}$, and $F_{ext}=F_{unbalance}$, then the equation of motion of the rotor can be described as

$$\dot{W}_r=A_rW_r+B_rF_{unbalance} \tag{70}$$

For unbalance analysis, substitute $F_{unbalance}=\tilde{F}_{unbalance}e^{i\omega t}$ and $W_{rotor}=\tilde{W}_{rotor}e^{i\omega t}$, $\tilde{W}_{rotor}$ can be solved as

$$\tilde{W}_r=(-i\omega\cdot I-A_r)^{-1}B_r\cdot\tilde{F}_{unbalance} \tag{71}$$

Finally, the displacement vector U under unbalance can be obtained.

In the example, the unbalance amount is 1.5kg·mm, which induces an unbalance force equivalent to 10% of the rotor weight at 3,600 rpm. The unbalance response plot is shown in Figure 29, which predicts a first critical speed of 4,640 rpm and a second critical speed of 35,210 rpm.

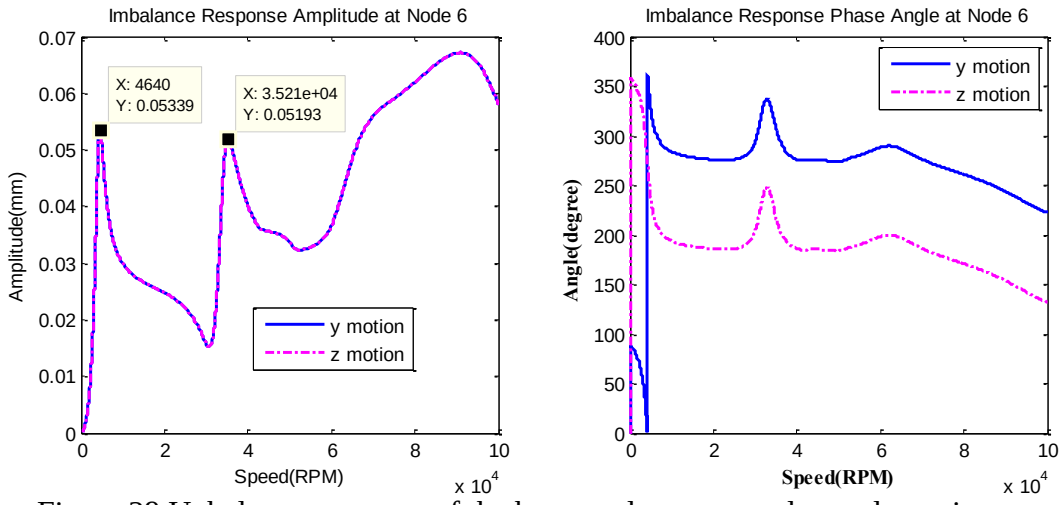

Figure 29 Unbalance response of the heteropolar supported rotordynamic system

4.2.3 Sensor runout analysis

Imperfections in the shaft surface, out-of roundness and non-uniform magnetic, optical and electrical properties produce a sensor output called "runout". Figure 35 shows highly magnified runout pattern, in which O_T is the target center of the rotor, O is the actual center of the rotor, and O_B is the center of the bearing.

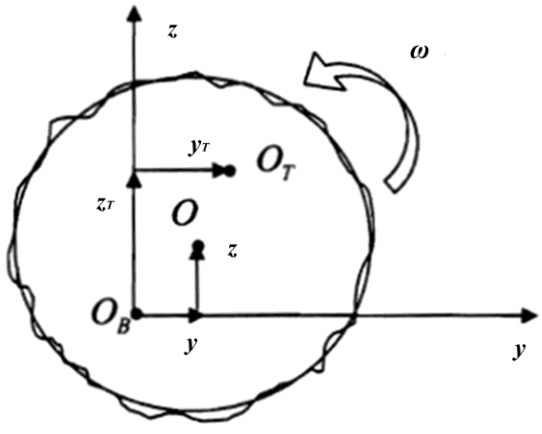

Figure 30 Highly magnified runout pattern

Runout is defined by the amplitude and phase angle of the "imperfections". In this example, the runout is defined as shown in Table 2. The y- direction sensors at both node 6 and noe7 have runouts of type 1, and the z- direction sensors at both nodes have runouts of type 2.

Table 2 Definition of the sensor runouts

		Runout Type 1	Runout Type 2
1X	1x Amp (mm)	0.17	0.17
	1x Phase (degree)	10	100
2X	2x Amp (mm)	0.0423	0.0423
	2x Phase (degree)	-50	110
3X	3x Amp (mm)	0.00847	0.00847
	3x Phase (degree)	90	180
4X	4x Amp (mm)	0.00508	0.00508
	4x Phase (degree)	-80	180
5X	5x Amp (mm)	0.00423	0.00423
	5x Phase (degree)	200	290

Besides the sensor runouts, there might be some random noise, which also needs to be defined by its maximum amplitude. In this example, the maximum amplitude of the random noise is defined as 0.001V, which corresponds to 0.00085mm in motion amplitude.

The magnetic bearing force response to the 5X runouts spectra is presented in Figure 31. Figure 32 shows the coil current response to the sensor runouts. Figure 33 shows the coil voltage response to the sensor runouts.

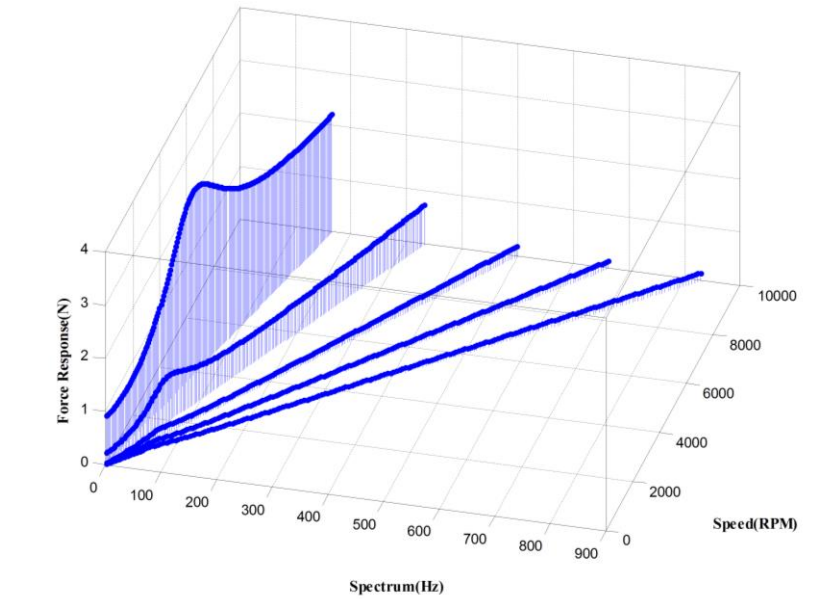

Figure 31 Force response to sensor runouts

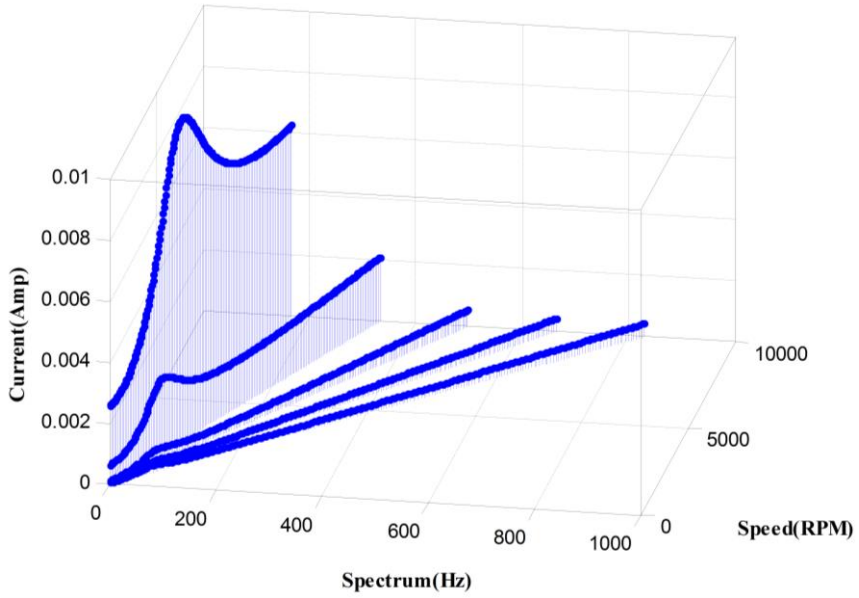

Figure 32 Current response to sensor runouts

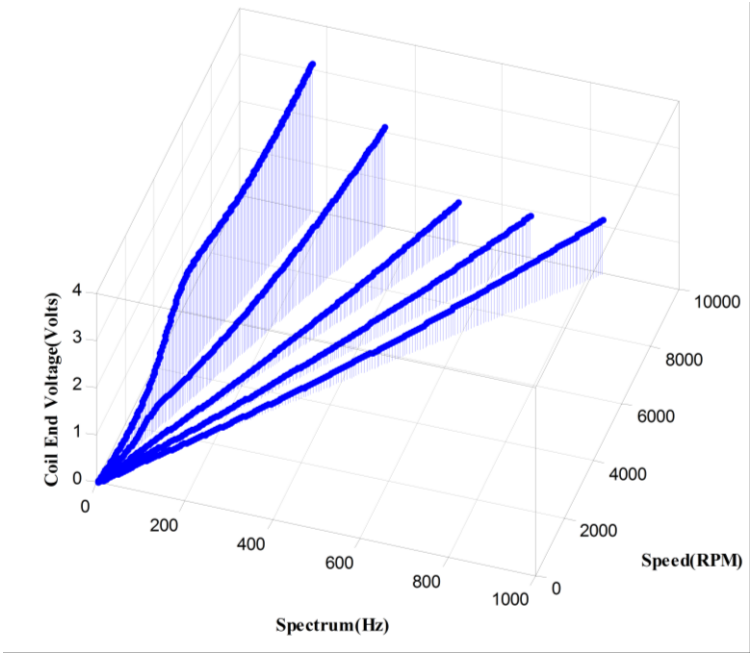

Figure 33 Coil voltage response to sensor runouts

The rotor orbit plot to the sensor runouts is presented in Figure 34.

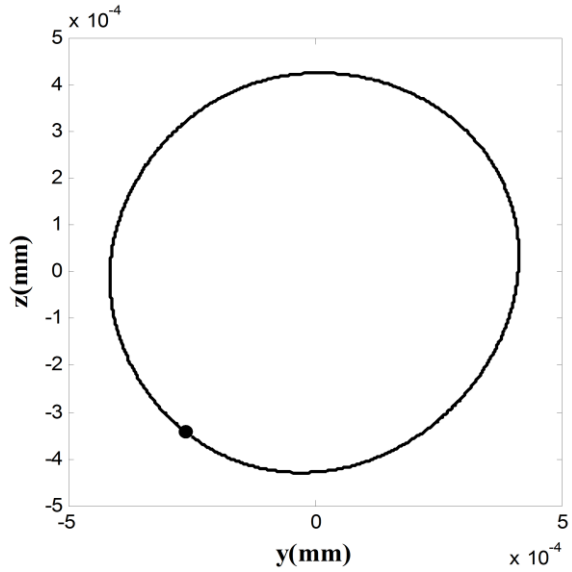

Figure 34 Rotor orbit plot to sensor runouts

4.2.4 Unbalance transient analysis

The unbalance transient analysis is conducted with a rotor unbalance located at the center of gravity of the rotor and phased to create the maximum synchronous response amplitude, as required by API617. Unbalance transient analysis is conducted when the mass center of the rotor (*G*) is shifted away from the spin (geometric) center (*P*) by the imbalance eccentricity distance *e*, as is shown in Figure 35. The spin speed of the rotor is ω and the phase angle of the rotor unbalance is ϕ. The induced amount of the unbalance force is $me\omega^2\cos(\phi)$ in y-axis direction and $me\omega^2\sin(\phi)$ in z-axis direction, where me is the unbalance amount in terms of mass and eccentricity. The transient analysis of rotor unbalance is conducted by solving equation (17) with the unbalance forces assembled into the right hand side as external forces.

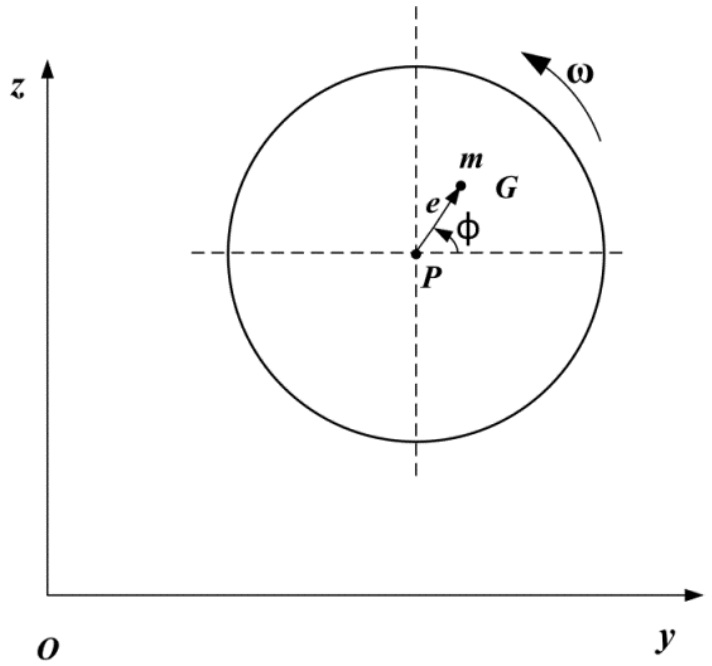

Figure 35 Rotor unbalance diagram

In this example, the unbalance transient analysis is run at the rotor speed of 3,600 rpm, with1.5kg·mm unbalance at the center of the bearing in –z direction, which induces an unbalance force equivalent to 10% of the rotor weight at the spin speed.

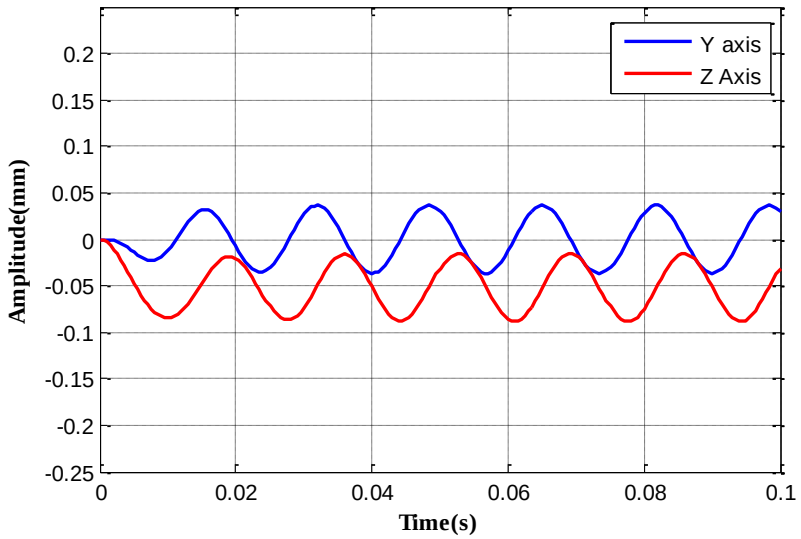

Figure 36 Unbalance transient plot of the homopolar AMB system

4.2.5 Waterfall diagram

Waterfall diagram is a three-dimensional plot of spectra at various machine speeds to show how vibration changes in time or during transient events. The sequential spectra are separated by uniform increments in speed. The plot suggests the frequency-speed of rotation interface diagram, and allows the analyst to evaluate the various frequency components of vibration as the rotor runs up to the operating speed. The waterfall diagram is plotted from an FFT analyzer.

The waterfall diagram for this example case is presented in Figure 37, which shows a first spectrum caused by the rotor unbalance as defined in the unbalance transient analysis.

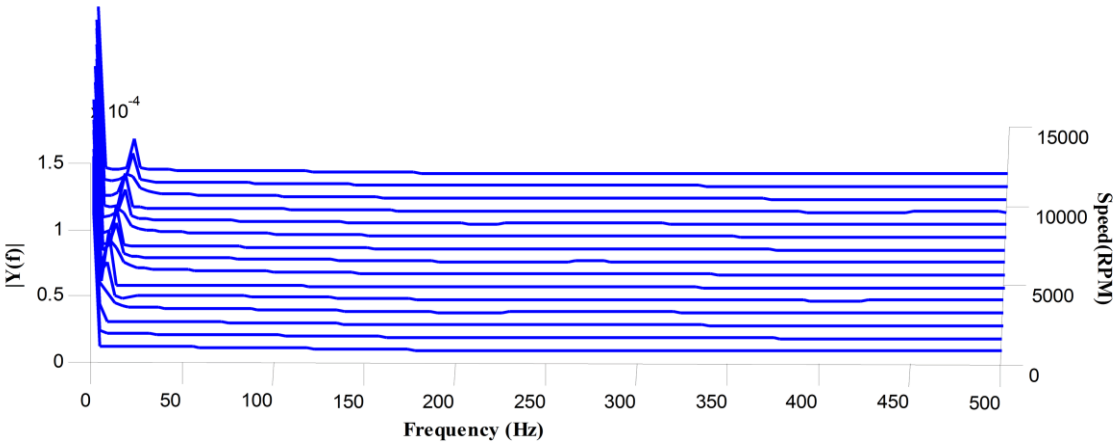

Figure 37 Waterfall plot of the system

4.2.6 Startup transient analysis

The startup transient analysis, also called levitation analysis, simulates the transient process of the rotor lifted by the magnetic bearing from an initial position. Generally, the rotor rests on catcher bearings before the system is powered and the magnetic bearings start working. In the linear simulation, there is no catcher bearing. The catcher bearing in Figure 38 is only there to indicate the initial bearing position and to make a comparison with the nonlinear simulation later. Figure 38 shows successful levitation of the rotor from the initial position.

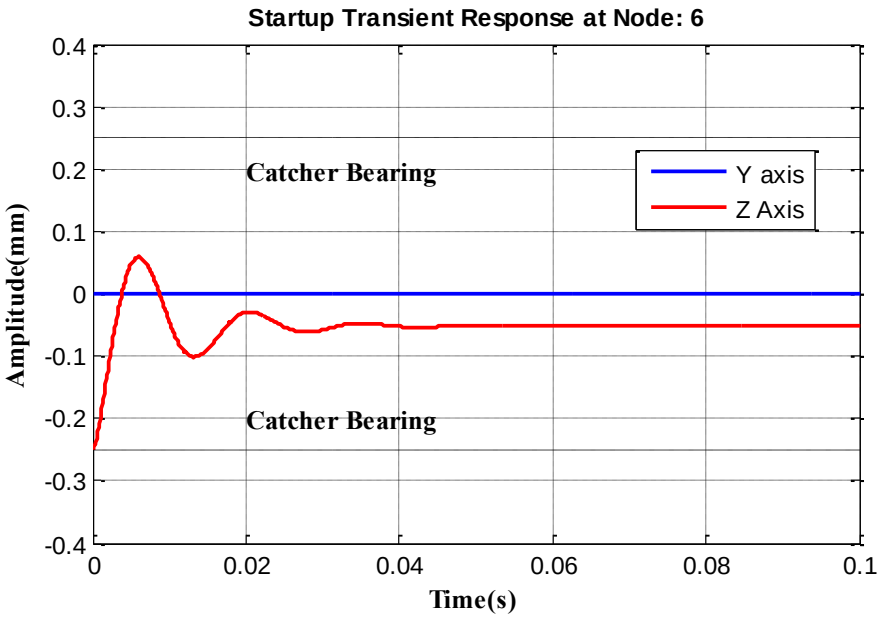

Figure 38 Startup transient analysis of the homopolar AMB system

Figure 39 plots the magnetic bearing force, the current in the power amplifier, and the voltage of the power amplifier during the levitation. In the levitation, due to the rapid change of the displacement, the magnetic bearing force can be very large, resulting in large power amplifier current and voltage. It clears shows that the maximum power amplifier current is as large as 45.3 *amps*, and the peak power amplifier voltage is 492.3 *volts*, which exceed the limits of real power amplifiers. Also, the flux intensity in the poles might also be saturated in the levitation to supply large magnetic bearing force, which cannot be simulated by the linear code. Thus the linear code cannot be reliable to predict the performance of the magnetic bearing- rotor system, and more dedicated nonlinear analysis is required.

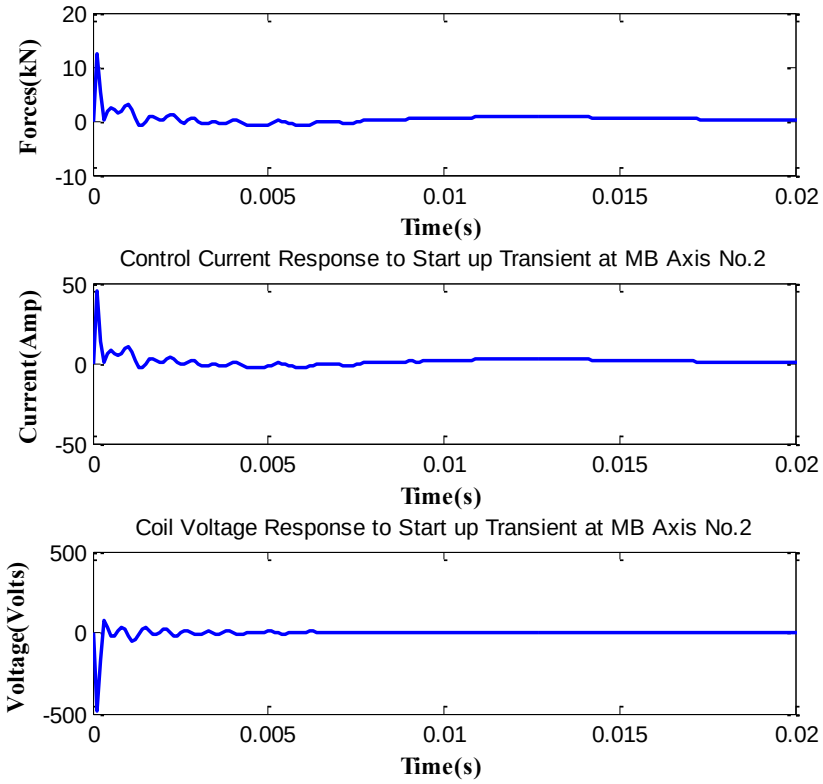

Figure 39 Magnetic bearing force, power amplifier current, power amplifier voltage in the startup analysis

4.3 Nonlinear Rotordynamic Analysis

While many of the current research and modeling of magnetic bearings use linear analysis, the actual magnetic bearing supported rotordynamic system is nonlinear. The nonlinearities might come from:

1) the magnetic bearing force as a nonlinear function of the rotor displacement and the coil current;
2) rotor and stator ferromagnetic material saturation effects;
3) the saturation of current and voltage in the power amplifier;
4) the catcher bearing, sensor runouts and so on.

In linear analysis, the magnetic bearing force is linearized at the centered position and assuming no control current. Thus the flux intensity is not limited in the linear analysis. In the nonlinear analysis, a nonlinear BH curve is used for the magnetic bearing force calculation with the maximum flux intensity. A nonlinear power amplifier with saturation effects of both current and voltage is used, which has been talked in Section 2.

The catcher bearing (also known as an auxiliary, back-up or touchdown bearing) is a ball bearing with clearance between its inner space and the rotor. It is designed to prevent the unexpected contact between the rotor and stator of the magnetic bearing in cases of overload or failure of the magnetic bearing.

Other effects, such as disturbances in the system, like sensor runout, random noise, imbalance, affects the system. Even the gain control may amplify effects of disturbances to cause saturation. Besides all these, saturation may cause a "nonlinear" instability due to increased phase lag, large limit cycle or erratic vibrations.

4.3.1 Levitation simulation with catcher bearing

Magnetic bearings rest on catcher bearings before startup. In the levitation, the magnetic bearings lift the rotor from the initial position at zero spin speed.

In this simulation, the catcher bearing is simplified as a spring-damping model with tangential friction force, and defined by the spring stiffness, damping ratio, and the tangential friction coefficient. The catcher bearing clearance is half of the centered air gap clearance. High fidelity modeling of the catcher bearing drop events with life

prediction, which provides a specified number of safe stops from full speed or worst case load conditions, will be conducted in the future.

Figure 40 shows the forces of the linearized spring-damper catcher bearing model. O is the center of the centered rotor/catcher bearing center, O' is the eccentric rotor center, R_r is the rotor radius, and R_{cb} is the catcher bearing radius, θ is the angle of the whirl motion of the rotor center inside the catcher bearing, ϕ is the counter clockwise rotation motion of the shaft, and $\dot{\phi}$ is the spin velocity.

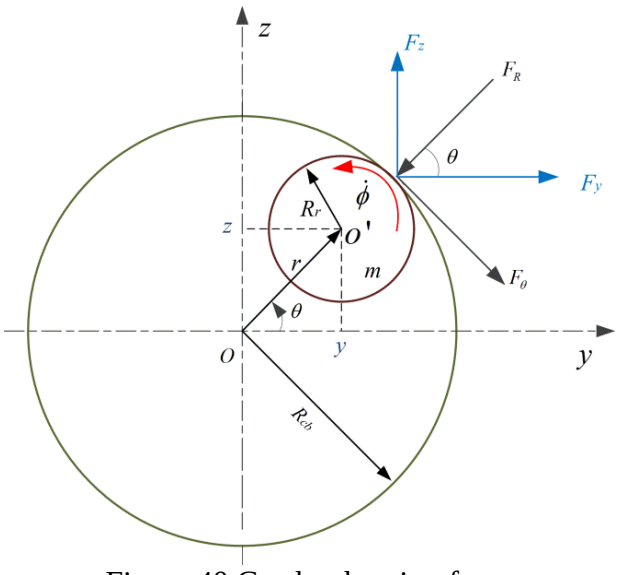

Figure 40 Catcher bearing force

Here

$$r = \sqrt{y^2 + z^2} \tag{72}$$

where y and z are the translational displacements of the rotor. The normal force is consisted of force induced by the linear spring with stiffness K_{cb} and the damper with the damping coefficient C_{cb}, which can be expresses as:

$$F_R = K_{cb} r + C_{cb} \frac{dr}{dt} \tag{73}$$

Substitute equation (38) into (39), the normal force on the catcher bearing is

$$F_R = K_{cb}(\sqrt{y^2 + z^2} + R_r - R_{cb}) + C_{cb} \frac{y\dot{y} + z\dot{z}}{\sqrt{y^2 + z^2}} \tag{74}$$

where R_r is the rotor radius at the catcher bearing locations, and C_g is the catcher bearing radius, and $R_{cb} - R_r = C_g$, which is the catcher bearing clearance. Then the normal force F_R can be expressed as

$$F_R = K_{cb}(\sqrt{y^2 + z^2} - C_g) + C_{cb} \frac{y\dot{y} + z\dot{z}}{\sqrt{y^2 + z^2}} \tag{75}$$

The tangential friction force is:

$$F_\theta = \mu_f F_R \tag{76}$$

where μ_f is the Coulomb friction force coefficient. When $y > 0$ and $z > 0$, forces in y and z directions are:

$$F_y = -F_R \cos\theta + F_\theta \sin\theta \tag{77}$$

$$F_z = -F_R \sin\theta - F_\theta \cos\theta \tag{78}$$

Substitute (41) and (42) into (43) and (44), the y and z directions forces are

$$F_y = [K_{cb}(\sqrt{y^2+z^2} - C_g) + C_{cb}\frac{y\dot{y}+z\dot{z}}{\sqrt{y^2+z^2}}]\frac{-y+\mu_f z}{\sqrt{y^2+z^2}} \tag{79}$$

$$F_z = -[K_{cb}(\sqrt{y^2+z^2} - C_g) + C_{cb}\frac{y\dot{y}+z\dot{z}}{\sqrt{y^2+z^2}}]\frac{-z+\mu_f y}{\sqrt{y^2+z^2}} \tag{80}$$

Torque caused by the friction force in the θ direction:

$$T_\theta = -R_r \cdot F_\theta = -R_r\mu_f[K_{cb}(\sqrt{y^2+z^2} - C_g) + C_{cb}\frac{y\dot{y}+z\dot{z}}{\sqrt{y^2+z^2}}] \tag{81}$$

The tangential friction forces and torque induced by the catcher bearing are assembled into the right side of the MCK equation as external forces at the nodes where the catcher bearing are located, and transient analysis of the equation is conducted when the rotor is at zero spin speed.

As has been stated, due to the rapid change of displacement in the levitation simulation, the magnetic force can be very large, causing saturation in the power amplifier and flux intensity. As a result, the nonlinear analysis for the levitation process with a limited power amplifier voltage and current, as well as a BH curve with saturation, is required.

4.3.2 Unbalance transient analysis

For most of the case, unbalance would not be large enough to cause saturation in the flux intensity or the power amplifier. So the difference between the linear and nonlinear unbalance transient analysis is caused by the linearization of the magnetic

bearing force with respect to the displacement and current, which is supposed to be small.

But when there is large external load applied, the system could be highly saturated. In this case, the linear and the nonlinear analysis result could be very different.

Example cases of the nonlinear analysis, with the saturation model included, will be given in section 8.

4.4 Linear and Nonlinear Analysis Comparison Example

The significance of nonlinear analysis has been stated. In this part, an example case run with linear and nonlinear code for transient simulation is presented.

The rotor model used in this example is given in Figure 41. The heavy rotor is 2m in length with a mass of 624.4kg. The first structure damping ratio is 0.1 at 126rad/s spin speed and the 2^{nd} structure damping ratio is 0.1 at 6283rad/s. The radial magnetic bearings are located at node 7 and node 21. The non-collocated sensors are located at node 6 and node 20, respectively, which are next to the bearing nodes. Disks are added on the rotor, which are treated as added mass.

The heteropolar "C" core magnetic bearings are used, with a position stiffness of -1.19E7 N/m and a current stiffness of 7637.1 N/Amp for linear analysis.

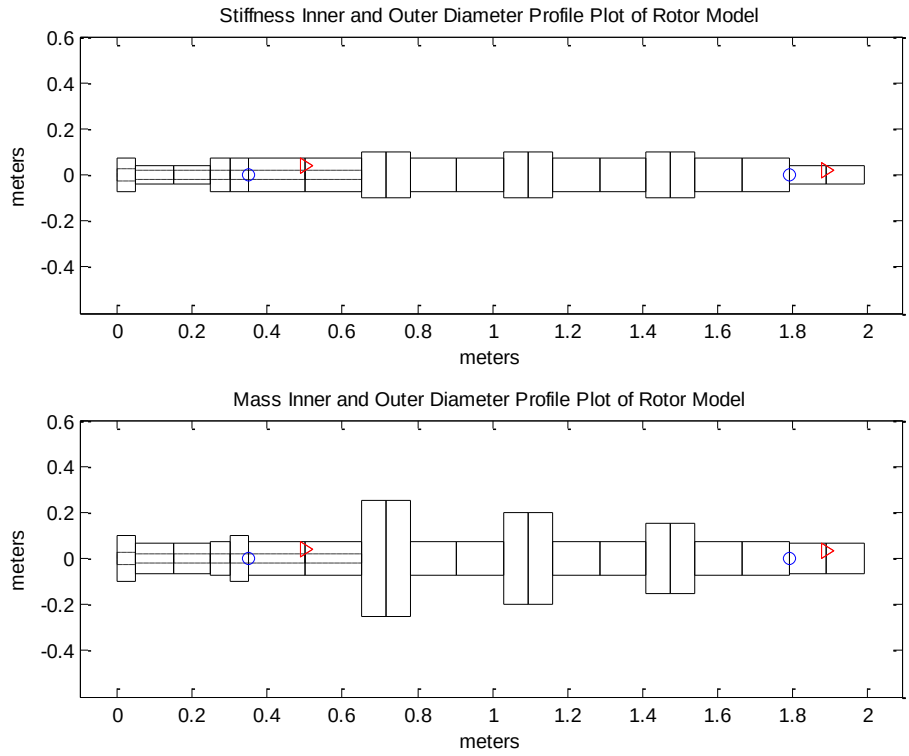

Figure 41 Rotor profile with added disk and non-collocated sensor and actuator

More details of the actuator parameters are presented in Table 3 for nonlinear force calculation.

Table 3 Magnetic bearing actuator parameters for linear & nonlinear comparison case

Flux area	$A_g\ (m^2)$	1.00E-02
Air gap	$L_g\ (m)$	5.00E-04
Flux path in stator	$L_s\ (m)$	0.2
Flux path in rotor	$L_r\ (m)$	0.25
Number of coil turns	N	500
Bias current	$I_b\ (Amp)$	1
Permeability in stator	$\mu_s(H/m)$	0.002
Permeability in rotor	$\mu_r(H/m)$	0.002

The sensor DC gain is 8V/mm, with a high 1st order cut off frequency of 10E5 Hz. The resulting transfer function of the sensor is

$$TF_{sensor}(s) = \frac{5.03\text{E}9}{s + 6.28E5} \tag{82}$$

The PD controller is used, with a transfer function of the form

$$TF_{PD}(s) = \frac{0.1368 + 1.3712\text{E} - 5s}{(1E - 5s + 1)^3} \tag{83}$$

In the linear analysis, the power amplifier is modeled as a DC gain of 1.56 Amp/V with 1st order low pass filter with a cut off frequency of 960 Hz. In the transfer function form,

$$TF_{PA}(s) = \frac{9.4248E3}{s + 6.0328E3} \tag{84}$$

In the nonlinear analysis, the voltage limit of the power amplifier is set to be 80V, and the current limit is set to be 10Amp. The coil inductance is 0.002H, and the coil resistance is 0.5Ω. The nonlinear BH curve used is as shown in Figure 6, with the transient flux intensity of 2 Tesla and the maximum flux intensity of 2.3 Tesla. The material permeability for flux intensity under 2 Tesla is 0.016 H/m, and 0.000051064 H/m for flux intensity between 2 Tesla to 2.3 Tesla.

For levitation simulation, the rotor's initial vertical position is -2.5E-4 m. The target is to levitate the rotor to the centered position with a vertical displacement of 0. The levitation result for both linear and nonlinear is shown in Figure 42.

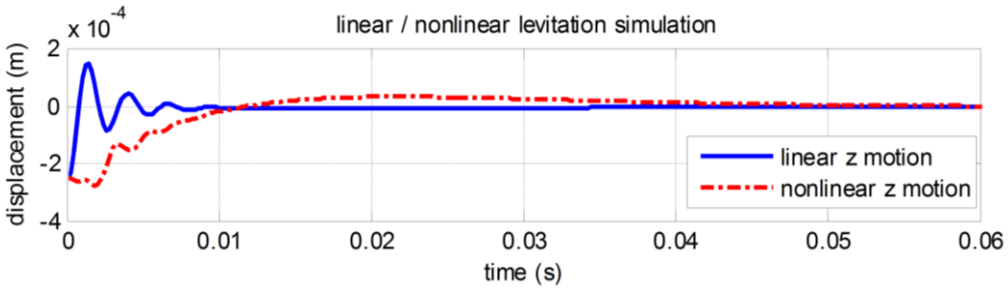

Figure 42 Linear and nonlinear code levitation simulation comparison

Control currents corresponding to the magnetic bearings located at node 7 and node 21 in the vertical direction are plotted for comparison as shown in Figure 43. The figure shows different current behavior of the power amplifiers in the linear analysis and in the nonlinear analysis, even though the currents do not exceed the limit of the power amplifier.

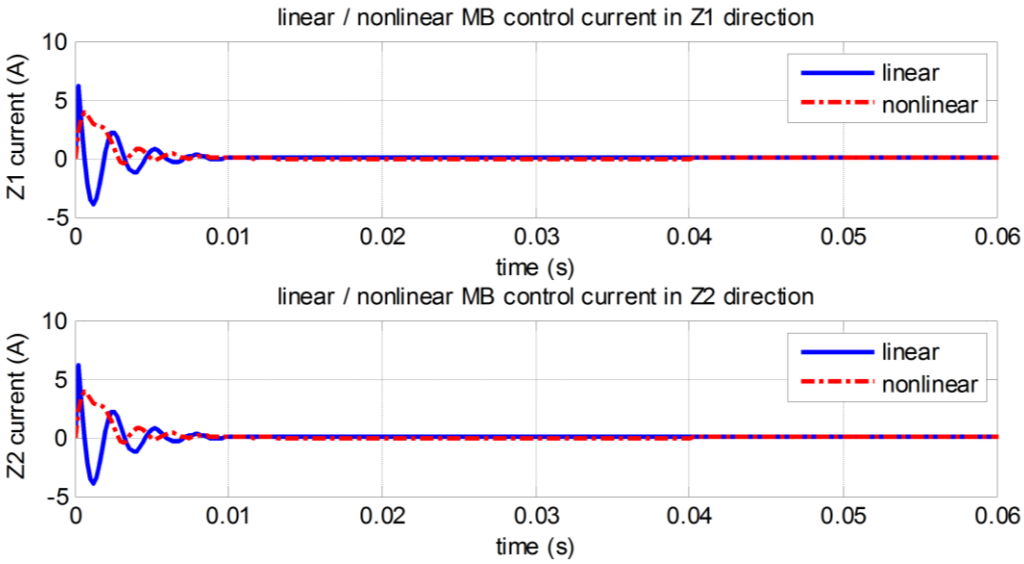

Figure 43 Linear and nonlinear code levitation simulation comparison_ control current

The flux intensities corresponding to the magnetic bearings at node 7 in the upper cores and the lower cores are plotted in Figure 44. It clearly shows that in the lower cores, the maximum flux intensity exceeds 2 Tesla, which means that the B-H curve goes into the nonlinear range and there is flux intensity saturation. This explains the differences of the motion and current in the linear and nonlinear analysis.

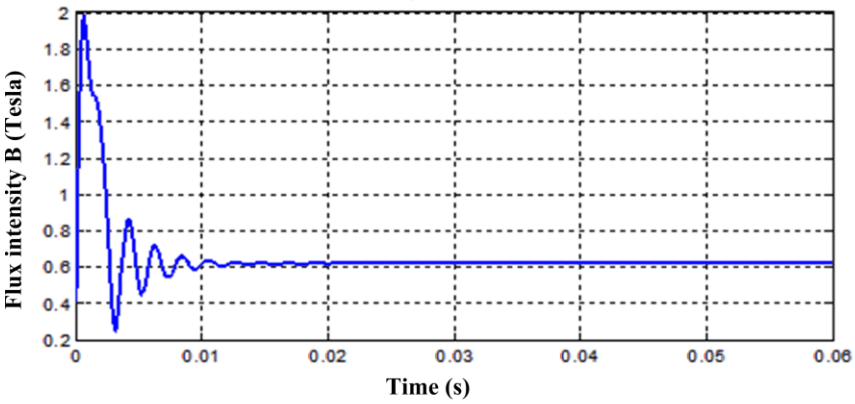

(a) flux intensity in the upper cores

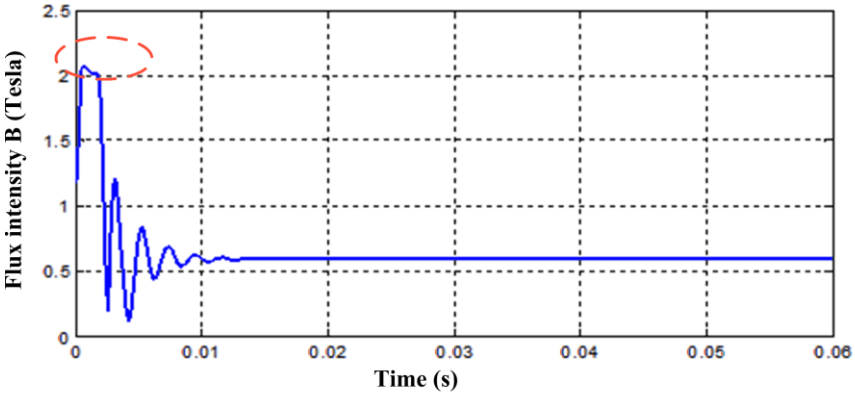

(b) flux intensity in the lower cores

Figure 44 Flux intensity in the nonlinear levitation simulation in the upper cores and the lower cores

5. FLEXIBLE SUPPORT ANALYSIS OF AMB SYSTEM

The bearing support structure may have a big effect on the rotating machinery behavior by altering the effective bearing stiffness and the damping properties. Vazquez et al. [26, 27]experimentally studied the effects of the bearing support flexibility on rotor stability and unbalance response with fluid film bearings, and demonstrated that the analysis of machine vibration response based on rigid bearing supports predict critical speeds that are substantially higher than actual values. Nicholas et al. [28]included the flexible supports using experimentally measured compliance frequency response function (FRF), and presented an improvement in the calculation of the critical speeds using the method. API 617 stated that if the foundation flexibility is less than 3.5 times the bearing stiffness, then a foundation model should be included.

This study gives an analytical way to predict the magnetic bearing supported rotor system properties with flexible support.

5.1 Dynamics of Flexible Support

A typical simplified outline of the AMB support is displayed in Figure 45. The dynamic characteristics of the support model can be determined experimentally by measuring the response of the support under certain external excitations. The general process is shown in the block diagram in Figure 46. An impact hammer is used to excite the support casing. In a lot of experiments, radial magnetic bearings are used as shakers to generate excitations. The acceleration by the excitation is measured by the signal

conditioner, and is then processed by the modal analyzer to get the displacement caused by the excitation.

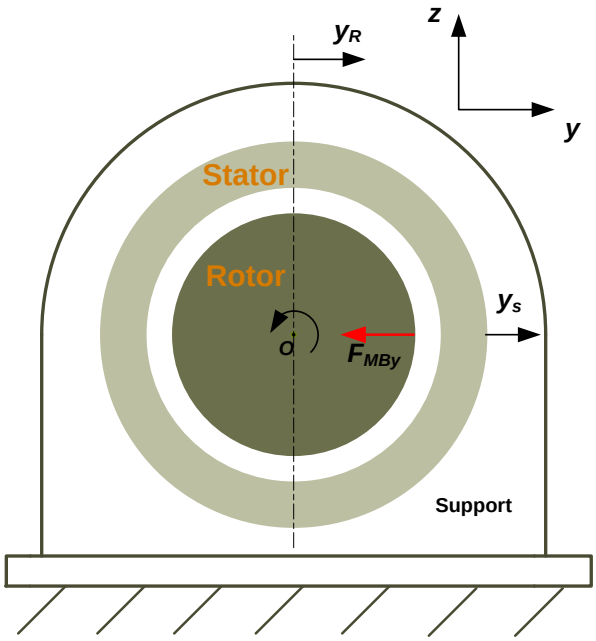

Figure 45 Simplified model plot of the AMB support

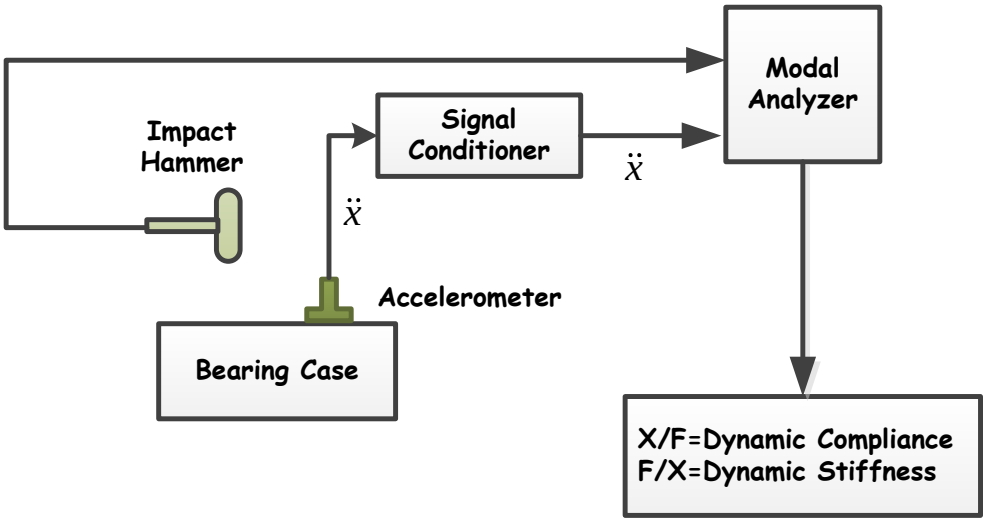

Figure 46 Modal analysis schematic diagram

In this study, we assume that there are two supports, one at each of the magnetic bearing locations. The excitation is applied to each support in the horizontal direction or vertical direction, one direction at a time. Accelerations with a total of 16 are measured, and can be assembled in the matrix as

$$\begin{Bmatrix} \ddot{y}_1 \\ \ddot{z}_1 \\ \ddot{y}_2 \\ \ddot{z}_2 \end{Bmatrix} = \begin{bmatrix} a_{y_1y_1} & a_{y_1z_1} & a_{y_1y_2} & a_{y_1z_2} \\ a_{z_1y_1} & a_{z_1z_1} & a_{z_1y_2} & a_{z_1z_2} \\ a_{y_2y_1} & a_{y_2z_1} & a_{y_2y_2} & a_{y_2z_2} \\ a_{z_2y_1} & a_{z_2y_1} & a_{z_2y_1} & a_{z_2y_1} \end{bmatrix} \begin{Bmatrix} F_{y_1} \\ F_{z_1} \\ F_{y_2} \\ F_{z_2} \end{Bmatrix} \tag{85}$$

The subscripts 1 and 2 refer to support 1 and 2, respectively. The acceleration data is integrated twice to get the displacements. The relations between the response displacements and the excitation forces are be expressed in the form of

$$\begin{Bmatrix} y_1 \\ z_1 \\ y_2 \\ z_2 \end{Bmatrix} = \begin{bmatrix} G_{y_1y_1} & G_{y_1z_1} & G_{y_1y_2} & G_{y_1z_2} \\ G_{z_1y_1} & G_{z_1z_1} & G_{z_1y_2} & G_{z_1z_2} \\ G_{y_2y_1} & G_{y_2z_1} & G_{y_2y_2} & G_{y_2z_2} \\ G_{z_2y_1} & G_{z_2y_1} & G_{z_2y_1} & G_{z_2y_1} \end{bmatrix} \begin{Bmatrix} F_{y_1} \\ F_{z_1} \\ F_{y_2} \\ F_{z_2} \end{Bmatrix} \tag{86}$$

Let $G_{ij} = \begin{bmatrix} G_{y_1y_1} & G_{y_1z_1} & G_{y_1y_2} & G_{y_1z_2} \\ G_{z_1y_1} & G_{z_1z_1} & G_{z_1y_2} & G_{z_1z_2} \\ G_{y_2y_1} & G_{y_2z_1} & G_{y_2y_2} & G_{y_2z_2} \\ G_{z_2y_1} & G_{z_2y_1} & G_{z_2y_1} & G_{z_2y_1} \end{bmatrix}$, and G_{ij} is defined for each excitation frequency. G_{ij} is called dynamic compliance matrix. Each term of G_{ij} is a polynomial transfer function.

In multiple-input-multiple-output control, this frequency dependent matrix G_{ij} can be treated as a transfer function matrix for the stator system, where the input is excitation forces, and the output is the displacement, as shown in Figure 47.

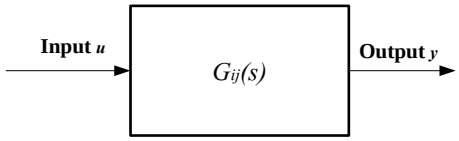

Figure 47 Transfer function matrix diagram of a MIMO system

This transfer function represented stator system can be written in state space form,

$$\begin{aligned} W_{stator} &= A_s W_{stator} + B_s u \\ y &= C_s W_{stator} \end{aligned} \tag{87}$$

where W_{stator} is the state variables of the system, u is the input into the system, and y is the output of the system. In this case, the input $u = \begin{Bmatrix} F_{y_1} \\ F_{z_1} \\ F_{y_2} \\ F_{z_2} \end{Bmatrix}$, and the output $y = \begin{Bmatrix} y_1 \\ z_1 \\ y_2 \\ z_2 \end{Bmatrix}$.

5.2 Flexible Support Assembling into AMB System

The state space representation form of the stator has been derived. To get the rotordynmaic behaviors of the rotor-bearing-support system, the support model needs to be assembled into the system matrix.

As has been stated, the equation of motion of the rotor can be written as

$$\frac{d}{dt}\begin{bmatrix}\dot{U}\\U\end{bmatrix}=\begin{bmatrix}-M^{-1}C & -M^{-1}K\\ I & 0\end{bmatrix}\begin{bmatrix}\dot{U}\\U\end{bmatrix}+\begin{bmatrix}M^{-1}F_{ext}\\0\end{bmatrix} \tag{88}$$

Let $W_0=\begin{bmatrix}\dot{U}\\U\end{bmatrix}$, then the equation of motion is in the form of 1st order differential equation

$$\begin{bmatrix}M & 0\\0 & K\end{bmatrix}\frac{d}{dt}\begin{Bmatrix}\dot{W}_0\\W_0\end{Bmatrix}=\begin{bmatrix}-C & -K\\K & 0\end{bmatrix}\begin{Bmatrix}\dot{W}_0\\W_0\end{Bmatrix}+\begin{Bmatrix}F_{ext}\\0\end{Bmatrix} \tag{89}$$

As a result, the state space representation of the rotor can be written as

$$\begin{bmatrix}M & 0\\0 & K\end{bmatrix}\frac{d}{dt}\begin{Bmatrix}\dot{W}_0\\W_0\end{Bmatrix}=\begin{bmatrix}-C & -K\\K & 0\end{bmatrix}\begin{Bmatrix}\dot{W}_0\\W_0\end{Bmatrix}+TF_{AMB}\begin{Bmatrix}-K_{py1}(y_{r1}-y_{s1})+K_{iy1}i_{cy1}\\-K_{pz1}(z_{r1}-z_{s1})+K_{iz1}i_{cz1}\\-K_{py2}(y_{r2}-y_{s2})+K_{iy2}i_{cy2}\\-K_{pz2}(z_{r2}-z_{s2})+K_{iz2}i_{cz2}\end{Bmatrix} \tag{90}$$

$$\begin{aligned}&\begin{bmatrix}M & 0\\0 & K\end{bmatrix}\frac{d}{dt}\begin{Bmatrix}\dot{W}_0\\W_0\end{Bmatrix}=\begin{bmatrix}-C & -K\\K & 0\end{bmatrix}\begin{Bmatrix}\dot{W}_0\\W_0\end{Bmatrix}\\&-TF_{AMB}K_{p1}\begin{Bmatrix}y_{r1}\\z_{r1}\\y_{r2}\\z_{r2}\end{Bmatrix}+TF_{AMB}K_{p1}\begin{Bmatrix}y_{s1}\\z_{s1}\\y_{s2}\\z_{s2}\end{Bmatrix}+TF_{AMB}K_{i1}\begin{Bmatrix}i_{cy1}\\i_{cz1}\\i_{cy2}\\i_{cz2}\end{Bmatrix}\end{aligned} \tag{91}$$

where $K_{p1}=\begin{bmatrix}K_{py1} & & & \\ & K_{pz1} & & \\ & & K_{py2} & \\ & & & K_{pz2}\end{bmatrix}$, $K_{i1}=\begin{bmatrix}K_{iy1} & & & \\ & K_{iz1} & & \\ & & K_{iy2} & \\ & & & K_{iz2}\end{bmatrix}$, TF_{AMB} is the coordinate selection matrix for the magnetic bearing forces. For a rotor with n nodes and with two radial magnetic bearings located and node i and node j, respectively, the TF_{AMB} is in the form of

$$TF_{AMB} = \begin{bmatrix} 0 & 0 & 0 & 0 \\ 0 & 0 & 0 & 0 \\ \vdots & \vdots & \vdots & \vdots \\ 1 & 0 & 0 & 0 \\ 0 & 1 & 0 & 0 \\ \vdots & \vdots & \vdots & \vdots \\ 0 & 0 & 1 & 0 \\ 0 & 0 & 0 & 1 \\ \vdots & \vdots & \vdots & \vdots \\ 0 & 0 & 0 & 0 \end{bmatrix} \begin{matrix} \\ \\ \\ \leftarrow row = 6(i-1)+2 \\ \leftarrow row = 6(i-1)+3 \\ \\ \leftarrow row = 6(j-1)+2 \\ \leftarrow row = 6(j-1)+3 \\ \\ row = 6(n-1)+3 \end{matrix} \tag{92}$$

The $TF_{AMB}K_{p1}\begin{Bmatrix} y_{r1} \\ z_{r1} \\ y_{r2} \\ z_{r2} \end{Bmatrix}$ term can be written into the form of K_pW_0, as has been

introduced. Let $K' = K + K_p$, then the equation of the rotor can be written as

$$\begin{bmatrix} M & 0 \\ 0 & K' \end{bmatrix} \frac{d}{dt} \begin{Bmatrix} \dot{W}_0 \\ W_0 \end{Bmatrix} = \begin{bmatrix} -C & -K' \\ K' & 0 \end{bmatrix} \begin{Bmatrix} \dot{W}_0 \\ W_0 \end{Bmatrix} + TF_{AMB}K_{p1} \begin{Bmatrix} y_{s1} \\ z_{s1} \\ y_{s2} \\ z_{s2} \end{Bmatrix} + TF_{AMB}K_{i1} \begin{Bmatrix} i_{cy1} \\ i_{cz1} \\ i_{cy2} \\ i_{cz2} \end{Bmatrix} \tag{93}$$

The system electronics, including the sensors, the controllers, the filters, the power amplifiers, and the actuators, are assembled into one state space equation in the form of

$$\begin{aligned} \dot{W}_{MB} &= A_{MB}W_{MB} + B_{MB}u_{MB} \\ y_{MB} &= C_{MB}W_{MB} \end{aligned} \tag{94}$$

where $W_{MB} = [W_{sen}W_{con}W_{pa}W_{act}W_{filter}]^T$. The output and input of the state space form depend on the electronics represented. The inputs into the sensors are relative

displacements between the rotor and the sensors, $\begin{Bmatrix} y_{r1}-y_{s1} \\ z_{r1}-z_{s1} \\ y_{r2}-y_{s2} \\ z_{r2}-z_{s2} \end{Bmatrix}$. The control currents,

$\begin{Bmatrix} i_{cy1} \\ i_{cz1} \\ i_{cy2} \\ i_{cz2} \end{Bmatrix}$ are the output of the controllers. They can be extracted from the output of the

electronics system y_{MB}. The support model is in the form of

$$\begin{aligned} \dot{W}_s &= A_s W_s + B_s u_s \\ \begin{Bmatrix} y_{s1} \\ z_{s1} \\ y_{s2} \\ z_{s2} \end{Bmatrix} &= C_s W_s \end{aligned} \tag{95}$$

where u_s is the input of the support system, which is the magnetic bearing force in this case. In this case, we are demonstrating the effects from the dynamics of the support model, so the cross-coupling stiffness of the magnetic bearing is neglected. The support model is

$$\dot{W}_s = A_s W_s + B_s \begin{Bmatrix} F_{MBy1} \\ F_{MBz1} \\ F_{MBy2} \\ F_{MBz2} \end{Bmatrix} = A_s W_s + B_s \begin{Bmatrix} -K_{py1}(y_{r1}-y_{s1}) + K_{iy1} i_{cy1} \\ -K_{pz1}(z_{r1}-z_{s1}) + K_{iz1} i_{cz1} \\ -K_{py2}(y_{r2}-y_{s2}) + K_{iy2} i_{cy2} \\ -K_{pz2}(z_{r2}-z_{s2}) + K_{iz2} i_{cz2} \end{Bmatrix} \tag{96}$$

$$\dot{W}_s = A_s W_s - B_s K_{p1} \begin{Bmatrix} y_{r1} \\ z_{r1} \\ y_{r2} \\ z_{r2} \end{Bmatrix} + B_s K_{p1} \begin{Bmatrix} y_{s1} \\ z_{s1} \\ y_{s2} \\ z_{s2} \end{Bmatrix} + B_s K_{i1} \begin{Bmatrix} i_{cy1} \\ i_{cz1} \\ i_{cy2} \\ i_{cz2} \end{Bmatrix} \tag{97}$$

Assemble the rotor, the electronics, and the support into a whole system equation, considering that

$$\begin{Bmatrix} y_{r1} \\ z_{r1} \\ y_{r2} \\ z_{r2} \end{Bmatrix} = TF_{AMB} W_0, \begin{Bmatrix} y_{s1} \\ z_{s1} \\ y_{s2} \\ z_{s2} \end{Bmatrix} = C_s W_s, \text{ and } \begin{Bmatrix} i_{cy1} \\ i_{cz1} \\ i_{cy2} \\ i_{cz2} \end{Bmatrix} = TM_{MB} W_{MB}$$

where TM_{MB} is the transform matrix from the electronics system to the control current, which depends on the states represented by the controllers.

The final equation of the whole system is in the form of

$$\begin{bmatrix} M & & & \\ & K & & \\ & & I & \\ & & & I \end{bmatrix} \frac{d}{dt} \begin{Bmatrix} \dot{W}_0 \\ W_0 \\ W_{MB} \\ W_s \end{Bmatrix} = \begin{bmatrix} -C & -K & TM_{MB}C_{MB} & TF_{AMB}K_{p1}C_s \\ K & 0 & 0 & 0 \\ 0 & B_{MB} & A_{MB} & -B_{MB}TF_{AMB}C_s \\ 0 & -B_s K_{p1} TF_{AMB}' & B_s C_{MB} & A_s + B_s K_{p1} C_s \end{bmatrix} \begin{Bmatrix} \dot{W}_0 \\ W_0 \\ W_{MB} \\ W_s \end{Bmatrix} \quad (98)$$

The system stability (eigenvalue analysis), unbalance transient analysis, and forced harmonic responses can be obtained by solving this system equation.

5.3 Rigid Support and Flexible Support Comparison

The comparison between the rigid support and flexible support was based on the heteropolar “C” core magnetic bearings, and the coil turn was set to be 100, and the bias current was 6 Amps, and resulting position stiffness was -3.6E6 N/m, current stiffness was 353.8 N/Amp. According to API 617, if the foundation flexibility is less than 3.5

times the bearing stiffness, then a foundation model should be included. For magnetic bearings, the bearing stiffness should be effective stiffness, which includes the effects from the sensor, power amplifier, PD controller and the actuator, rather than simply the position stiffness or the current stiffness. The effective stiffness of a heteropolar "C" core magnetic bearing is in the form of

$$K_{effective} = K_p + K_i \mathrm{G}_{pa} \mathrm{G}_p \mathrm{G}_{sensor} \tag{99}$$

where K_p is the position stiffness, K_i is the current stiffness, G_{pa} is the power amplifier stiffness, G_p is the proportional gain of the PD controller, and G_{sensor} is the sensor gain. In this example case, the resulting effective stiffness of the magnetic bearing is 1.197E7 N/m. A flexible support model is described by the compliance frequency response function (FRF), and defined as a transfer function matrix G_{ij}. In the study performed by Vazquez et al., a highly cross-coupled support transfer function matrix G_{ij} with 24^{th} order transfer functions were obtained through measurements. Example cases with low order transfer functions in G_{ij} are run and compared with flexible support model, to demonstrate the effects induced by the dynamics of the support as well as the cross-coupled stiffness. Three example cases are given here.

In the 1^{st} case, assume that there is no cross-coupled term in the G_{ij} matrix. The support has a static direct stiffness of 1.8E7 N/m in both the horizontal and the vertical directions, which is equivalent to twice of the magnetic bearing effective stiffness. Resulting a simple matrix G_{ij} in the form of

$$G_{ij} = \frac{1}{10s^2 + 100s + 2.394E7}\begin{bmatrix} 1 & 0 & 0 & 0 \\ 0 & 1 & 0 & 0 \\ 0 & 0 & 1 & 0 \\ 0 & 0 & 0 & 1 \end{bmatrix} \tag{100}$$

The resulting unbalance responses of the rotor at node 6, where the magnetic bearings are located, are plotted in Figure 48 and compared with the one with rigid support model.

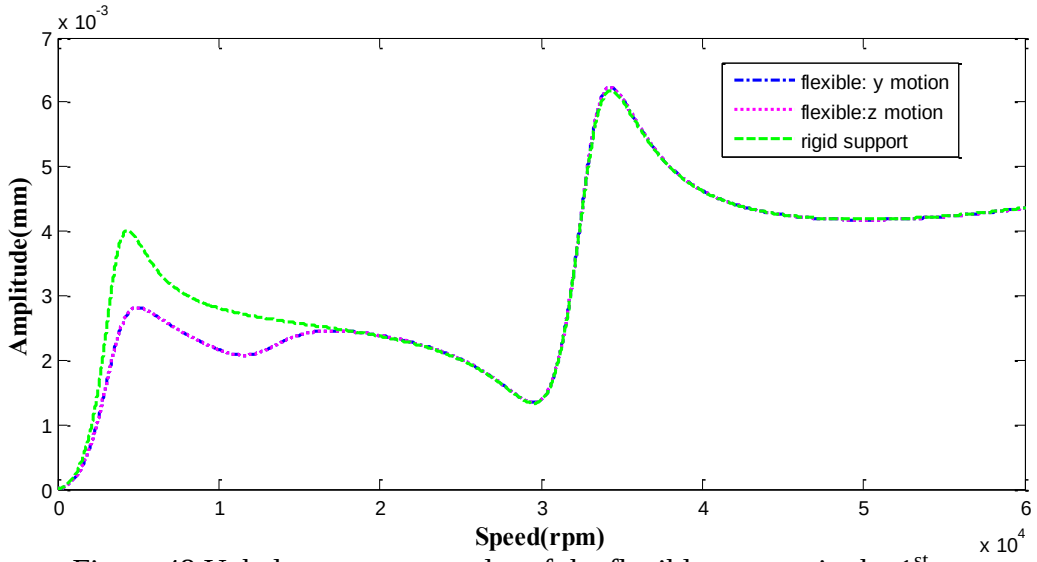

Figure 48 Unbalance response plot of the flexible support in the 1st case

The 2nd case increases the support stiffness to 6 times the effective stiffness of the magnetic bearings, resulting G_{ij} in the form of

$$G_{ij} = \frac{1}{10s^2 + 100s + 7.2E7}\begin{bmatrix} 1 & 0 & 0 & 0 \\ 0 & 1 & 0 & 0 \\ 0 & 0 & 1 & 0 \\ 0 & 0 & 0 & 1 \end{bmatrix} \tag{101}$$

The resulting unbalance responses of the rotor at node 6, where the magnetic bearings are located, are plotted in Figure 49 and compared with the one with rigid support model.

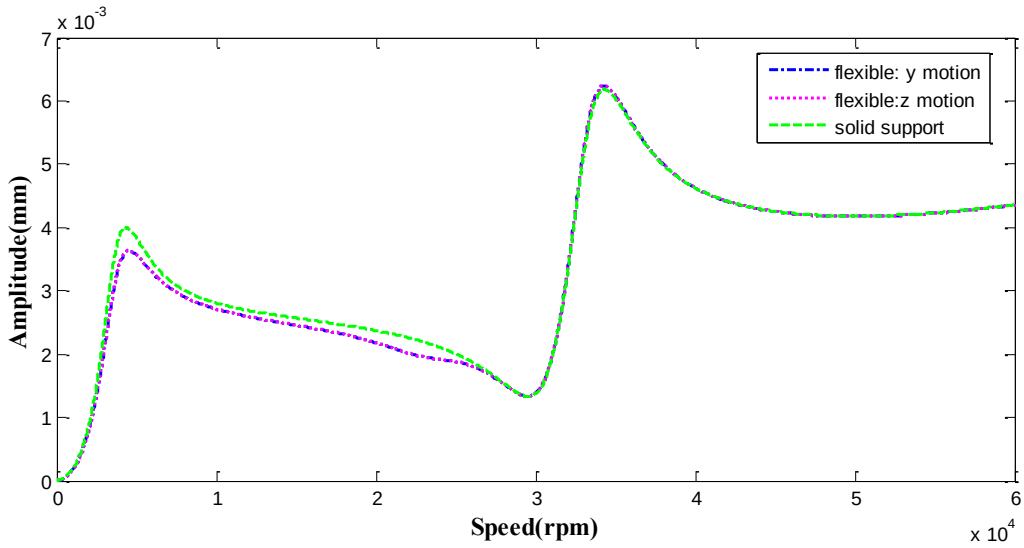

Figure 49 Unbalance response plot of the flexible support in the 2nd case with increased support static stiffness

The 3rd case introduces cross-coupled support dynamics into the matrix, making the G_{ij} in the form of

$$G_{ij} = \begin{bmatrix} \frac{1}{10s^2+100s+K_1} & \frac{1}{10s^2+100s+K_2} & 0 & \frac{1}{10s^2+100s+K_2} \\ 0 & \frac{1}{10s^2+100s+K_1} & 0 & 0 \\ 0 & 0 & \frac{1}{10s^2+100s+K_1} & 0 \\ \frac{1}{10s^2+100s+K_2} & 0 & 0 & \frac{1}{10s^2+100s+K_1} \end{bmatrix} \quad (102)$$

where $K_1 = 7.2E7$, representing a direct stiffness of the support of $7.2E7N/m$, and $K_2 = 7.2E8$, representing a cross-coupled static stiffness of $7.2E8N/m$. The resulting unbalance responses of the rotor at node 6, where the magnetic bearings are located, are plotted in Figure 50 and compared with the one with rigid support model. The plot indicates that the cross-coupled dynamic compliances increase the amplitude of the rotor response to unbalance, thus should be considered in real applications.

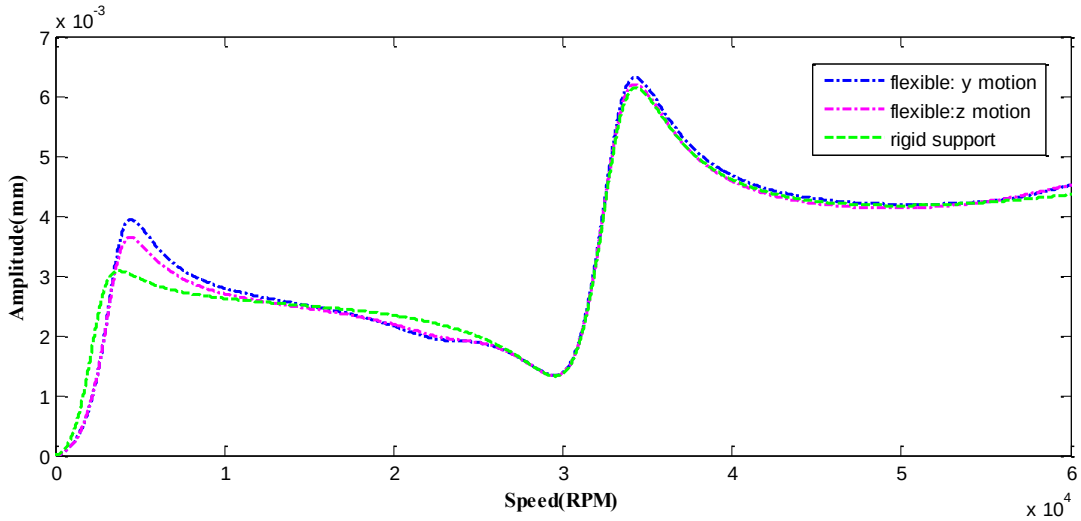

Figure 50 Unbalance response plot of the flexible support in the 3rd case with cross-coupled support static stiffness

An unbalance transient simulation with the support model in the 2nd case is conducted. The result is shown in Figure 51, which shows that the rotor is unstable with this support model.

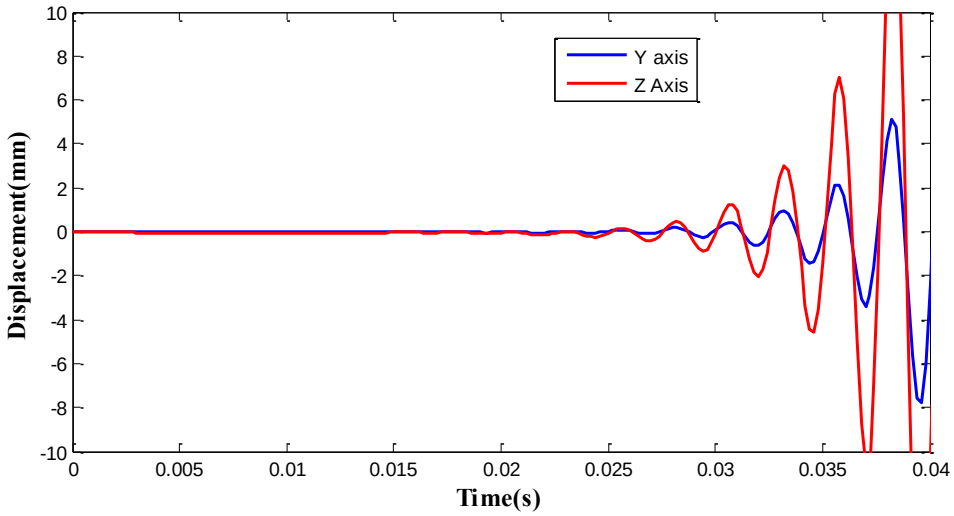

Figure 51 Unstable unbalance transient simulation with flexible support

Increase the coefficient of 's' term, which is equivalent to adding damping into the support model while keeping the mass and static stiffness terms, the resulting G_{ij} is in the form of

$$G_{ij} = \frac{1}{10s^2 + 10000s + 7.2E7}\begin{bmatrix} 1 & 0 & 0 & 0 \\ 0 & 1 & 0 & 0 \\ 0 & 0 & 1 & 0 \\ 0 & 0 & 0 & 1 \end{bmatrix} \tag{103}$$

The unbalance transient simulation is shown in Figure 52, which shows that the rotor is stable with added damping in the support model.

These two examples of unbalance transient simulation shows that different transfer functions of the support could affect the rotor behavior significantly. Even with same static stiffness of the support, different higher order terms in the transfer function (corresponds to support damping in these two examples) might lead to totally different behaviors of the rotor. Thus an accurate description of the support model, either through

simulation or experimental measurements, is very important in predicting rotordynamic performances.

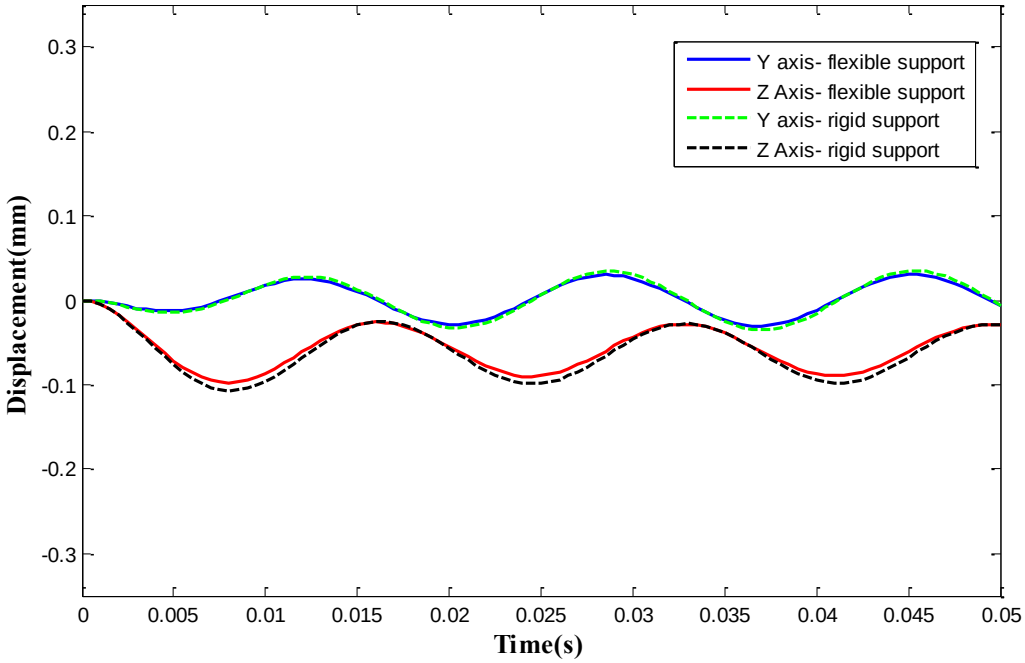

Figure 52 Stable unbalance transient simulation and comparison to the rigid support

5.4 Conclusions for Flexible Support

This section presents a state space representation method to describe the behavior of the flexible support, explains how the support model is assembled into the system, and shows that the dynamic flexibility in the support could lead to totally different rotordynamic behaviors. Examples in which flexible support is modeled with simple and low order transfer functions demonstrated that an accurate description of the support model, either obtained through simulation or experimental measurements, is very important in predicting rotordynamic performances.

6. POWER LOSS AND THERMAL FIELD ANALYSIS

Improving the energy efficiency and reducing the power loss are always a major concern of the turbomachinery area. Due to the non-contact mechanism of magnetic bearings, the power loss of the magnetic bearing supported system is much lower than the conventional bearing supported ones without friction loss. However, the uniqueness of the magnetic bearings introduces other power loss sources, like hysteresis loss and eddy current loss. This part will talk about numerical calculation of the power loss of the magnetic bearing system in the steady state operation of the rotor.

Magnetic bearings have broad applications under extreme environments because no lubrication is required in the system. Successful application of magnetic bearings demonstrated a temperature as high as 1000 degrees Fahrenheit. This part will show a two-dimensional thermal field analysis of the actuator in the steady state operation of the rotor with finite element method.

6.1 AMB System Power Loss Analysis

This part talks about the numerical method to determine the power losses in the magnetic bearing-rotor system. Figure 53 shows the power losses of the total bearing-rotor and electronics system, which come from the actuator, rotor, power amplifier and long cables. Cable loss only exists in long cables, thus is generally ignored. As has been talked, power amplifiers can be as efficient as 98%. As a result, the power loss analysis counts the actuator loss and the rotor loss.

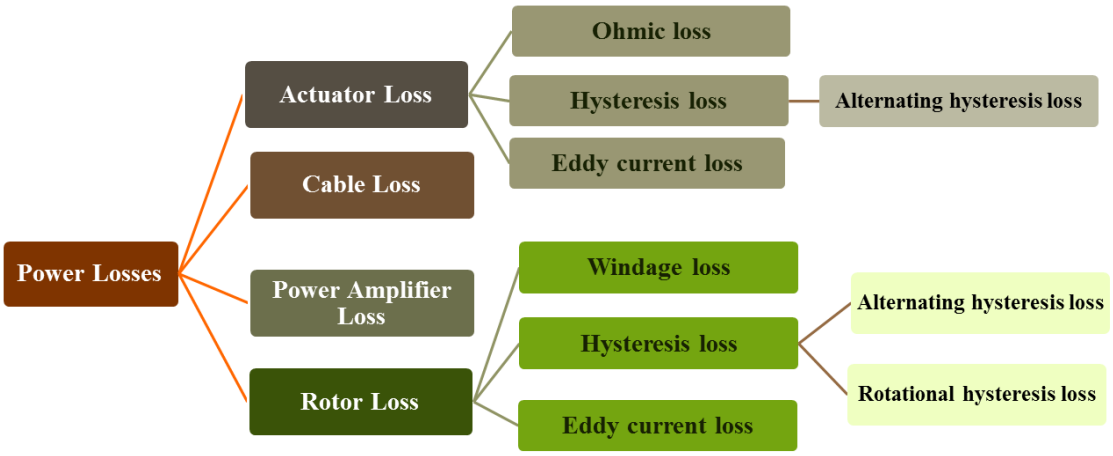

Figure 53 Power losses in the magnetic bearing supported system

6.1.1 Power loss in the rotor

The main losses in the rotor of the magnetic bearings supported system include: eddy current loss, hysteresis loss including both alternating hysteresis loss and rotational hysteresis loss, and windage loss. [29]

Rotational hysteresis loss in the magnets is caused by the change of the orientation of the magnetic field with respect to the material. The rotational hysteresis loss is calculated based on a linear curve fit of the experiment data (Brailsford (1938)), which is expressed by:

$$P_{hr} = (3000B_{\max} - 500) f_r M_{vrh} 10^{-1} (watts / m^3) \quad (104)$$

Here, M_{vrh} is the effective volume coefficient for the rotational hysteresis phenomenon, f_r is the effective rotational hysteresis frequency in H_z, which is 4 times of the rotational frequency for an 8-pole heteropolar AMB, $B_{\max}$ is the maximum flux density in *Tesla*.

The alternating hysteresis loss occurs when the magnitude of the flux intensity in a magnetic material changes while the direction remains the same. It is caused by the effects of energy diminishing at remagnetization when the iron in the B-H curve traversing a complete cycle of the B-H curve. At remagnetization, the iron in the B-H curve travels along a hysteresis loop where the energy diminishes by the area enclosed in each loop.

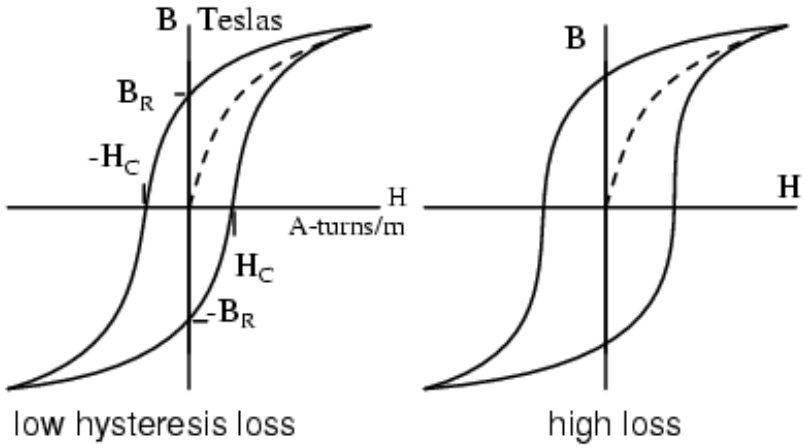

Figure 54 Alternating hysteresis loss in B-H curve

The loss for one rotor lamination stack is given by the formula from Steinmetz as presented by Knowlton (1949) as:

$$P_{ha} = \eta f_{eff} (10000 B_{\max})^{k} M_{vah} 10^{-1} (watts / m^{3}) \qquad (105)$$

Here, η is the hysteresis coefficient with a value of approximately 0.00046 for a good grade of silicon, and M_{vah} is the effective volume factor. For flux densities in the range

of 0.15~1.2 *Tesla*, the exponent k has an approximate value of 1.6. $B_{\max}$ and f_{eff} are the same as they are discussed in the eddy current loss.

Eddy currents are generated when the flux density within the iron core changes. A solid magnetic core acts like a short winding that generates large eddy currents. By dividing the iron core into insulated sheets or particles, the eddy currents can be reduced.

Assuming that the flux in the laminated sheets is sinusoidal and distributed evenly, the eddy current losses can be approximated by [24]:

$$P_e = \frac{\pi^2 d^2 B_{\max}^2 f_{eff}^2 M_{vec}}{6\rho} (watts/m^3) \tag{106}$$

Here, d is the lamination thickness in meter, ρ is the electric resistivity of the material in kg/m^3, f_{eff} is effective remagnetization frequency in H_z, which is 4 times of the rotational frequency for the 8-pole heteropolar magnetic bearing, and equal to the rotational frequency for the homopolar magnetic bearing. M_{vec} is the effective volume factor for eddy currents. For the heteropolar radial magnetic bearings, due to the alternating of the polarities in the poles, the flux direction in the rotor is also changing when it rotates, thus $B_{\max}$ is the maximum total flux intensity in *Tesla*. For the homopolar radial magnetic bearings, all the poles on the rotating plane of the rotor have the same polarity, so the varying flux intensity is only caused by the control flux. Thus for the homopolar magnetic bearings, $B_{\max}$ is the maximum control flux intensity. This results in the advantage of the homopolar magnetic bearing that the power loss is much lower than heteropolar magnetic bearings.

The hysteresis loss and the eddy current loss can be summed up as core loss and approximated from Carpenter's catalog [30], as shown on Figure 55.

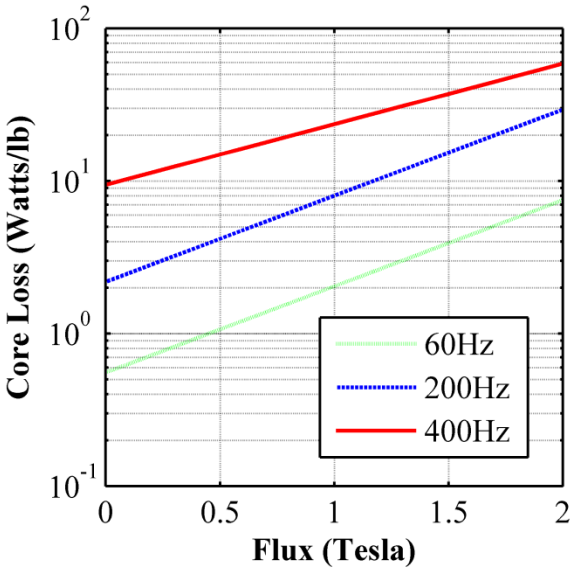

Figure 55 Extended core loss map from Carpenter's catalog

Windage losses are dominant in high speed machineries, for example in compressors and expanders where the gas is under high pressure. Basically, the air losses are proportional to the cube of the circumferential speed. Windage losses were calculated based on the drag force on a turbulent boundary layer as developed by Von Karman, which is approximated by:

$$P_{wd} = 0.074\pi\rho_g LR^4\omega^3\left(\frac{\nu}{2\pi R^2\omega}\right)^{0.2}(watts) \qquad (107)$$

Here, ρ_g is the air density in kg/m^3, ω is the shaft rotational frequency in rad/s, and υ is the viscosity of air in m^2/s, L is the length of the actuator, and R is the radius of the rotor at the bearing locations.

6.1.2 Power loss in the stator

The main losses in the actuator of the magnetic bearings system comes from the ohmic loss. The eddy current loss and alternating hysteresis loss exist in the stator. The total loss of the system is expressed by

$$P_{stator} = P_e + P_{ohmic} + P_{ha} \tag{108}$$

where P_{stator} is the total stator power loss, P_e is the eddy current loss, and P_{ha} is the alternating hysteresis loss. P_{ohmic} is the ohmic loss, which is caused by the current in the coils. The ohmic loss in each of the coil is in the form of

$$P_{ohmic} = \sum_{i=1}^{8} I_i^2 R_{coil} (watts) \tag{109}$$

where I_i is the maximum current in the coils for the i^{th} pole, and R_{coil} is the coil resistance of the pole.

The calculation of the eddy current loss and the alternating hysteresis loss is similar to the calculation in the rotor. The difference is that in the rotor, the flux intensity change is large with the flux direction change. However, in the stator, the direction of the flux intensity remains the same. The fluctuation of the flux intensity comes from the

variation of the control flux intensity. As a result, the hysteresis loss and the eddy current loss in the stator are generally very small and can be ignored.

As has been stated in part 2, homopolar magnetic bearings generally have lower power loss. In homopolar magnetic bearings, there are no changes in polarities in the rotational plane. As a result, there is no rotational hysteresis loss in the homopolar magnetic bearing supported rotor. Besides, the variation of the flux intensity is much smaller than they are in the heteropolar magnetic bearings, causing much lower rotational hysteresis loss and eddy current loss. In this research, in the heteropolar magnetic bearing supported system, the actuator and the rotor are laminated to reduce the eddy current loss.

6.2 AMB Actuator Thermal Analysis

The power loss components are used as heat sources in the thermal analysis of the actuator. The 2D finite element method (FEM) is used to determine the temperature distribution and find the hot spot temperature on the actuator. The 3D thermal modeling in Solidworks is used to validate the 2D thermal modeling.

6.2.1 Thermal analysis with 2D Finite Element Method

The 2D finite element method (FEM) is used to determine the temperature distribution of the actuator and detect the hot spot temperature on it. The calculation area of the actuator is selected based on the symmetry rule, assuming that all the currents in the 8 poles are the same, as is shown in Figure 56. As a result, half pole is chosen for

calculation. Four-node iso-parametric finite element method is used and the mesh for the 2D thermal analysis is shown in Figure 57. The Gauss quadrature formula is used for numerical integration.

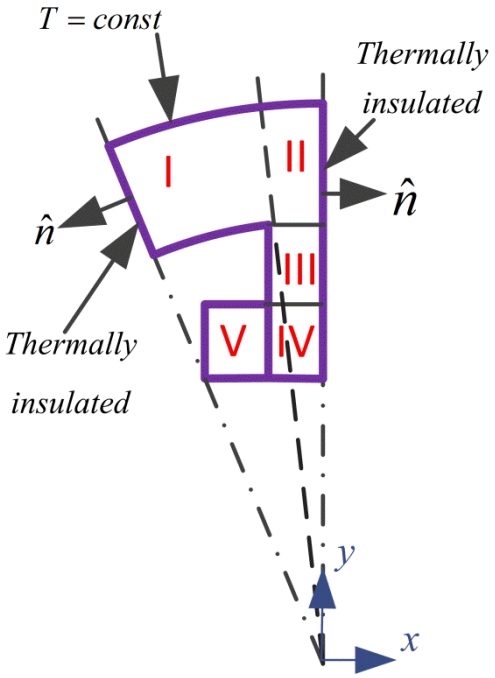

Figure 56 Calculation area of the actuator

On the right and left boundaries of the actuator, due to the symmetry, there is no heat flow across the two boundaries. On these two boundaries,

$$\hat{q}_l = 0 \tag{110}$$

In the actual applications, the outer surface of the stator is connected to the housing that dissipates heat efficiently. As a result, the upper boundaries are assumed constant room temperature, which is assumed to be 77°F (25°C). On this boundary,

$$T = const \tag{111}$$

The lower boundaries are forced convective boundary condition when the rotor is spinning. All the other boundaries are assumed free convection.

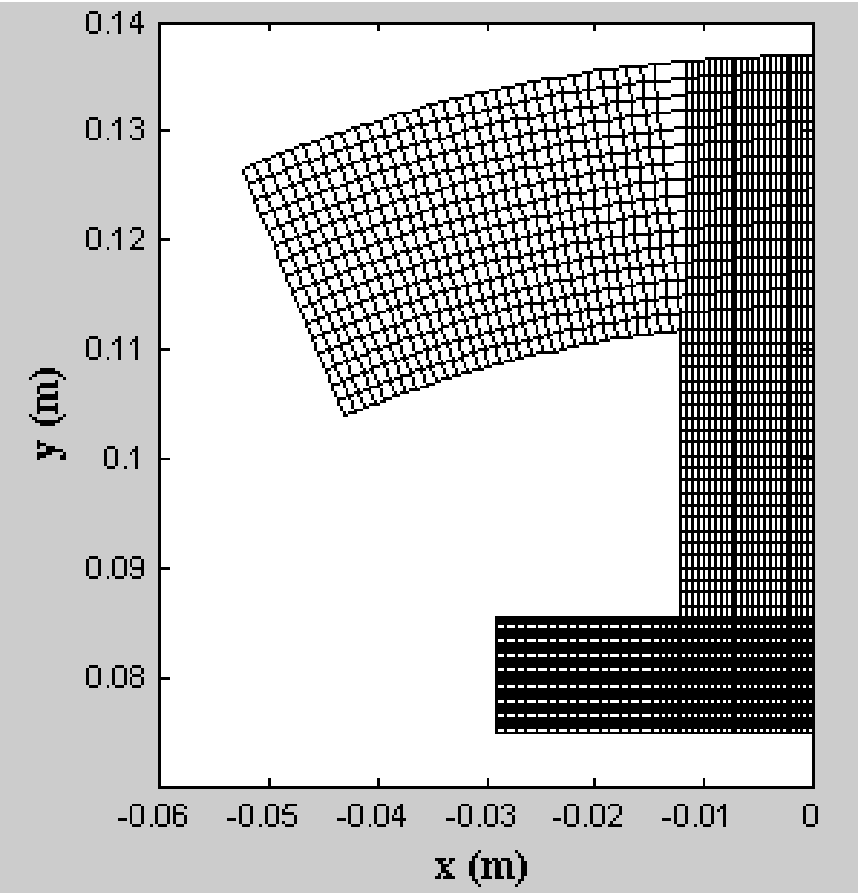

Figure 57 Mesh plot of the 2D FEM thermal analysis

In the stator (section I~ IV), the internal heat sources, which comes from the eddy current loss and alternating hysteresis loss, are assumed evenly distributed. In the coil (section V), the evenly distributed heat sources come from the ohmic loss.

6.2.2 Thermal analysis with 3D Solidworks modeling

The 3D thermal analysis is modeled with Solidworks. The power losses from the actuator are modeled as the heat sources. In this check case, assume that in each coil, there is 100 watts heat from iron power loss, which is about 5A current through 2 Ω resistance (half of the coil in 2D model). In the stator, assume there are 286.2 watts of the heat from core loss by Carpenter's catalog. On the inner surface of each pole, assume taht the windage loss is of 2 watts at 1300 rpm spin speed. The outer surface of the stator is assumed constant room temperature (77°F). All the other outer surfaces are considered as natural convection, with a convection coefficient of 7 $watts / m^2 / K$.

Figure 58 shows the temperature surface plot of the 2D thermal code, which shows a hot spot temperature of 147.8°F in the coil.

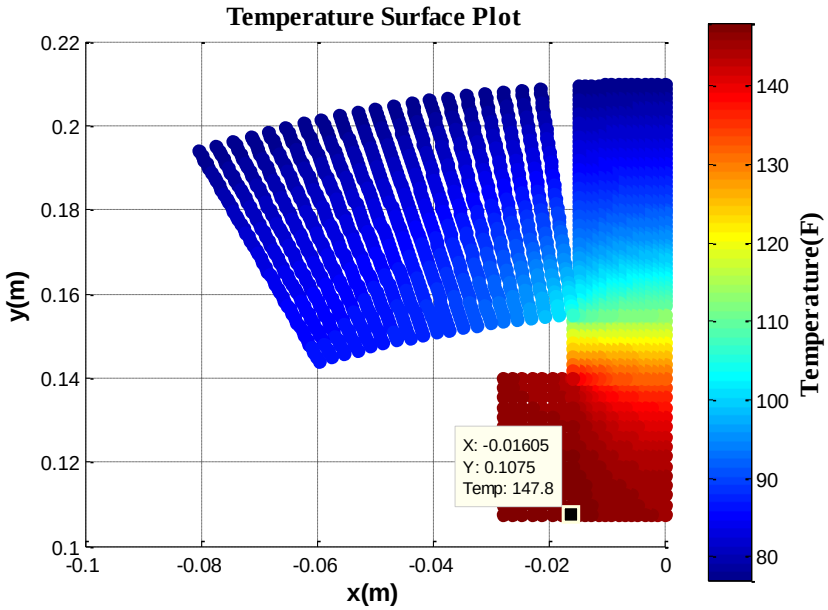

Figure 58 Temperature surface plot of the 2D modeling with TRC code

Figure 59 shows the mesh plot of the heteropolar 8-pole magnetic bearing core actuator model with 3D Solidworks thermal model.

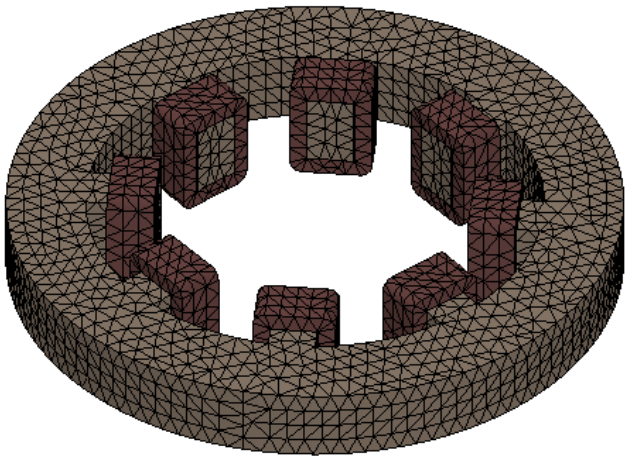

Figure 59 Mesh plot of the 3D thermal modeling with Solidworks

Figure 60 shows the temperature surface plot of the actuator in the 3D thermal modeling, which shows a hot spot temperature of 150°F in the coil. Comparison between Figure 58 and Figure 60 shows that temperature distribution in the actuator and the predicted hot spot temperature by the 2D FEM thermal modeling code are very close to they are in the 3D Solidworks model. The 2D FEM thermal modeling, which takes only 1/16 of the actuator and assumes that all heat flows in the radial direction, is proved to be a reliable and much less computationally expensive way to predict the temperature distribution and the hot spot temperature in the actuator. The hot spot temperature will be later used as a constraint in one of the optimization example. In the searching and iteration, this type of simplified yet accurate model saves computation cost significantly.

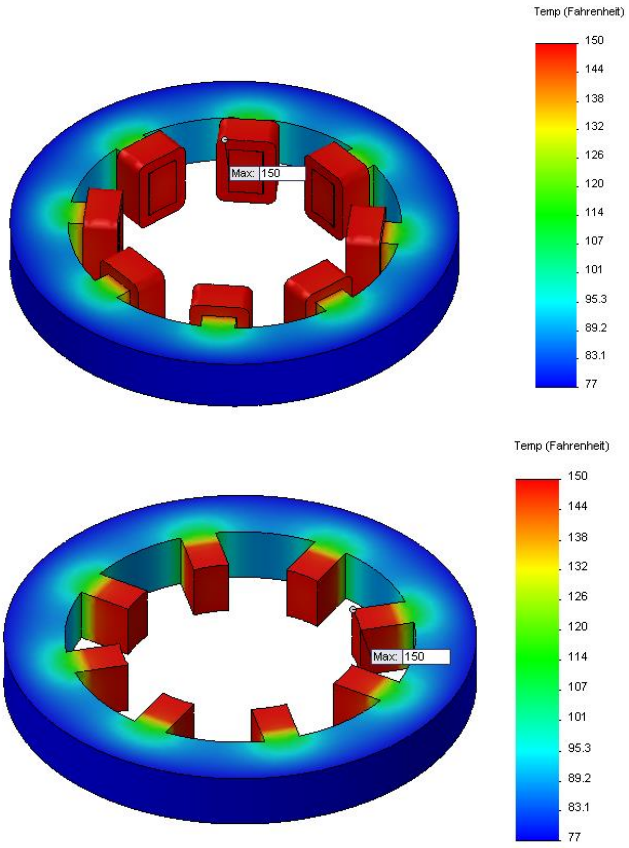

Figure 60 Temperature surface plot of the 3D thermal modeling with Solidworks

6.2.3 Thermal test with a 6 pole homopolar magnetic bearing actuator

A thermal test is conducted on a stationery 6-pole homopolar magnetic bearing actuator. Figure 61 shows the devices used in the test, including the amplifier, 6-pole magnetic bearing actuator, current probe and the thermal couple. The thermal couple was used to detect and measure the highest temperature on the stator and coil corresponding to different coil current values. In this case, the stator is stationery and there is no spinning rotor, thus the only power loss or the heat source in the stator comes

from the ohmic loss in the coils. There is no eddy current loss or the hysteresis loss in the stator.

Coil resistance in each of the pole is 0.126 Ω by test result. The hot spot was detected and measured by increasing the current from 1A to 5A. The convective coefficient was estimated to be h=7.5 $W / m^2 / K$. In this test, the outer surface of the stator is free convection boundary, which is different from the constant temperature boundary in the 8-pole case where the stator is connected with the housing.

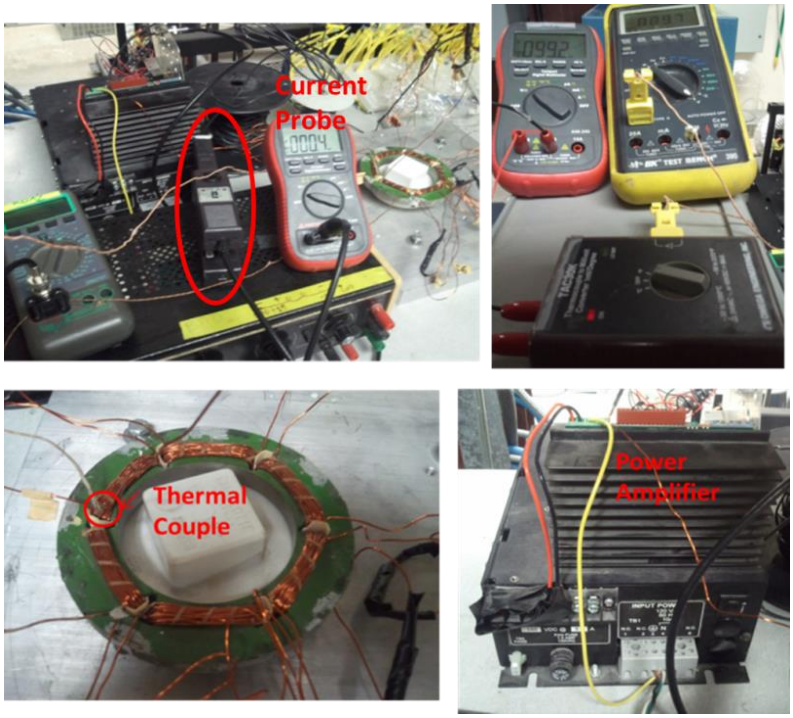

Figure 61 Thermal test experimental setup

The main uncertainty in the test comes from the convective coefficient at the free convective boundary. The value is dependent on the type of media, gas or liquid, the

flow properties such as velocity, viscosity and other flow and temperature dependent properties. In general the free convective heat transfer coefficient for air indoors varies from 5 ~ 25 $W / m^2 / K$. In this simulation, the free convective boundaries are approximated as vertical plate with laminar flow, and using Rayleigh number [8] to determine the convective heat transfer coefficient. The Rayleigh number is

$$Ra_L = \frac{g\beta(T_s - T_\infty)L^3}{\alpha\nu} \tag{112}$$

The correlations recommended by Churchill and Chu [9] is of the form

$$Nu_L = \left\{ 0.825 + \frac{0.387\ Ra_L^{1/6}}{[1+(0.492/\mathrm{Pr})^{9/16}]^{8/27}} \right\}^2 \tag{113}$$

The convective heat transfer coefficient for free convection is

$$h = \frac{Nu_L \cdot k}{L} \tag{114}$$

Here, g is the gravity acceleration, T_s is the surface temperature, T_∞ is the room temperature, L is the characteristic length of the surface, which is the thickness of the actuator in this case. ν is the kinematic viscosity, α is the thermal diffusivity, and β is the thermal expansion coefficient, P_r is the Prandtl number.

The resulting convective heat transfer coefficients for free convection are 6 ~ $10 W / m^2 / K$ when the surface temperature is between 82°F and 200°F, which is the temperature range of the convective boundaries. In this simulation, free convection coefficient is assumed to be 7.5 $W / m^2 / K$ and the result is compared with the test, as is shown in Figure 62.

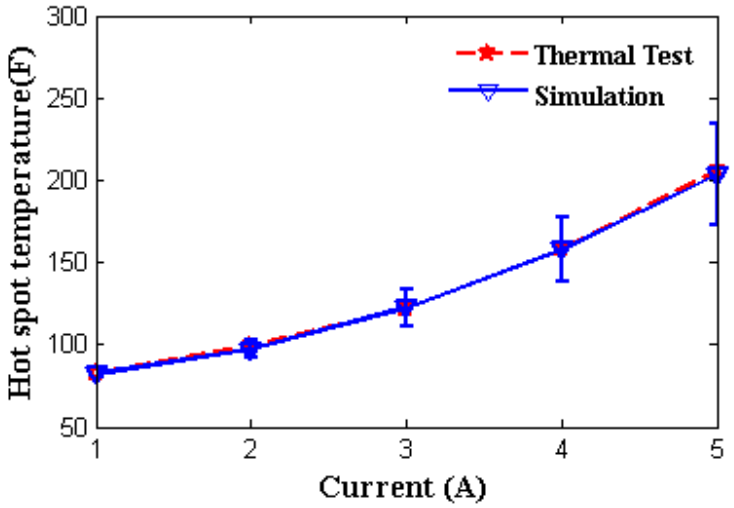

Figure 62 Code result V.S. test result with error bar induced by uncertainty of the convective coefficient

The results show that when the free convection coefficient is $7.5 W / m^2 / K$, the test and the simulation give almost identical hot spot temperatures, which means the 2D FEM thermal analysis results are consistent with the test.

Figure 62 also shows the error bar induced by the uncertainty of the convective heat transfer coefficient. Points below the line indicate an upper limit of the free convection coefficient value of $10 W / m^2 / K$, while points above the line indicate a lower limit of the free convection coefficient value of $6 W / m^2 / K$. The error induced by the uncertainty of the free convection coefficient is significant at high temperatures.

7. ISO STANDARD CHECK OF AMB SUPPORTED SYSTEM

The ISO 14839 standards were developed specifically for rotating machinery equipped with active magnetic bearings. For conventional oil-film bearings, API 617 [31] regarding centrifugal compressors is usually applied. However, these standards set a peak-to-peak displacement criterion that is too strict for magnetic bearings. Besides, due to the control unit in the active magnetic bearings supported rotor-bearing system, the stability of the system should be evaluated with the electronic components, including the controller, sensor, power amplifier and compensators. The ISO 14839 [1, 32]standards are specially designed for magnetic bearing supported turbomachinery systems, which requires that the rotating machinery equipped with active magnetic bearings should be evaluated:

- shaft vibratory displacement measured at or close to the AMBS, and
- working current and voltage measured in magnetic coils or power supply amplifiers, and
- stability margin of the closed loop system

In this study, a power amplifier model with both current and voltage limit is developed. The current and voltage output can be plotted in the transient simulations. So the main standard check focuses on the vibratory displacement and the stability margin. To note that in the eight edition of API617, a new annex presents an extensive set of specifications that AMB supported compressors and expanders must meet for API service. For the vibration amplitude and sensitivity margin check, the API617 follows the ISO14839.

7.1 ISO 14839-2: Evaluation of Vibration

Reliable operation of the AMB machines requires that the maximum rotor displacement lower than the minimum radial clearance (minimum axial clearance for axial bearing) to avoid contact between rotating and stationary parts of a machine. Due to the larger clearance, magnetic bearings allow larger vibration amplitude than conventional bearings. The standards for oil-film bearings can be relaxed for the magnetic bearings. The ISO 14839-2 sets limits for the maximum displacement of the rotor.

The catcher bearing clearance is generally set to be the minimum clearance. The following figure shows the maximum rotor displacement of a radial magnetic bearing $D_{\max}$, where ε_x and ε_y are the rotor eccentricities in *x*, *y* directions, $2a_x$ and $2a_y$ are the vibration amplitude in *x*, *y* directions.

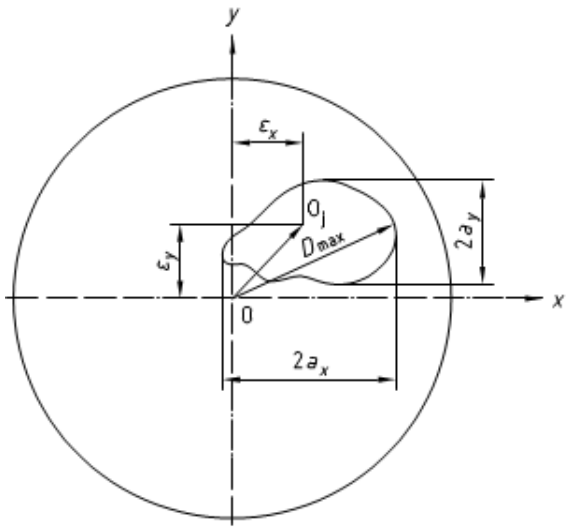

Figure 63 Maximum rotor displacement

ISO 14839 establishes vibration zone guidelines for magnetic bearings. The definitions of each zone are as follows.

Zone A: The vibratory displacement of newly commissioned machines would normally fall within this zone.

Zone B: Machines with vibratory displacement within this zone are normally considered acceptable for unrestricted long-term operation.

Zone C: Machines with vibratory displacement within this zone are normally considered unsatisfactory for long term continuous operation. Generally, the machine may be operated for a limited period in this condition until a suitable opportunity arises for remedial action.

Zone D: Vibratory displacement within this zone is normally considered to be sufficiently severe to cause damage to the machine.

In this study, the maximum vibratory displacement is measured in the transient analysis, with rotor induced unbalance and other external static force applied on the rotor.

7.2 ISO 14839-3: Evaluation of Stability Margin

ISO 14839 introduced a new approach to evaluate the stability margin of the AMB system. The approach is related to the gain margin. The peak magnitude value of the closed-loop sensitivity function is inversely proportional to the system gain margin. Therefore, a smaller sensitivity function peak corresponds to a larger system gain margin, which indicates a larger stability margin.

7.2.1 Sensitivity function measurement

The perturbation and measurement points specified in the ISO 14839-3 standard for obtaining the sensitivity function is shown in Figure 64, which can be simplified as a block diagram as shown in Figure 65. According to the ISO14839-3, the open-loop transfer function or the system's sensitivity function is measured at rotor standstill and/or nominal speed but over the maximum frequency range starting from zero.

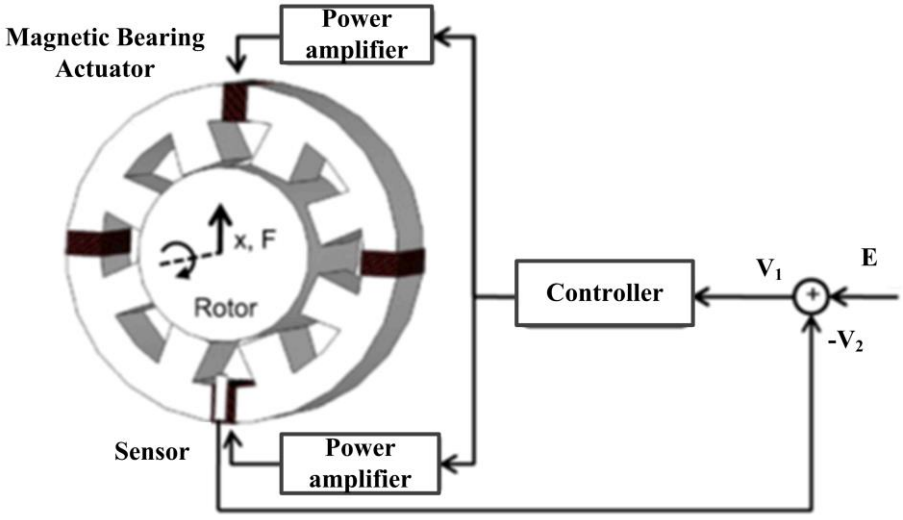

Figure 64 Excitation and measure point for sensitivity function

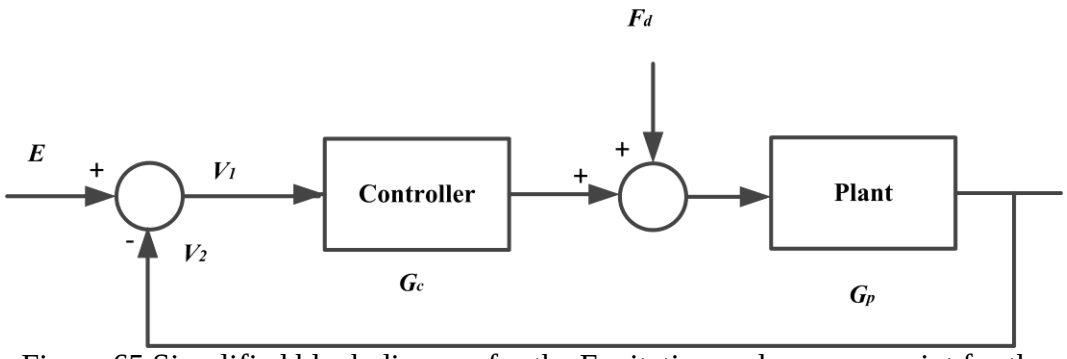

Figure 65 Simplified block diagram for the Excitation and measure point for the sensitivity function

In Figure 64 and Figure 65, a point between the sensor and controller was selected to injection an excitation $E(s)$. The response signals V_1 and V_2, after and before the injection point respectively, are measured. At this injection point,

$$V_1(s) = E(s) - V_2(s) \tag{115}$$

And the open loop transfer function of the closed loop system is

$$G_o = \frac{V_2(s)}{V_1(s)} \tag{116}$$

Thus, the sensitivity transfer function is

$$G_s = \frac{1}{1+G_0} = \frac{V_1}{V_1+V_2} = \frac{V_1(s)}{E(s)} \tag{117}$$

Similar to the ISO 14839-2, four zones are defined in ISO 14839-3 to describe the stability of the AMB system.

Table 4 given by ISO 14839 summarizes the zones for vibration displacement and sensitivity. According to the table, for new machines supported on magnetic bearings, the maximum displacement should be less than 0.3 of the catcher bearing clearance, and the peak sensitivity should be less than 3 (9.5 dB). To be accepted for long term operation, it is required that the magnetic bearing supported machines have a maximum displacement between 0.3 ~ 0.4 of the catcher bearing clearance, and a maximum sensitivity bound between 3 ~ 4 (9.5 ~ 12 dB). If the maximum displacement is between 0.4 ~ 0.5 of the catcher bearing clearance, or a maximum sensitivity bound is between 4 ~ 5 (9.5 ~ 12 dB), the magnetic bearing supported machines are expected to have excessively high vibration. If the maximum displacement is larger than 0.5 of the

catcher bearing clearance, or a maximum sensitivity bound is larger than 5 (12 dB), then the magnetic bearing supported machines are expected to be damaged by excess vibration.

Table 4 Zones and respective boundaries from both ISO 14839-2 and ISO 14839-3

Zone	Max. displacement bounds	Peak sensitivity G(jω) bounds	Description
A	$D_{max} < 0.3C_{min}$	$G(j\omega) < 3$ (9.5dB)	New machines
B	$0.3C_{min} < D_{max} < 0.4C_{min}$	$3(9.5dB) < G(j\omega) < 4$ (12dB)	Acceptable for long term operation
C	$0.4C_{min} < D_{max} < 0.5C_{min}$	$4(12dB) < G(j\omega) < 5$ (14dB)	Excessively high vibration
D	$D_{max} > 0.5C_{min}$	$G(j\omega) > 5$ (14dB)	Machine damage expected

7.2.2 Sensitivity function by simulation

As shown in Figure 65, the open loop transfer function of the system can be described as

$$G_0(s) = G_c(s) \cdot G_p(s) \tag{118}$$

Here $G_c(s)$ is the transfer function of the controller, including lead and/or lag compensators, notch filters, and any other additional filters. $G_p(s)$ is the transfer function of the plant, including the system components of sensor, amplifier, and actuator, as shown in Figure 66. So the open loop transfer function is in the form of

$$G_0(s) = G_c(s) \cdot G_{PA}(s) \cdot G_{act}(s) \cdot G_{rot}(s) \cdot G_{sen}(s) \tag{119}$$

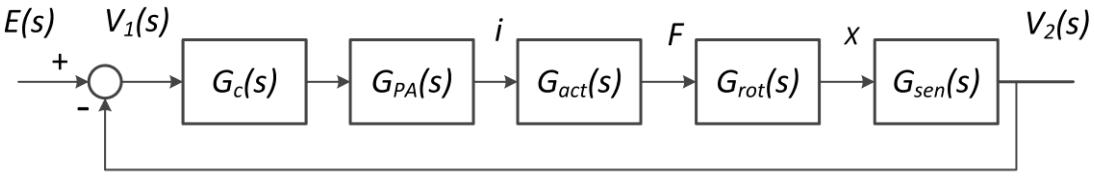

Figure 66 Block diagram for excitation and measure point for sensitivity function

The transfer function of the controller, power amplifier, and sensor can be defined easily. The actuator transfer function can be defined as the 2nd order filter with a DC gain that is equivalent to the current stiffness in that direction.

The rotor transfer function can be defined by the ratio of the displacement at the sensor to the magnetic force generated in the corresponding actuator.

The equation of motion of the AMB supported system can be described by:

$$\underline{M}\ddot{\underline{X}} + \underline{C}\dot{\underline{X}} + \underline{K}\underline{X} = \underline{F} \tag{120}$$

The position stiffness of the magnetic bearing is included in the $\underline{K}$. Substitute $\underline{X} = \tilde{\underline{X}}e^{j\omega t}$ and $\underline{F} = \tilde{\underline{F}}e^{j\omega t}$ into the equation of motion and

$$(-\omega^2\underline{M} + j\omega\underline{C} + \underline{K})\tilde{\underline{X}} = \tilde{\underline{F}} \tag{121}$$

$$\tilde{\underline{X}} = (-\omega^2\underline{M} + j\omega\underline{C} + \underline{K})^{-1}\tilde{\underline{F}} \tag{122}$$

Let $R(\omega) = (-\omega^2\underline{M} + j\omega\underline{C} + \underline{K})^{-1}$, then

$$\tilde{\underline{X}}_j = R_{jk}(\omega)\tilde{\underline{F}}_k \tag{123}$$

The transfer function of the rotor, which describes the magnitude and phase angle between the rotor displacement at the sensor location ($\tilde{\underline{X}}_j$) and the corresponding magnetic force generated by the actuator ($\tilde{\underline{F}}_k$), is

$$G_{rot}(j\omega) = \frac{\tilde{\underline{X}}_j}{\tilde{\underline{F}}_k} = R_{jk}(\omega) \tag{124}$$

Finally, the open loop transfer function can be written in the function of the sweep frequency ω

$$G_o = G_c(s = j\omega) \cdot G_{PA}(s = j\omega) \cdot G_{act}(s = j\omega) \cdot G_{rot} \cdot G_{sen}(s = j\omega) \tag{125}$$

Then by $G_s = \frac{1}{1 + G_o}$, the sensitivity function can be obtained as

$$G_s = \frac{1}{1 + G_c(s = j\omega) \cdot G_{PA}(s = j\omega) \cdot G_{act}(s = j\omega) \cdot G_{rot} \cdot G_{sen}(s = j\omega)} \tag{126}$$

Now the stability margin of the system can be obtained by evaluating the magnitude of this frequency dependent sensitivity function.

7.3 Example of ISO Standard Check

The example of the ISO standard check is based on the linear case in part 4. The exemplary plot of the transient analysis with rotor unbalance, with same setups as in 4.2, is as presented in Figure 67. The catcher bearing clearance is 0.25mm, and the maximum displacement is 0.096mm, which is 0.39 of the catcher bearing clearance. The vibratory displacement falls into the zone B in the ISO standard, which is acceptable for long-term use of the magnetic bearing supported system. As shown in the plots, the maximum magnitude of sensitivity function in the z direction is smaller than 3, which indicates that the system in the z direction satisfy the zone A stability requirements, which is for new machines.

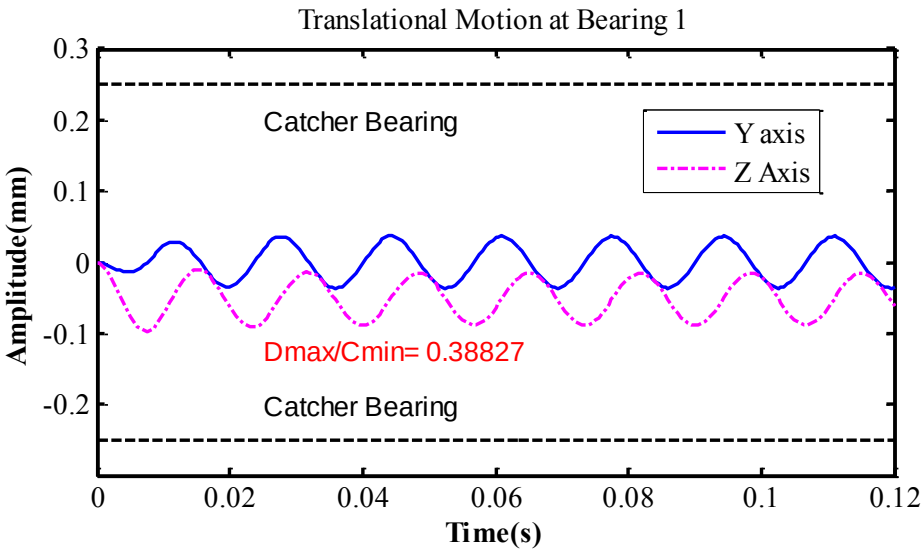

Figure 67 Unbalance transient analysis for ISO standard check

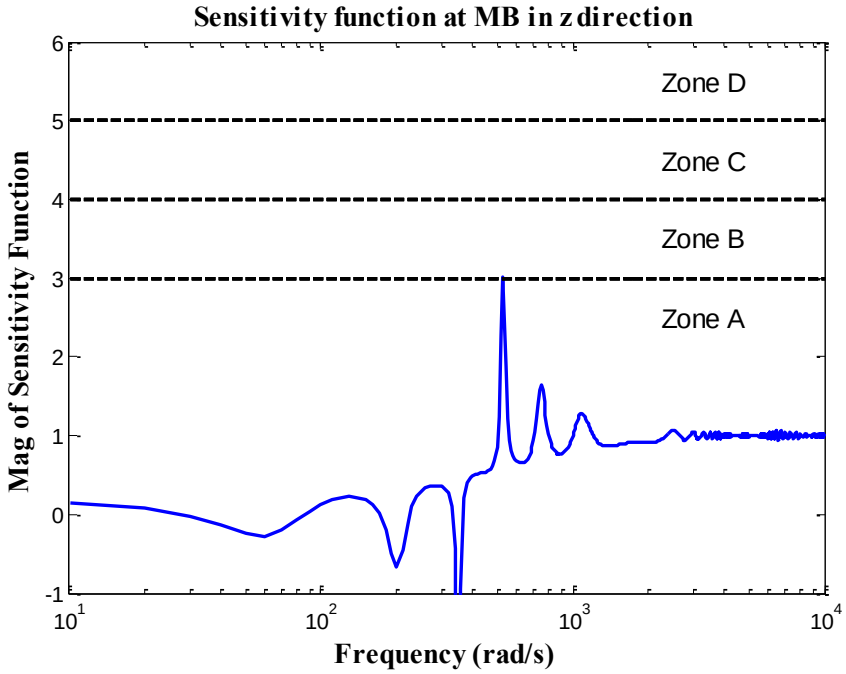

Figure 68 Exemplary sensitivity function magnitude plots

8. HOMOPOLAR AMB OPTIMIZATION DESIGN EXAMPLE*

In this section, an optimization design example based on homopolar magnetic bearing actuator supported rotordynamic system is presented. Homopolar magnetic bearings, which have much lower power loss and higher energy efficiency, have been widely used especially in the satellites. However, the more wide spread use of the homopolar magnetic bearings is limited by their complicated structure. This section presents an example design of the homopolar magnetic, which can optimize the actuator and the controller parameters simultaneously, to achieve a design with the minimum actuator mass, the minimum vibration amplitude at steady state operation, and the minimum power loss.

8.1 Homopolar AMB Optimization Problem Statement

In this study, the actuator mass, the steady state vibration amplitude, and the power loss are evaluated and set as three minimization type objectives. The objectives, design variables, and constraints are illustrated in this part.

8.1.1 Objectives

One of the main concerns in the designing of the homopolar magnetic bearings is

* Copyright [2015] by ASME: Part of the data reported in this section is reprinted with permission from Zhong, W., and Palazzolo, A., 2015, "Magnetic Bearing Rotordynamic System Optimization Using Multi-Objective Genetic Algorithms," Journal of Dynamic Systems, Measurement, and Control, 137(2), p. 021012.

to reduce the actuator mass, especially in the application of air space area. As a result, minimizing the total actuator mass is set as the first optimization goal. The total actuator mass includes the mass of the stator, mass of the coil, mass of the permanent magnet, and mass of the back iron. The actuator mass can be expressed as

$$W_{Total} = W_s + W_{coil} + W_{pm} + W_{bi} \tag{127}$$

where W_s is the mass of the stator, W_{coil} is the mass of the coil, W_{pm} is the mass of the permanent magnet, and W_{bi} is the mass of the back iron and

$$W_s = \rho_s V_s \tag{128}$$

$$V_s = \pi\left(r_s^2 - r_c^2\right) l_p + 4A_p(r_c - r_p) \tag{129}$$

where r_s is the outer diameter of the stator, l_p is the length of pole along the rotor axis, A_p is the cross sectional area of the pole.

The weight of the coil is

$$W_{coil} = 4\eta\rho_c V_c \tag{130}$$

where V_c is the volume of the coil and η is the coil packing factor

$$\begin{aligned} V_c &= ((w_p + 2t_c)(l_p + 2t_c) - w_p l_p) l_c \\ &= 2t_c l_c (w_p + 2t_c + l_p) \end{aligned} \tag{131}$$

and $A_c = t_c l_c = N\eta\pi(d_w / 2)^2$, so $l_c = N\eta\pi(d_w / 2)^2 / t_c$.

The weight of the permanent magnet is

$$W_{pm} = 8\rho_{pm} A_m L_m \tag{132}$$

where ρ_{pm} is the mass density of the permanent magnet, A_m is the cross sectional area of the permanent magnet and L_m is the length of the permanent magnet.

The weight of the back iron is:

$$W_{bi} = \rho_{bi} L_r ((r_s + t_{bi})^2 - r_s^2) \tag{133}$$

where ρ_{bi} is the mass density of the back iron.

The steady state vibration amplitude from unbalance response indicates the rotor sensitivity and the effectiveness of the bearing damping, thus is selected as the second objective of optimization design. Steady state vibration amplitude is obtained from the unbalance transient analysis. In this study, the rotor unbalance is defined at node 11, which is the center of the rotor that excites the first mode most, with a phase angle of 90°.

The main losses in the homopolar magnetic bearings system include: eddy current loss, windage loss, ohmic loss, and hysteresis loss. [29] The total loss of the system is expressed by:

$$P_{Total} = P_{wd} + P_{ohmic} + P_{core} \tag{134}$$

where P_{Total} is the total system power loss and P_{ohmic} is the core loss of the actuator consisting of eddy current loss and hysteresis loss.

The calculation of the windage loss has been stated in part 3.4. The ohmic loss is in the form of

$$P_{ohmic} = n_p I_{\max}{}^2 R_{coil} (watts) \tag{135}$$

where $I_{\max}$ is the maximum current in the coil and R_{coil} *i*s the total resistance of the coil.

$$R_{coil} = \rho_{cu} N l_{coil} / A_w = 4\rho_{cu} N l_{coil} / (\pi d_w{}^2) \quad (136)$$

where l_{coil} is the average length of the coil per turn, which is the circumferential length of the blue center line in Figure 4 (b). The equation for the average length of the coil per turn is written as:

$$l_{coil} = 2(l_p + w_p + 2t_c) \quad (137)$$

The eddy current loss and hysteresis loss can be calculated according to the equations in chapter 3. In this case study, the eddy current loss and hysteresis loss are summed up as core loss and approximated from Carpenter's catalog [30], as shown on Figure 69.

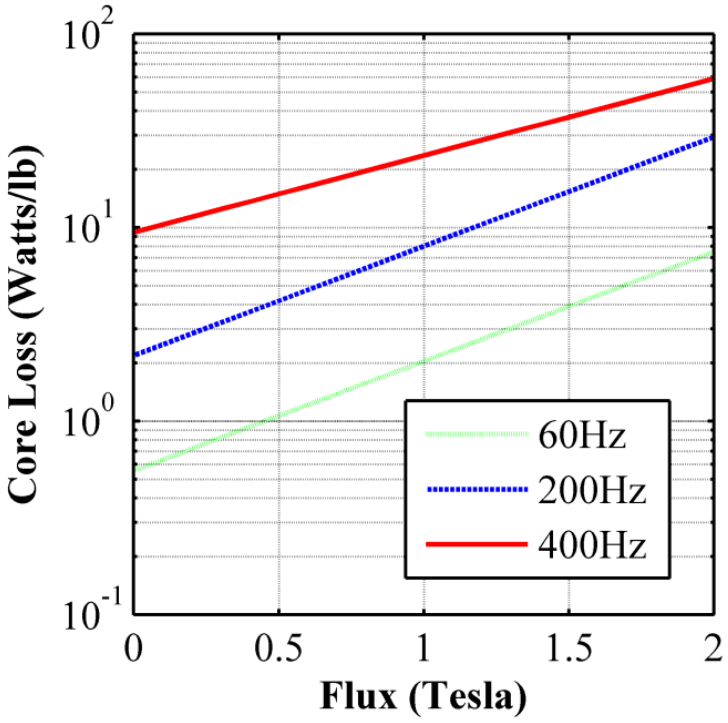

Figure 69 Extended core loss map from Carpenter's catalog

8.1.2 Design variables

To achieve the design objectives, 10 design variables, including 8 parameters describing the actuator geometry, and 2 parameters defining the gains of the PD controller, are selected. The design variables and their boundaries are listed in Table 5.

Table 5 Design variables and bounds for homopolar AMB optimization example

Design Variable	Design Variable	Lower Bound	Upper Bound
1	pole length along rotor axis, $l_p(m)$	0.01	0.08
2	air gap clearance, $l_g(m)$	0.0003	0.0012
3	permanent magnet thickness, $t_m(m)$	0.005	0.03
4	permanent magnet length, $L_m(m)$	0.008	0.08
5	air gap area, $A_g(m^2)$	0.0001	0.005
6	permanent magnet area, $A_m(m^2)$	0.0001	0.01
7	coil turns, N	30	200
8	stator inner radius, $r_c(m)$	0.055	0.25
9	proportional gain, G_p	5	80
10	derivative gain, G_d	0.005	1

8.1.3 Constraints

The optimization constraints come from the physical configuration, stability of the rotordynamic system, power amplifier limits, material properties, etc. In this MOGAs optimization of HOMB supported rotordynamic system, 11 constraints were applied in the NSGA-II code:

1. The closed loop controlled system should be stable, with all eigenvalues of the characteristic matrix A_{sys} in the left half plane, which can be written as

$$(real(\lambda))_{max} \le 0 \tag{138}$$

where λ is the eigenvalue of the closed loop system characteristic matrix A_{sys}, $real(\lambda)$ is the real parts of the eigenvalues, and $(real(\lambda))_{max}$ represents its maximum value.

2. The power amplifier current is limited by its saturation value and can be expressed by

$$i_{\max} \le i_{sat} \tag{139}$$

where $i_{\max}$ is the maximum power amplifier current in the levitation simulation and unbalance analysis, which is extracted from the transient analysis.

3. The power amplifier voltage in the unbalance analysis and levitation simulation is limited by the saturation voltage of the power amplifier.

$$V_{pmax} \le V_{psat} \tag{140}$$

where V_{pmax} is the maximum power amplifier voltage in the levitation simulation and unbalance analysis, which is extracted from the transient analysis.

4. The flux density is limited to the saturation flux density of the actuator material,

$$B_{\max} \le B_{sat} \tag{141}$$

where B_{sat} is the saturation flux intensity and $B_{\max}$ is the maximum flux intensity. The maximum flux density $B_{\max}$ is obtained through solving the circuit equation with the control current and the respective rotor displacement when the control current is the maximum throughout the levitation and rotor unbalance analyses, i.e.

$$i_{cy} = i_{cz} = i_{\max} \tag{142}$$

$$y = y_{i_c = i_{max}}, z = z_{i_c = i_{max}} \tag{143}$$

5. The space of the total actuator is limited in the radial direction by the maximum outer diameter of the back iron.

$$D_{BI} \le D_{\max} \tag{144}$$

where $D_{BI} = 2(r_s + t_{bi} + t_m)$ and $D_{\max}$ is the maximum outer diameter of the back iron defined.

6. The length of the coil bulk is limited by the stator and can be expressed as

$$l_c \le (l_c)_{\max} \tag{145}$$

where $(l_c)_{\max} = \sqrt{r_c^2 - (t_c + w_p / 2)^2} - r_p$.

7. Width of the coil bulk is defined 5 times bigger than the diameter of the coi,

$$t_c \ge 5 d_w \tag{146}$$

where d_w is the diameter of the coil, and t_c is the width of the coil bulk. For this 4-poles case,

$$t_c = r_p \tan 45^\circ - w_p / 2 \tag{147}$$

8. The space of the permanent magnet is limited. The area of the permanent magnet can be expressed by

$$A_m = \theta(r_s^2 - (r_s - t_m)^2) / 2 \tag{148}$$

where θ is the angle of arc of the permanent magnet, and is limited by

$$\theta \le 2\pi / n_p \tag{149}$$

where n_p is the number of poles on each stator, and $n_p = 4$ in this case.

9. According to the API 617 [31], the maximum amplification factor(AF) is defined less than 5.

$$(AF_i)_{\max} < 5 \tag{150}$$

The amplification factor is directly related to the damping ratio of the closed loop system in the form of $AF_i = \frac{1}{2\xi_i}$, where ξ_i is the damping ratio of the system defined by the eigenvalues in the form of $\xi_i = -\frac{real(\lambda_i)}{|\lambda_i|}$, i=1,2,3,…, 332. This amplification factor constraint is to ensure that the closed loop controlled system should be able to supply sufficient damping.

10. The actuator length is limited by L_{rmax}, which is the maximum actuator length defined

$$L_r < L_{rmax} \tag{151}$$

The flowchart of the code is shown in Figure 70. As can be seen from the flowchart, the good design should be able to: 1) stabilize the rotor system; 2) levitate the rotor from the initial position; 3) minimize the three objectives including the actuator mass, the steady state vibration amplitude, and the power losses simultaneously.

In the standard NSGA-II, all the constraints are treated independently and equally, which from the first generation, for each population in each generation, all the analysis, including eigenvalue analysis, time transient response analysis, and power loss analysis, etc. are required. In this study, to speed up the optimization, the optimization first checks the physical confliction constraints. For example, the 6th

constraint listed above, that the length of the coil bulk is limited by the stator, is expressed by a simple equation and can be checked quickly at very low computation cost. If there are physical conflictions of the actuator parameters, it will be unnecessary to do eigenvalue analysis, time transient response analysis, and power loss analysis, etc. In such cases, all the following eigenvalue analysis, transient analysis, power loss analysis, etc. are skipped. Extremely "poor" objective values and constraint values are assigned to these design variables so that the optimization would filter out these designs quickly. With similar strategy, the eigenvalues are then checked for system stability of the system without physical conflictions. Time transient levitation simulation are only conducted for the stable system without physical conflictions to check if the system has enough dynamic load capacity to lift the rotor from an initial position. For the system with enough dynamic load capacity, an unbalance transient simulation is then conducted. The power loss is determined for the steady state operation in the unbalance transient analysis to work as one of the optimization objectives. Since the initial generation is randomly created, most of the populations in the early generations might physical conflictions. No eigenvalues analysis, transient analysis, or power loss analysis are required for them. For the early generations, the computation can be very fast with the strategy. As the optimization continues, the populations get better with less physical conflictions. The eigenvalues analysis, transient analysis, and power loss analysis are more frequently required and the optimization slows down.

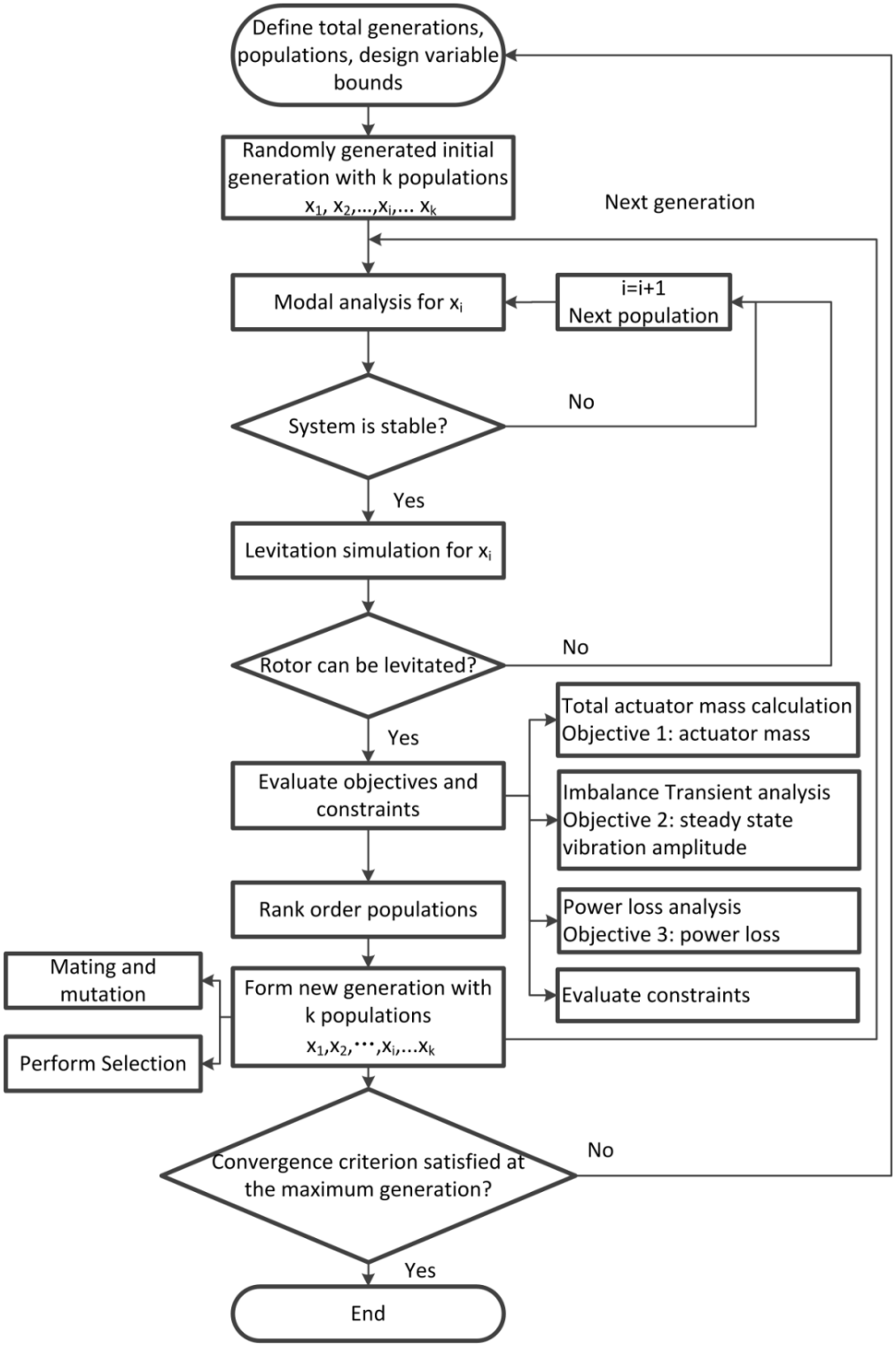

Figure 70 Flowchart of multiple objective optimization of HOMB system with NSGA-II code

8.2 Rotordynamic System Assembling

The optimization is based on the FEM flexible rotor model with 6 degree of freedom Timoshenko beam element. In this example, there are 23 nodes of the rotor, resulting in 138 states in *U*. Simulations verified that 23 nodes yielded converged natural frequencies and responses. The blue circles on the rotor indicate the nodes for the magnetic bearings and their respective sensors. The bearings are located symmetrically with respect to the mid cross section of the rotor (Node 11). The controllers, power amplifiers, sensors, filters and compensators of the closed loop controlled system are represented by the transfer function forms, and then converted into state space representation forms to assemble into motion of equation of the rotor. The total system can be summarized as a first order ordinary differential equation with 332 dimensions, which is in the form of

$$W_{sys} = [\underbrace{\dot{U}^T U^T}_{1\times 276} W_{sen}\ W_{con}\ W_{pa}\ W_{act}\ W_{filter}]^T \qquad (152)$$

where W_{sen} includes the state variables of the sensors, which are modeled as a DC gain with a first order filter. W_{con} includes the state variables of the PD controllers. W_{pa} includes the state variables of the power amplifiers modeled as a DC gain with a 1st order filter with an output current and voltage limit in the linear range. W_{act} includes the state variables of the actuator with 2nd order filters. W_{filter} includes the state variables of the additional low pass filters (5X4), lead compensators (1X4) and lag compensators (1X4).

The sensor used in the system is modeled as a DC gain of 1181V/m with a 1st order filter of high bandwidth (cut-off frequency set to be 15.9 kHz). The resulting transfer function of the sensor is

$$TF_{sen}(s) = \frac{1181}{1e-5s+1} \tag{153}$$

The power amplifier is modeled as a DC gain of 1A/V with a 1st order filter of 100 Hz cut-off frequency and is limit to output current and voltage saturation. In the linear range while the output current and voltage are less than the limits, the transfer function of the power amplifiers is

$$TF_{pa}(s) = \frac{12.5664}{0.02s+12.5664} \tag{154}$$

The transfer function of the PD controller is written as

$$TF_{con}(s) = \frac{G_p + G_d s}{(\tau_p s+1)(\tau_d s+1)^2} \tag{155}$$

where the proportional gain and derivative gain, G_p and G_D are two of the design variables to be optimized, τ_p and τ_d are the time constants of the proportional gain and derivative gain respectively. τ_p and τ_d are both set to be small as 1e-5 to ensure high bandwidth of the PD controller. Other system constant parameters are listed in Table 6. The maximum flux intensity is limited to 2 Tesla, the saturation voltage of the power amplifier is set to be 220 V, and the saturation current of the power amplifier is set to be 15Amps.

Table 6 Constants and input parameters for homopolar AMB optimization example

Symbol	Quantity	Value
μ_0	free air permeability	$4\pi\times10^{-7} H/m$
μ_{pm}	permeability of permanent magnet	$1.35\times10^{-6} H/m$
B_{sat}	saturated flux density	$2.0\,Tesla$
η	coil packing factor	0.85
d_w	wire diameter	$0.00129\,m$
ρ_r	weight density of rotor	$7850\,kg/m^3$
ρ_s	weight density of stator	$7770\,kg/m^3$
ρ_c	weight density of coil	$8910\,kg/m^3$
ρ_{bi}	back iron weight density	$7850\,kg/m^3$
ρ_{pm}	permanent magnet density	$7400\,kg/m^3$
ρ_{air}	air density	$1.2\,kg/m^3$
t_{bi}	back iron thickness	$0.01\,m$
υ_{air}	air viscosity	$1.501\times10^{-5} m^2/s$
ρ_{cu}	resistivity of copper	$1.68\times10^{-8}\Omega\cdot m$
H_c	permanent magnet coercive field intensity	$633000\,A/m$
r_s/r_c	ratio of stator outer diameter to coil radius	1.1
$D_{\max}$	maximum back iron outer diameter	$0.4\,m$
M_s	volume ratio of the flux path in the stator	0.4
M_r	volume ratio of flux path in the rotor	0.3
V_{sat}	power amplifier saturated voltage	$220\,V$
i_{sat}	power amplifier saturated current	$15\,A$

8.3 Homopolar AMB Optimization Results

The optimization design results of the HOMB supported rotordynamic system under different rotor spin speeds are displayed in this part. Different control strategies will also be compared and discussed. The multiple objective optimization result is presented in the form of Pareto frontier. For the solutions on the Pareto frontier, which is called Pareto optimal solutions or non-dominated solutions, no improvement is possible

in any objective function without sacrificing the other objectives. Thus on the Pareto frontier, all the solutions are optimal compromises among the conflicting objectives.

8.3.1 HOMB optimization with MOGAs under different spin speed

The spin speed of the rotor affects the windage loss and the unbalance of the rotor system. Optimizations were conducted at multiple speeds in order to illustrate the design process which includes accounting for variations in vibration behavior with speed. Speeds of 3600 rpm, 7200 rpm and 9000 rpm were selected to be representative of those occurring in industrial rotors for this size and weight class. The optimization starts with a random generated initial generation with 60 populations, and the optimization is convergent after 150 generations. The initial rotor positions are set to be 40% of the air gap clearance under the centered position. In each generation and each population, it varies with the air gap clearance, which is one of the design variables.

The Pareto frontiers in the final generation of the 3 objective HOMB optimization when the rotor spin speed is 3600 rpm, 7200 rpm and 9000 rpm are shown in Figure 71- Figure 73. The unbalances are set at node 11, which is the center of the rotor and excites the 1^{st} mode most. The unbalances are 1.45 kg·mm, 0.36 kg·mm and 0.3 kg·mm for the spin speed at 3600 rpm, 7200 rpm and 9000 rpm respectively. The Pareto frontiers in all the three plots clearly show the trade-off between the vibration amplitude and the actuator mass under different spin speeds, namely decrease in the vibration amplitude causes an increase in the actuator mass and vice versa.

Figure 72 shows that in the Pareto-optimal solution on the Pareto frontier, the smaller actuator mass and power loss will result in high steady state vibration amplitude and vice versa. When both the actuator mass and the vibration amplitude approximate the minimum values, which is at the left corner of the Pareto frontier, the power loss approached the maximum.

Figure 73 shows that to get less vibration amplitude, either the power loss or the actuator mass is increased. Also, the red dots at the left corner of the Pareto frontier show that when both the vibration amplitude and actuator mass are close to the minimum, the power loss is about the maximum.

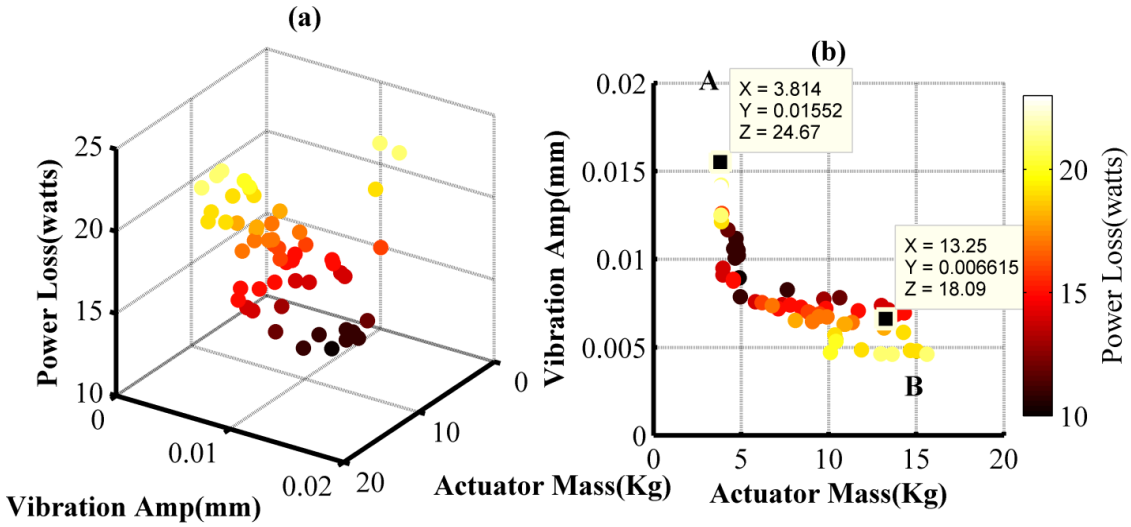

Figure 71 Pareto frontier of the multi-objective HOMB optimization- 3600 rpm (a) Pareto frontier (b) top view of the Pareto frontier

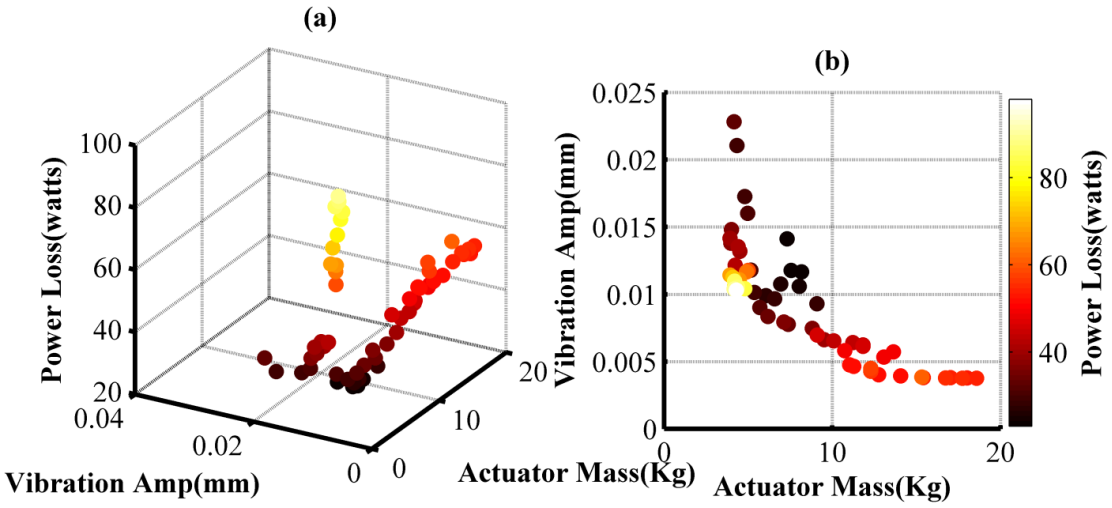

Figure 72 Pareto frontier of multi-objective HOMB optimization- 7200 rpm (a) Pareto frontier (b) top view of Pareto frontier

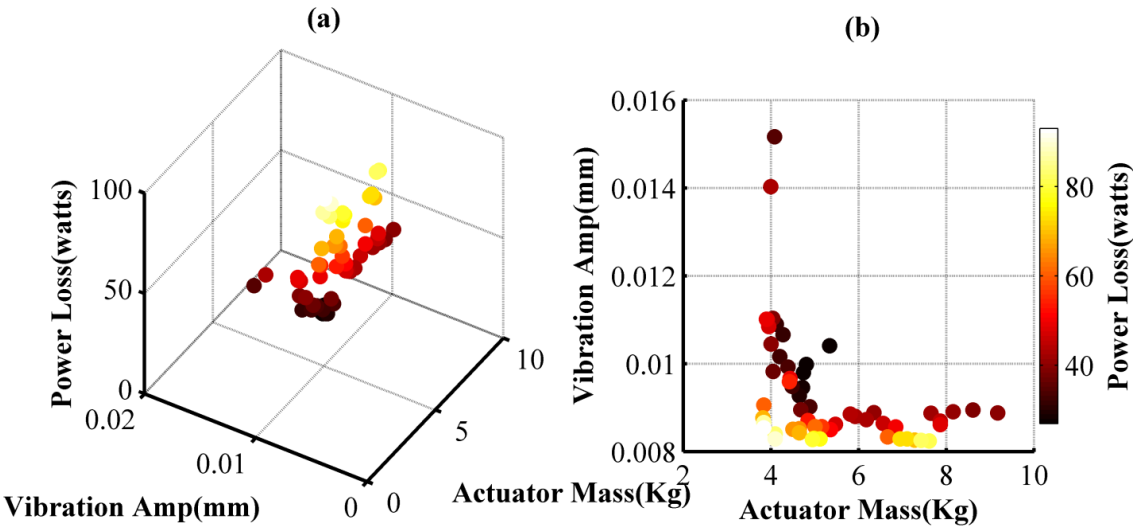

Figure 73 Pareto frontier of the multi-objective HOMB optimization- 9000 rpm (a) Pareto frontier (b) top view of the Pareto frontier

The general trends shown in the Pareto front plots in Figure 71, Figure 72 and Figure 73are a reduction of vibration with increased actuator mass, a “threshold actuator mass” below which the vibrations rise sharply, and increasing power loss with increasing

actuator mass. The peak vibration amplitude depends somewhat inversely with actuator mass. A second, and more subtle trend, is that the minimum achievable vibration on the Pareto front increases by approximately 25% as rotor speed increase from 7200 rpm to 9000 rpm.

Two points A and B on Figure 71, representing two sets of different designs are compared. The values of the 10 design variables at the two points are listed in the Table 7. The values of the three objectives and the amplification factors (AF) at the two points are listed in the Table 8.

Figure 74 shows the levitation simulation and rotor unbalance transient analysis of Point A on Figure 71. Figure 75 shows the levitation simulation and rotor unbalance transient analysis of Point B on Figure 71.

At point A, the optimization design result in an HOMB system which has an actuator of 3.81kg, and the steady state vibration amplitude with rotor unbalance is 0.016mm, and the power loss from the actuator is 24.7 watts. At point B, the optimization design result in an HOMB system which has an actuator of 13.3kg, and the steady state vibration amplitude with rotor unbalance is 0.007mm, and the power loss from the actuator is 18.1 watts. At both points, the rotor is successfully levitated from the catcher bearing positions and show good unbalance transient performance. As is clearly shown on the figures, the optimization design at point B has a much smaller vibration amplitude than it does at point A, but in the sacrifice of the actuator mass and power loss.

Table 7 Optimized design variables of point A and B on Figure 71

Design Variable	Design Variable	Point A	Point B
1	pole length along rotor axis, $l_p(m)$	0.01	0.028
2	air gap clearance, $l_g(m)$	0.00033	0.00030
3	permanent magnet thickness, $t_m(m)$	0.005	0.018
4	permanent magnet length, $L_m(m)$	0.023	0.036
5	air gap area, $A_g(m^2)$	0.00039	0.0025
6	permanent magnet area, $A_m(m^2)$	0.0014	0.0041
7	coil turns, N	56	43
8	stator inner radius, $r_c(m)$	0.081	0.083
9	proportional gain, G_p	60.3	27.6
10	derivative gain, G_d	0.25	0.19

Table 8 Objectives and amplification factors of point A and B on Figure 71

Variable	Variable description	Point A	Point B
1	Actuator mass(*kg*)	3.81	13.3
2	Power loss(*watts*)	24.7	18.1
3	Vibration amplitude(*mm*)	0.0155	0.0066
4	Amplification factor	2.43	3.62

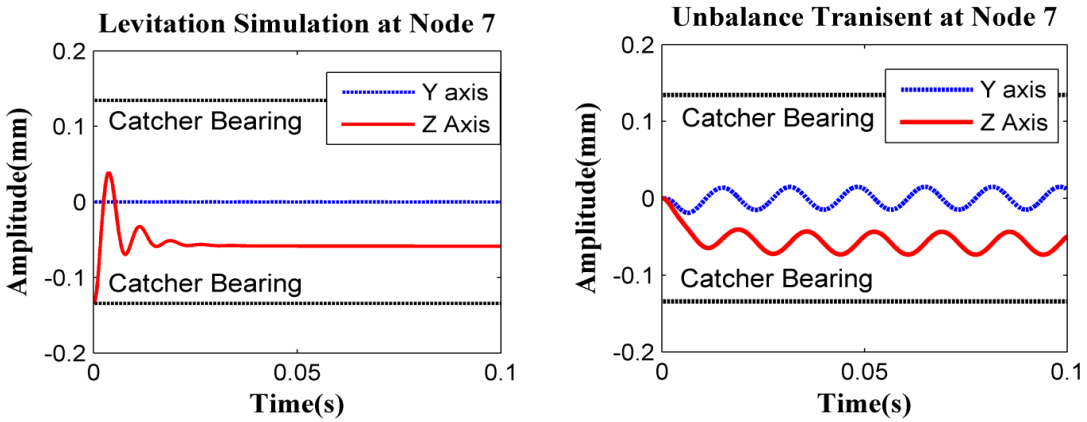

(a) *(b)*

Figure 74 Levitation simulation (a) and unbalance transient (b) analysis of point A on the Pareto frontier on Figure 71

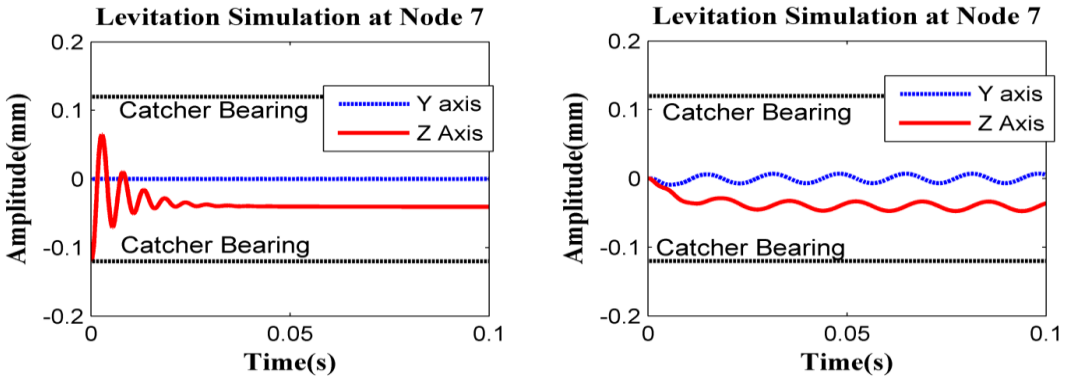

(a) *(b)*

Figure 75 Levitation simulation (a) and unbalance transient (b) analysis of point B on the Pareto frontier on Figure 71

8.3.2 HOMB optimization design with MOGAs using 2 stage control

The transient analysis includes two stages: the levitation stage where the actuator lifts the rotor from an initial position at zero speed, and the steady state stage where the rotor is spinning at a constant speed with an unbalance applied. In the levitation stage, due to the rapid change of displacement, the required magnetic force is large. So the voltage and current of the power amplifier, and the flux intensity in the poles, are very easily saturated. In the levitation stage, the controller needs to be carefully designed to avoid heavily saturated operation.

Figure 76 shows the HOMB optimization design with MOGAs using different PD controllers for the levitation stage and the steady state stage. The code is run when the spin speed is 3600 rpm, with all the other parameters staying the same with the optimization using the same controller throughout the two stages. To use different PD controllers for the levitation stage and the steady state stage, two extra PD controller gains are introduced as two additional design variables, resulting in 12 design variables.

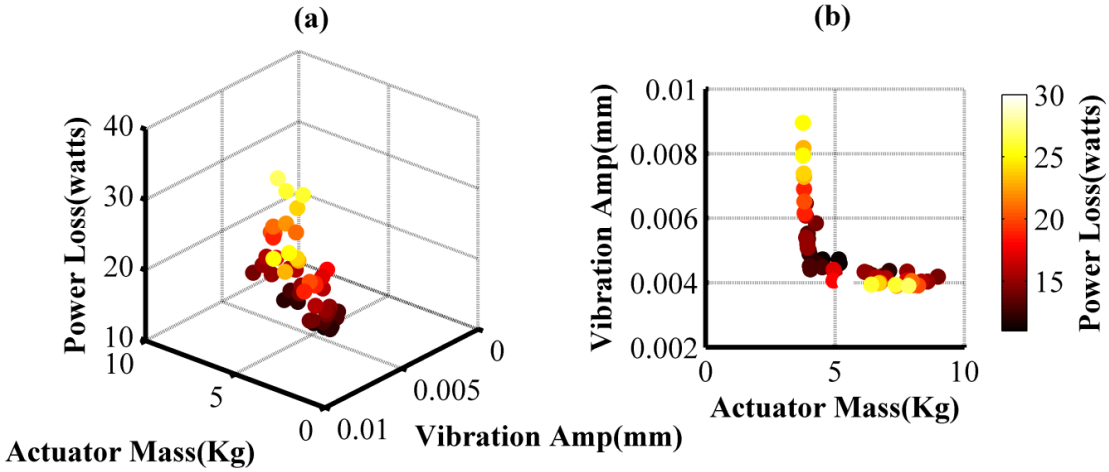

Figure 76 Pareto frontier of the multi-objective HOMB optimization with 2 stage control- 3600 rpm (a) Pareto frontier (b) top view of the Pareto frontier

Compared with Figure 71, it clearly shows a significant reduction of the steady state vibration amplitude and the actuator mass without too much increase in the power loss when using the 2 stage control.

To better demonstrate the benefits from the 2 stage control, Figure 77 is presented with the top views of the Pareto frontiers of the multi-objective HOMB optimization with single controller and 2 stage control under 3600 rpm spin speed. Compared with the single controller control, at the left corner on the Pareto frontier of the 2 stage control, the optimization comes with designs that the systems have much smaller actuator mass, lower vibration amplitude without much increase in the power loss.

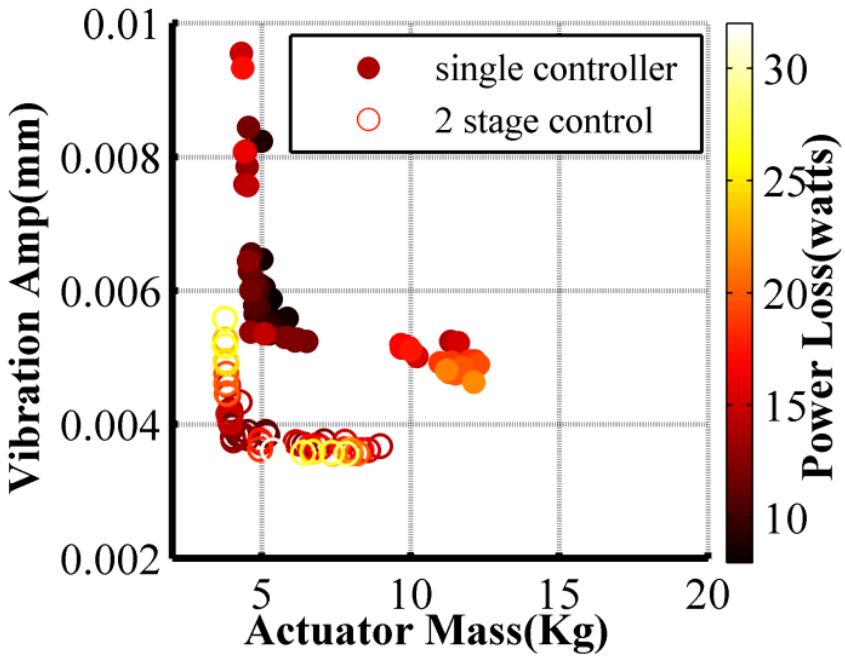

Figure 77 Top views of the Pareto frontiers of the multi-objective HOMB optimization with single controller and 2 stage control- 3600 rpm

Figure 78 is the top view of the Pareto frontier of the multi-objective HOMB optimization with single controller and 2 stage control under 7200 rpm spin speed. It also shows that the 2 stage control strategy reduces the actuator mass and vibration amplitude simultaneously compared with the single stage control.

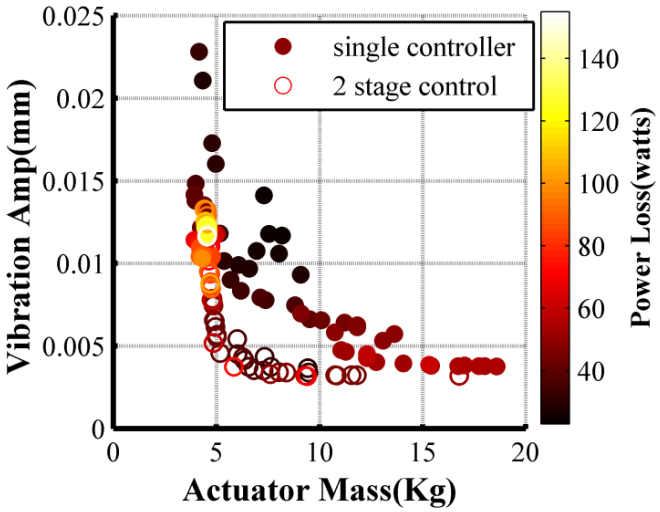

Figure 78 Top views of the Pareto frontiers of the multi-objective HOMB optimization with single controller and 2 stage control- 7200 rpm

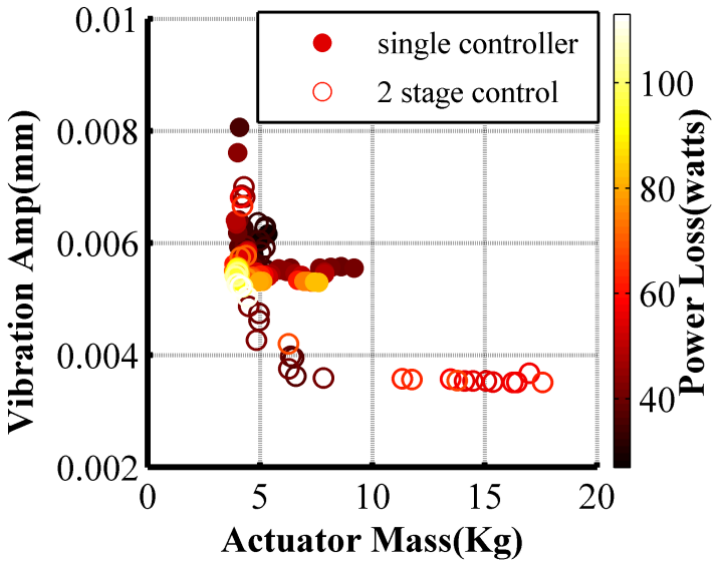

Figure 79 Top views of the Pareto frontiers of the multi-objective HOMB optimization with single controller and 2 stage control- 9000 rpm

Figure 79 is the top view of the Pareto frontier of the multi-objective HOMB optimization with single controller and 2 stage control under 9000 rpm spin speed. It

shows that at high spin speed (9000 rpm), the benefit from the 2 stage control is less than at the low spin speeds. However, the 2 stage control is still better than the single controller strategy in the optimization of the HOMB with the designs that comes with smaller steady state vibration amplitude with same amount of unbalance.

8.4 Summary of the HOMB Optimization Example

In this example, the NSGA-II algorithms are used to optimize the actuator and the PD controller of the homopolar magnetic bearing supported rotordynamic system. Three minimization type objectives are defined, including the actuator mass, the unbalanced rotor induced steady state vibration amplitude, and the power losses from the actuator. Eight actuator parameters and two PD controller gains were selected as design variables. Constraints were handled using the penalty-parameter-less method.

The best compromised optimization solutions, which are called Pareto solutions are presented in the form of Pareto frontier. For all the Pareto solutions, none of the objective can be improved in value without sacrificing any of the other objective. In this study, the Pareto solutions for the three objectives are given by the NSGA-II algorithms.

Closed-loop control of the rotordynamic system was simulated including both the levitation stage at zero spin speed and the steady state stage of the spinning, unbalanced rotor. A 2 stage control approach was utilized, which used different PD controllers for the levitation stage at zero speed, and at a steady state operating speed with unbalance. The 2 stage control approach is demonstrated to be able to further optimization one or more objectives.

This optimization uses linear analysis but with limits applied on the flux intensity, power amplifier voltage and current to count for the nonlinearities in the actual system. This means that designed system is not allowed to run in the saturation. But in real application, systems run in some extent of saturation may have higher load capacity and lower power loss. In the next section, a nonlinear model based on heteropolar magnetic bearing actuator which allows system saturation will be introduced.

9. HETEROPOLAR AMB OPTIMIZATION DESIGN EXAMPLE

In the previous section, we optimized the design of the actuator and the controller of the homopolar magnetic bearings supported rotor-bearing system using NSGA-II algorithms. The three minimization objectives included the shaft dynamic response (vibration), the actuator mass, and the actuator power loss. The magnetic bearing forces were linearized and represented by the bearing stiffness and the current stiffness. The study considered the nonlinearities in the AMB supported systems by limiting the power amplifiers and actuators operating in the linear range. The power loss in the actuator was estimated by the Carpenter's catalog map. The transient performance of the rotor with two stages was simulated; one was the levitation stage where the rotor was lifted from the catcher bearing locations at zero spin speed, and the other was the steady state stage where the rotor was spinning with rotor unbalance induced force. The present work is designed to optimize the design of the full nonlinear rotor-bearing system supported with heteropolar magnetic bearings. The goal is to get the most compact actuators with the highest static load and the lowest power loss under a certain hot spot temperature constraint and to the satisfaction of the ISO 14839 [32] standards. Compared with the previous work, the following novelties and improvements are made, 1) the simulated full nonlinear modeling allows the designed systems to run in the nonlinear range with saturation of power amplifiers and flux intensity. 2) Power loss from not only the magnetic bearing actuators but also the rotor was numerically determined since rotor loss can be significant in heteropolar AMBs systems. 3) Thermal modeling is included

with the finite element method (FEM) to determine the temperature distribution and predict the hot spot temperature of the designed magnetic bearing actuator. 4) The system is designed to bear a maximum additional static load applied at the center of the rotor in the steady state operation. 5) The steady state vibration amplitude and the sensitivity margin of the designed systems are checked to satisfy the ISO 14839 [32, 33] standards. 6) The optimization process is also managed by the optimization software Isight, which integrates the MATLAB code and conducts the optimization part. Different multi-objective algorithms in Isight were tested on this optimization problem, and finally NSGA-II and NCGA are selected to compare with the MATLAB coded NSGA-II algorithms due to their efficiency in finding feasible solutions and their fast convergence to the Pareto frontier.

9.1 Heteropolar AMB Optimization Problem Statement

In this study, three objectives are considered: minimizing the actuator mass, maximizing the static load at the center of the rotor, and minimizing the system power loss. Ten design variables, including the parameters describing the stators, the coils, the controllers, and the external static load are selected. The thermal analysis is coupled with the rotordynamic analysis so that the hot spot temperature at the steady state operation of the system can be predicted, and then checked with the upper temperature limit set as a constraint. Optimization constraints also include ISO standard check, and rotor levitation check to make sure the designed system has enough system dynamic capacity to lift the rotor.

9.1.1 Objectives

Reducing the actuator mass has been a major concern for the magnetic bearing design, especially in the applications of aerospace. According to NASA news, it costs $10,000 to put a pound of payload in Earth orbit. Schweitzer and Maslen [21] stated that a reduced unit load capacity is the main drawback of magnetic bearings in comparison to the rolling element bearings and fluid film bearings. Increasing the size of magnetic bearings at the design stage has been the way to solve the load capacity problem, resulting magnetic bearings generally having a larger size and mass. With all these concerns, the actuator mass is selected as the first optimization objective. The geometry of the stator and the coil is shown in Figure 7. The mass of the stator is

$$M_s = \rho_s A_s l_p \tag{156}$$

where ρ_s is the mass density of the stator, l_p is the effective length of the bearing, which is also the length of the pole, A_s is the surface area of the stator on the flux plane.

$$\begin{aligned} A_s = {} & \pi(r_s^2 - r_c^2) + 8[w_p(r_c - r_p)\frac{1}{2}\theta_1 r_c^2 - \frac{1}{2}\theta_2 r_p^2 \\ & - \frac{1}{2}w_p\sqrt{r_c^2 - (\frac{w_p}{2})^2} + \frac{1}{2}w_p\sqrt{r_p^2 - (\frac{w_p}{2})^2}] \end{aligned} \tag{157}$$

where $\theta_1 = 2\sin^{-1}(\frac{w_p}{2r_c})$, $\theta_2 = 2\sin^{-1}(\frac{w_p}{2r_p})$, r_s is the radius of the stator, r_c is the radius of the available coil space, w_p is the pole width, and r_p is the pole tip radius.

The mass of all the coils on the poles is

$$M_c = 8\eta\rho_c V_c \tag{158}$$

where V_c is the volume of the coil and η_c is the coil packing factor.

$$\begin{aligned} V_c &= ((w_p + 2t_c)(l_p + 2t_c) - w_p l_p) l_c \\ &= 2t_c l_c (w_p + 2t_c + l_p) \end{aligned} \tag{159}$$

and $A_c = t_c l_c = N\eta\pi(d_w / 2)^2$, so $l_c = N\eta\pi(d_w / 2)^2 / t_c$. The thickness of the coil t_c is

$$t_c = r_p \tan(\pi / n_p) - w_p / 2 \tag{160}$$

where n_p is the number of poles on each of the stator. In this case, $n_p = 8$.

As a result, the total mass of the actuator is

$$M_{actuator} = \rho_s V_s + 8\eta\rho_c V_c \tag{161}$$

$$\begin{aligned} M_{actuator} = \rho_s l_p \{\pi(r_s^2 - r_c^2) + 8[w_p(r_c - r_p)\frac{1}{2}\theta_1 r_c^2 - \frac{1}{2}\theta_2 r_p^2 \\ - \frac{1}{2} w_p \sqrt{r_c^2 - (\frac{w_p}{2})^2} + \frac{1}{2} w_p \sqrt{r_p^2 - (\frac{w_p}{2})^2}]\} + 16\eta\rho_c t_c l_c (w_p + 2t_c + l_p) \end{aligned} \tag{162}$$

As has been stated, a reduced unit load has been the main drawback of the magnetic bearings. Maximizing the static load is significant in the design of the magnetic bearings, thus is set as the third objective of the optimization.

An external static load is applied during the steady state operation at the center of the rotor in the same direction as the gravity force. An unbalance transient simulation is conducted with this static load. Therefore, in this transient process, the external forces on the rotor include the gravity force, rotor unbalance induced force, and this external static load. As listed in Table 9, the static load is also one of the design variables.

Minimizing the overall power loss is significant since it increases the efficiency for turbomachinery. The total power loss from the rotor and the stator during the steady

state operation of the system is evaluated and set as an objective to be maximized. In this operation, the horizontal rotor is loaded with an unbalance force and an external static force both at the center of the symmetric rotor.

9.1.2 Design variables

Ten design variables, reflecting the variation of the stator dimension, rotor profile, and the control strategy, are selected. The design variables and their respective bounds are listed in Table 9. Besides, this example also optimize the maximum static load of the magnetic bearing support system, thus the static load is also defined as a design variable.

Table 9 Design variables and respective bounds for heteropolar AMB optimization example

Design Variable	Quantity	Lower Bound	Upper Bound
1	bias current in the coil, $I_b(A)$	2	12
2	coil turn, N	60	200
3	cross sectional area of flux path in the air gap, $A_g(m^2)$	0.0002	0.003
4	radius of the rotor, $R_r(m)$	0.05	0.1
5	width of the pole, $w_p(m)$	0.015	0.04
6	radius of the coil space, $r_c(m)$	0.06	0.15
7	outer diameter of the stator, $r_s(m)$	0.08	0.16
8	proportional gain of the controller, G_p	5	30
9	derivative gain of the controller, G_d	0.01	0.05
10	static load, $F_{stat}(N)$	0	15,000

In this study, the power amplifier saturation voltage is set to be 220*V*, and the power amplifier saturation current is set to be 15*A*. The DC gain of the power amplifier from input voltage to output current is 1*V/A*. The bandwidth is set to be 6283*rad/s*, which is a typical 1*kHz* for power amplifiers.

9.1.3 Constraints

The constraints of the system come from the geometry of the actuator, the dynamic capacity of the system to levitate the rotor from an initial location, the maximum vibration displacement of the rotor checked with the ISO standards, and the high temperature limit of the actuator. According to these, 7 constraints are listed:

1. The length of the coil is limited to the available space in the stator and can be expressed as

$$l_c \le (l_c)_{\max} \tag{163}$$

where $(l_c)_{\max} = \sqrt{r_c^{\,2} - (t_c + w_p / 2)^2} - r_p$.

2. Width of the coil is larger than the coil diameter,

$$t_c \ge d_w \tag{164}$$

where d_w is the diameter of the coil, and t_c is the width of the coil bulk. For this 8-poles case,

$$t_c = r_p \tan 22.5^\circ - w_p / 2 \tag{165}$$

3. The magnetic bearings shall be able to levitate the rotor against the gravity from an initial released position. In this case, the rotor is initially rested on the catcher

bearings, which are ball bearings designed to prevent the unexpected contact between the rotor and the magnetic bearing stator in cases of overload or failure of the magnetic bearings. The catcher bearing clearance is generally half of the centered air gap clearance. The catcher bearing is simplified as a spring-damping model with tangential friction force. In this levitation, there is no friction force from the catcher bearing since the rotor is lifted at zero spin speed. A high fidelity modeling of the catcher bearing drop events with life prediction, which provides a specified number of safe stops from full speed or worst case load conditions, will be conducted in the future. In this study, levitation is accepted if the controller is able to lift the rotor from the catcher bearing location to at least half of the catcher bearing clearance at steady state operation. Mathematically, it is expressed by

$$z_{ss} - z_{initial} > c_{cb} / 2 \tag{166}$$

where z_{ss} is the steady state vertical rotor displacement, $z_{initial}$ is the initial vertical rotor displacement, c_{cb} is the catcher bearing clearance, $z_{initial} = -c_{cb}$, and $c_{cb} = g / 2$.

4. The vibration displacement of the rotor shall qualify the limits by ISO 14839 standards, which are developed specifically for rotating machinery equipped with AMBs. ISO 14839 establishes vibration zone guidelines for magnetic bearings. For newly commissioned machines, the vibration displacement should be lower than 0.3 of the minimum radial clearance.

5. The catcher bearing clearance is generally taken as the minimum radial clearance.

This optimization sets a constraint to ensure the designed systems meet this newly commissioned machine vibration displacement requirement. The maximum

vibration displacement is measured from the steady state of the unbalance transient simulation. The amount of the unbalance is 1.5kg·mm, which adds an external force of about 10% of the rotor weight and is phased to 90° to excite the most 1st mode.

6. The hot spot temperature of the actuator should be limited. ISO14839-2 [32] states that the temperature is one of the most important factors affecting the reliability of the AMB system that should be kept within range. The hot spot temperature is limited to 175^0F as a constraint in the optimization. The temperature distribution and the hot spot temperature are predicted with the 2D finite element method as shown in section 6.2.

7. To ensure that there is enough flux path area in the radial direction of the stator, the stator thickness should be larger than the pole width.

$$r_s - r_c - w_p > 0 \tag{167}$$

8. To ensure that there is enough flux path area in the rotor, the stack thickness of the laminated iron cobalt should also be larger than the pole width.

$$R_r - R_j - w_p > 0 \tag{168}$$

where R_j is radius of the un-laminated (solid) journal.

As a summary of the optimization objectives, design variables and constraints, the optimization code flow chart of the heteropolar AMB system is shown in Figure 80.

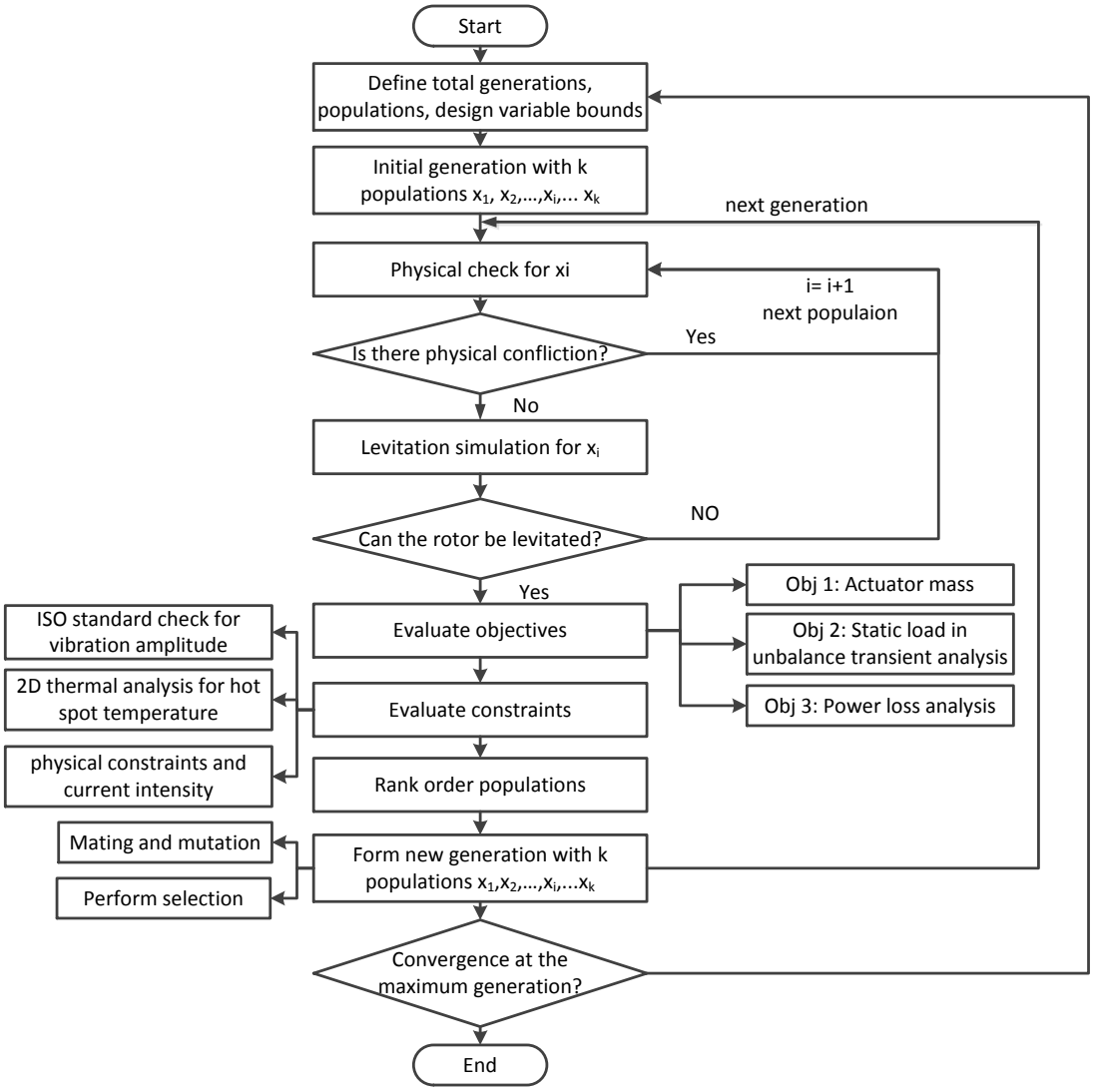

Figure 80 Code flow chart of the heteropolar AMB system optimization example

Similarly to the homopolar design example, to speed up the computation, the code first checks the physical conflictions of the design variables. The levitation simulation, which is used for check the dynamic load capacity, is only conducted for the designs without physical conflictions. Afterwards, unbalance transient analysis is conducted only for the system that can be successfully levitated. The power amplifier

current and the flux intensity in the steady state operation of the unbalance transient analysis are extracted, and used for the calculation of the power loss in the stator and the rotor. The finite element method is used to determine the temperature distribution of the actuator, and check if the highest temperature exceeds the set limit. Besides, the maximum rotor displacement in the unbalance transient process is checked with the ISO 14839 standards.

9.2 Heteropolar AMB Optimization Example Results and Discussions

In this part, the best-compromised solutions of the optimization are presented in the form of Pareto frontier with the NSGA-II algorithms in MATLAB. Representative Pareto solutions will be taken from the Pareto frontier. The rotordynamic performance, power loss, and hot spot temperature of the designs at these representative points will be presented and compared. Besides, nonlinearities of the AMB supported system at these designs will be illustrated.

9.2.1 Pareto frontier and optimization results

The optimization is conducted with a rotor steady state spin speed of 3600 *rpm* and the rotor unbalance of 1.5*kg·mm* at the center of the rotor with a phase angle of 90°. In this example, the code runs 120 generations, with 40 populations in each generation. In the final generation, all 40 populations are feasible solutions with all the constraints satisfied. However, only 30 populations are Pareto solutions, as presented in the Pareto frontier in Figure 81. The figure clearly shows the trade-off between the static load and

power loss, which means that the power loss becomes higher to get a higher static load and vice versa.

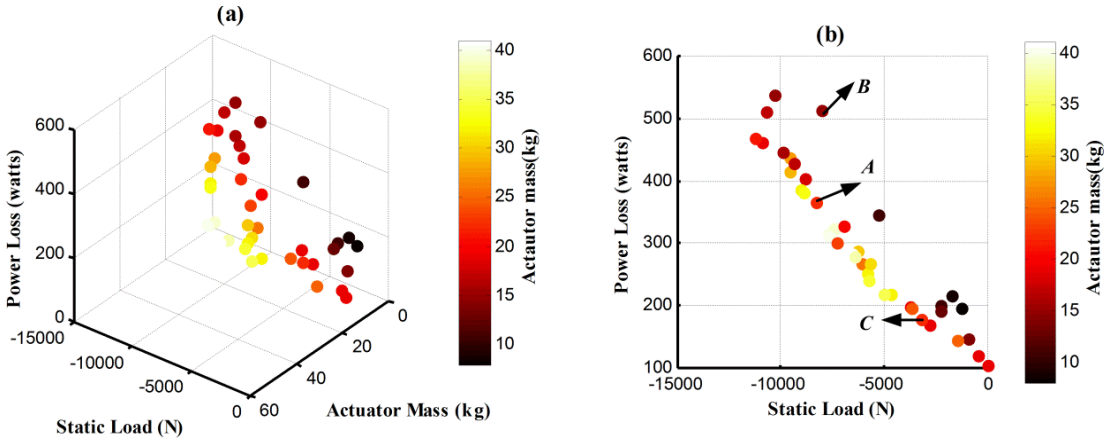

Figure 81 (a) Pareto frontier of the heteropolar AMBs optimization (b) side view of the Pareto frontier

Three representative points A, B, and C are taken from Figure 81 for comparison. Each point corresponds to a design of the AMB system. The design variables at the three points are listed in Table 10.

The three objectives values, the hot spot temperature, the steady state vibration amplitude, and other parameters at the three points are listed in Table 11. Comparison between the designed AMB systems at point A and point B shows that while the designs at the two points result in actuators with similar mass, the design at point A allows much higher static load at the center of the rotor with the sacrifice of producing higher power loss. Comparison between the designs at point A and point C shows they bear equivalent level of static load at the center of the rotor, but point A results in lower system power loss with the sacrifice of larger actuator mass.

Table 10 Design variables of the representative designs on Pareto frontier for heteropolar AMB optimization example

Design Variable	Quantity	Point A	Point B	Point C
1	bias current in the coil, $I_b(A)$	4.0	6.4	3.8
2	coil turn, N	179	168	173
3	cross sectional area of flux path in the air gap, $A_g(m^2)$	0.0021	0.0016	0.0017
4	radius of the rotor, $R_r(m)$	0.0745	0.0863	0.0746
5	width of the pole, $w_p(m)$	0.0241	0.0263	0.0239
6	radius of the coil space, $r_c(m)$	0.1124	0.1078	0.1126
7	outer diameter of the stator, $r_s(m)$	0.1369	0.1353	0.1435
8	proportional gain of the controller, G_p	16.8	16.9	15.4
9	derivative gain of the controller, G_d	0.024	0.023	0.029
10	static load, $F_{stat}(N)$	8251.1	7995.7	3180.9

Table 11 Objectives and other parameters of the representative points on Pareto frontier for heteropolar AMB optimization example

Parameter	Parameter Description	Point A	Point B	Point C
1	actuator mass(*kg*)	22.1	15.3	21.2
2	static load(*N*)	8251.1	7995.7	3180.9
3	power loss(*watts*)	365.8	512.1	178.4
4	hot spot temperature(°*F*)	127.2	114.9	101.2
5	maximum displacement with load and unbalance (*mm*)	0.058	0.051	0.035
6	ohmic loss(*watts*)	242.0	285.5	109.0
7	hysteresis loss in the rotor(*watts*)	84.3	151.8	49.2
8	eddy current loss in rotor(*watts*)	33.2	68.3	15.6
9	windage loss in rotor(*watts*)	5.2	6.1	4.2

To better demonstrate and compare the performance of the designed systems, this part will show the rotordynamic and thermal behaviors at the three points. Figure 82 plots the transient levitation analysis of the designed system at point A. It shows that the

designed magnetic bearing actuator and the respective PD controller can successfully levitate the rotor from the catcher bearings locations marked with red dashed line at the -0.25*mm*. Figure 83 presents the flux intensity and the current in the power amplifier corresponding to the upper electromagnetic core during levitation. The upper core is most easily saturated in flux intensity and current since it supplies the magnetic force to counter the gravity of the rotor and the applied external static load. Figure 83 shows during levitation, slight saturation in the flux intensity occurs at about 2.7*ms* and 5.4*ms*, and slight current saturation occurs at about 2.7*ms* during the levitation.

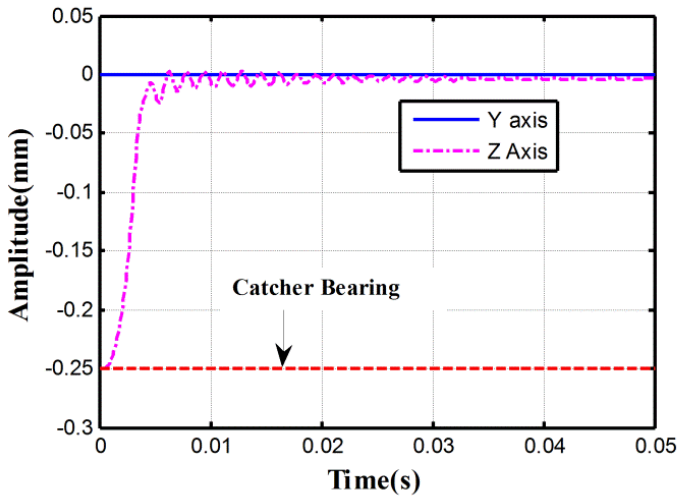

Figure 82 Levitation simulation at point A on the Pareto frontier in Figure 81

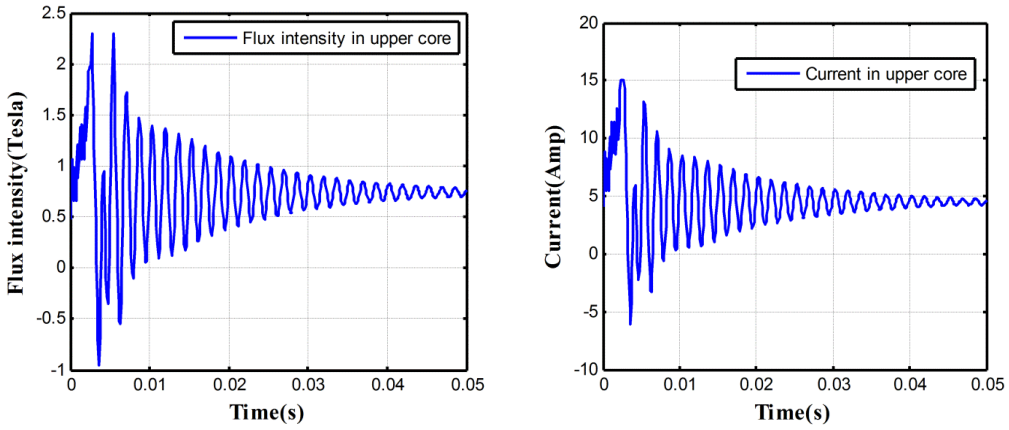

(a) *(b)*

Figure 83 (a) Flux intensity and (b) the power amplifier current during the levitation at point A

Figure 84 shows the translational displacement during the unbalance transient analysis at point A. Due to the static load from both rotor weight and the applied external force of 8251.1*N*, there is an eccentricity of -0.058*mm* in the z- direction. However, even with the eccentricity from the static load, the maximum displacement of the rotor satisfies the requirement for newly commissioned machines in the ISO14839 standard, which should be less than 0.075*mm* in this case.

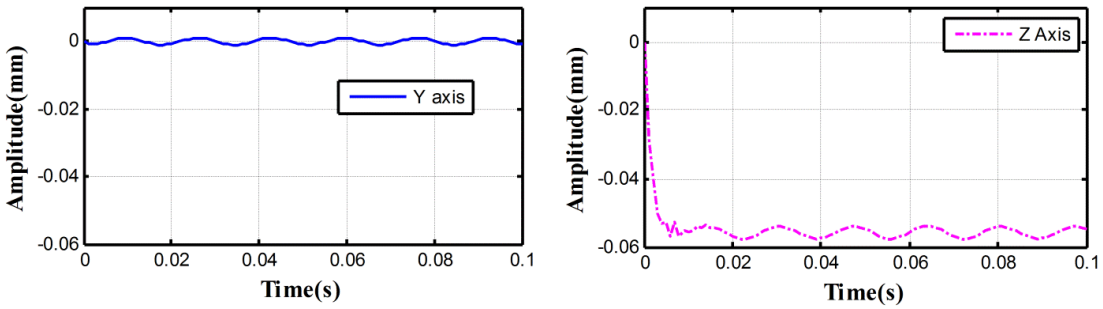

(a) *(b)*

Figure 84 Translational displacements (a) y- direction (b) z- direction in the unbalance transient analysis at point A

Figure 85 presents the flux intensity and the power amplifier current corresponding to the upper electromagnetic core during the steady state unbalance transient analysis with the applied external load of 6577.0*N*. There is no flux saturation or current saturation in the unbalance transient simulation at point A.

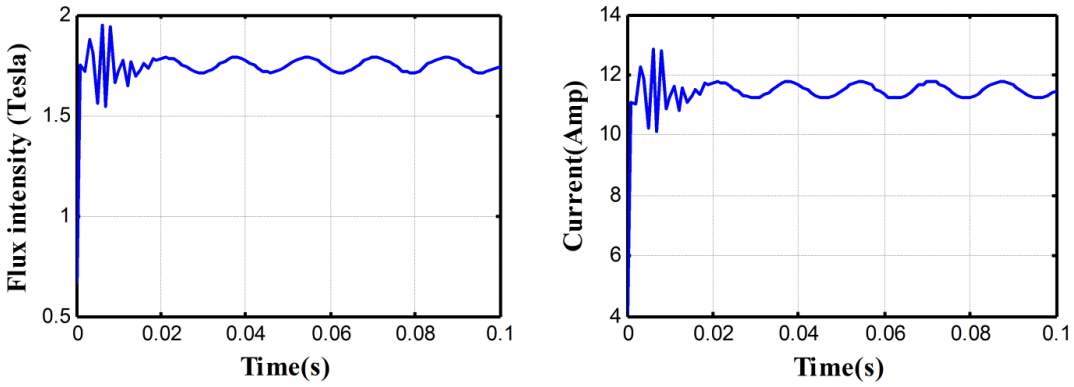

(a) *(b)*

Figure 85 (a) Flux intensity and (b) the power amplifier current during the unbalance transient at point A

Figure 86 presents the transient levitation simulation of the rotor in the designed system at point B. It shows successful levitation of the rotor from the catcher bearing position. Figure 87 shows the flux intensity and the power amplifier current corresponding to the upper electromagnet core during the levitation process. Flux intensity saturation occurs during 5.3*ms*~5.7*ms*, and power amplifier current saturation occurs during 1.2*ms*~2.6*ms* and at about 5.5*ms*.

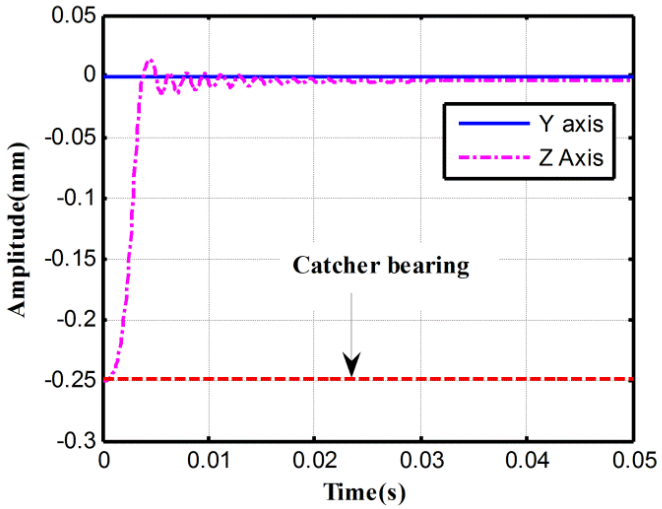

Figure 86 Levitation simulation at point B on the Pareto frontier in Figure 81

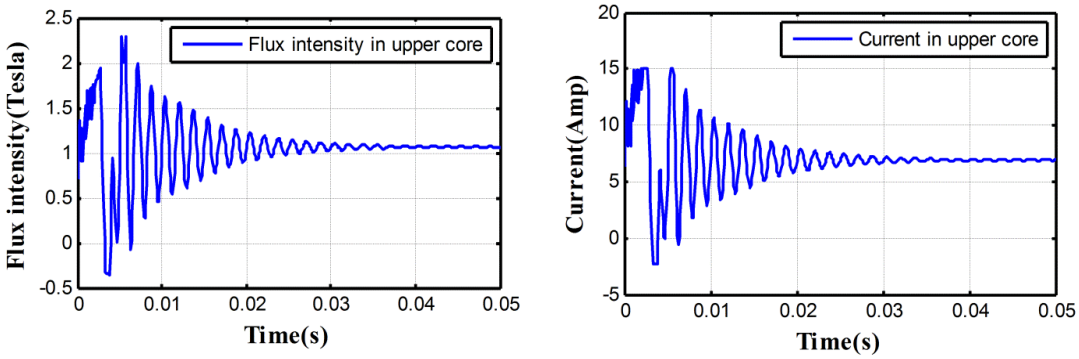

(a) *(b)*

Figure 87 (a) Flux intensity and (b) the power amplifier current during the levitation at point B

Figure 88 shows the translational displacement of the rotor of the designed system at point B with rotor induced unbalance and the applied external static load of 7995.7*N*. The maximum displacement is - 0.051*mm*, which satisfies the newly commissioned machines standards.

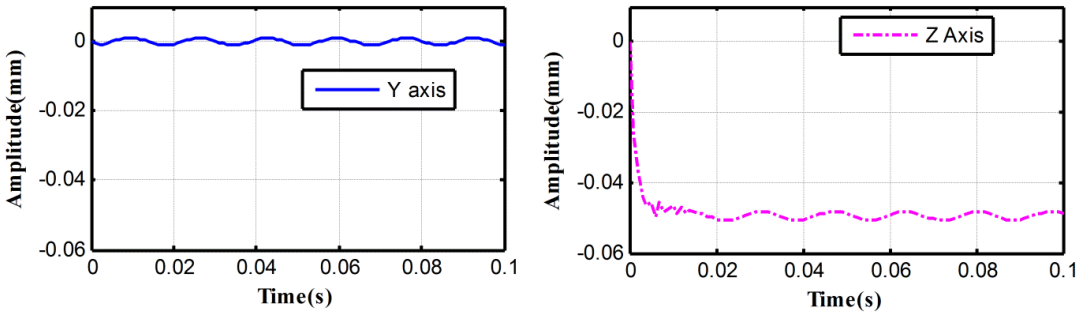

(a) *(b)*

Figure 88 Translational displacements (a) y-axis (b) z-axis in the unbalance transient analysis at Point B

Figure 89 shows the flux intensity and the power amplifier current corresponding to the upper electromagnet core during the unbalance transient simulation at point B. It shows slight flux saturation and slight power amplifier current saturation at around 6ms. At point B, the steady state flux intensity is about 1.8 *Tesla*, and the steady state current is about 13 *amps*. The large current results in high ohmic loss, and large flux intensity results in high eddy current loss and high hysteresis loss in the rotor, as is presented in Table 11. As has been stated, the design at point B has an equivalent static load compared to the design at point A, but it has smaller actuator mass with the sacrifice of producing higher power loss. This loss is caused by increased flux intensity and current which allows some degree of saturation in the unbalance transient process.

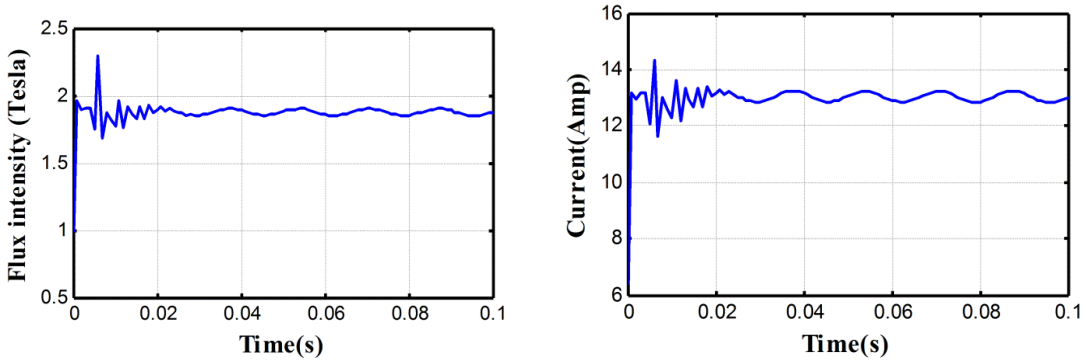

(a) *(b)*

Figure 89 (a) Flux intensity and (b) the power amplifier current during the unbalance transient at point B

Figure 90 shows the successful levitation of the rotor from the catcher bearing position in the designed system at point C. Figure 91 shows the flux intensity and the power amplifier current corresponding to the upper electromagnet core during levitation. The plot shows flux saturation at about 5.7*ms* and power amplifier current saturation from 2.3*ms*~3*ms*.

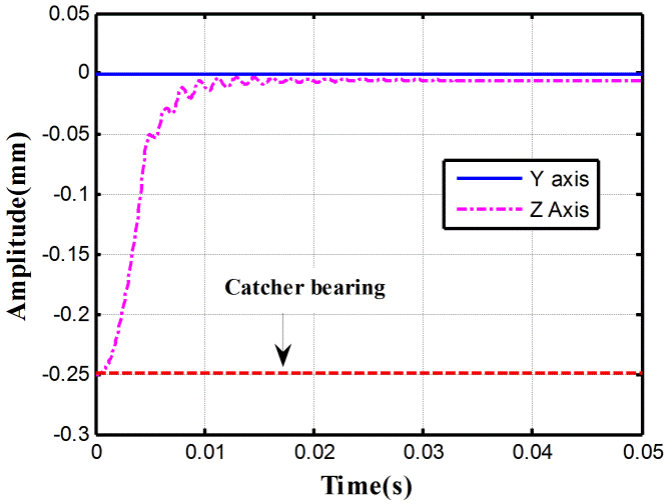

Figure 90 Levitation simulation at point C on the Pareto frontier in Figure 81

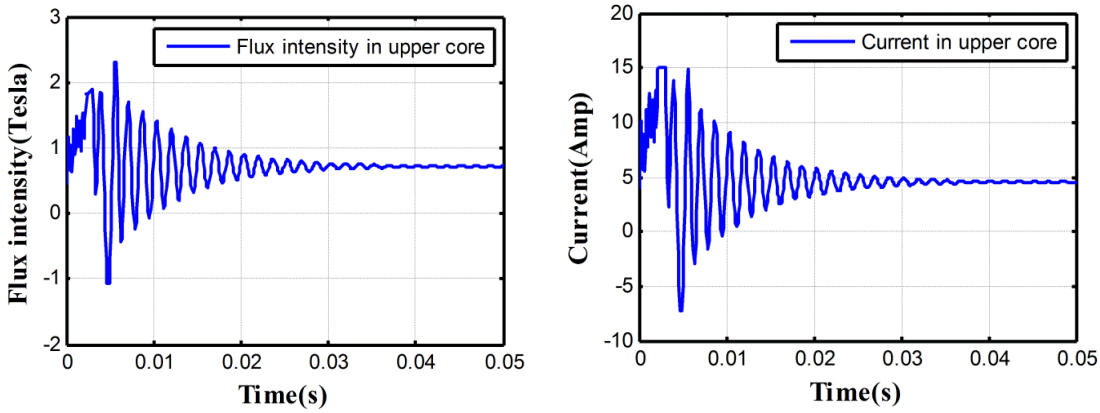

(a) *(b)*

Figure 91 (a) Flux intensity and (b) the power amplifier current during the levitation at point C

Figure 92 shows the translational displacement of the rotor during the unbalance transient analysis with the applied external static load of 3180.9*N* at point C. The maximum displacement is -0.035*mm*, which is smaller than it is at point A and B due to the much smaller applied external load. Figure 93 shows the flux intensity and the power amplifier current corresponding to the upper electromagnet core at point C during the simulation. There is no flux saturation or power amplifier current saturation.

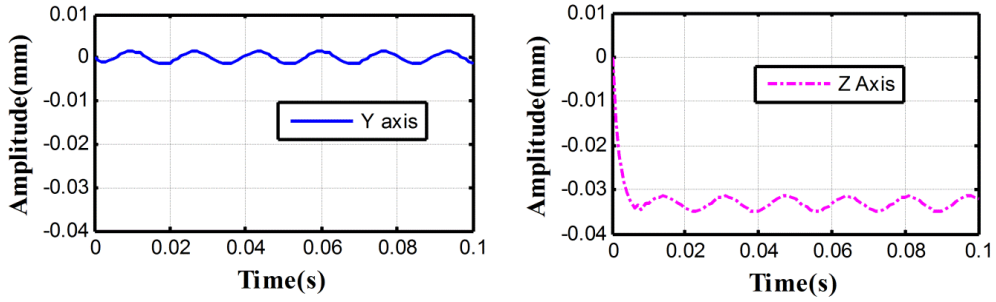

(a) *(b)*

Figure 92 Translational displacements of (a) y- axis (b) z-axis in the unbalance transient analysis at Point C

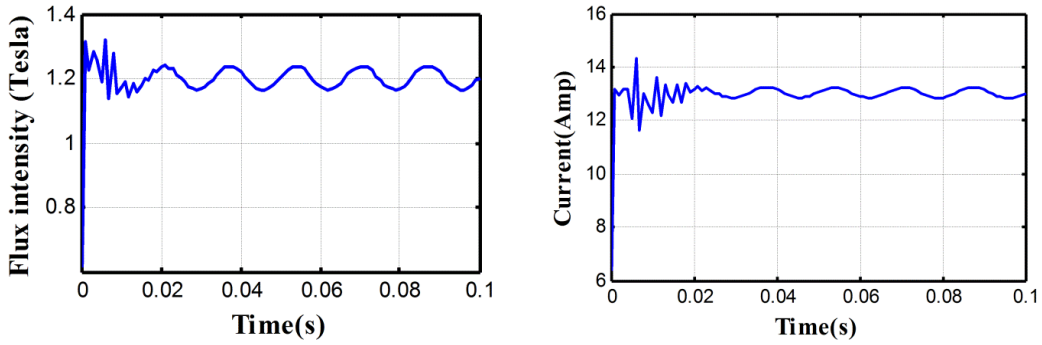

(a) *(b)*

Figure 93 (a) Flux intensity and (b) the power amplifier current during the unbalance transient at point C

Figure 94 shows the hot spot temperature verses the three objectives. The plots show that the static load and the power loss, rather than the actuator mass, dominate the hot spot temperature. To get lower hot spot temperature, the static load and the power loss of the system would be limited.

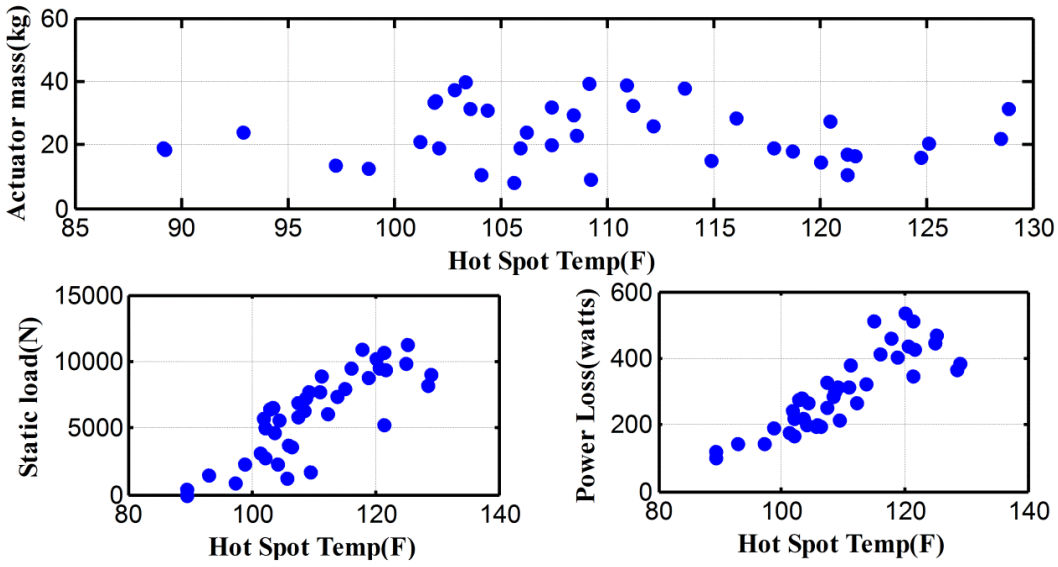

Figure 94 Hot spot temperature V.S. objectives

Power loss components of the designed system at point A are listed in the pie chart form in Figure 95. The main power loss comes from the ohmic loss, which takes about 66.2% of the total system power loss. The ohmic loss mainly comes from the bias current that counters the rotor gravity force and the large applied external force at the center of the rotor. The hysteresis loss in the rotor is significant due to alternating polarities in the heteropolar magnetic bearings. This takes about 23.1% of the total power loss. The windage loss is low in this case where the rotor is at low spin speed (3600 *rpm*). However, the windage loss grows with spin speed and could be dominant at high speed operation. Figure 95 suggests that the other losses in the stator, including the hysteresis loss and eddy current loss caused by the flux field change, are very small and can be ignored. The flux field change in the stator comes from the control current to counter the rotor unbalance induced force. Unless the rotor is heavily unbalanced, which is rare in rotordynamic applications, the control current is small resulting in slight flux field change in the stator. Thus the hysteresis loss and the eddy current loss in the stator are generally small compared to they are in the rotor.

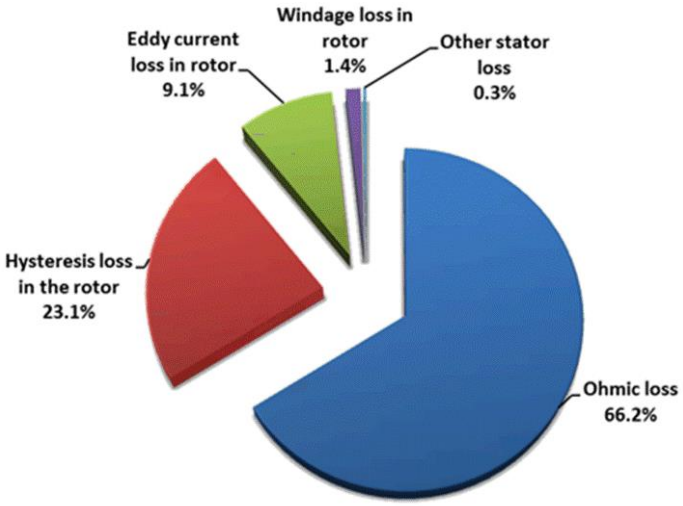

Figure 95 Power loss components of the designed system at point A

The 2D thermal analysis of the designed magnetic bearing actuator at point A is presented in Figure 96. The hot spot temperature occurs in the coil, which is 127.2°*F*.

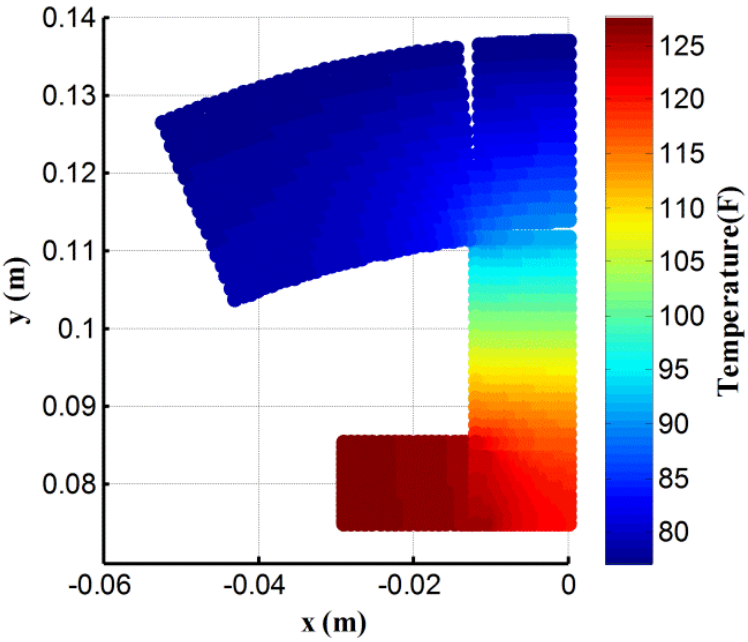

Figure 96 2D thermal analysis of the designed AMBs supported system at point A

To validate the 2D thermal modeling and the symmetric assumption of the actuator, a 3D thermal analysis of the designed actuator is conducted with the thermal analysis tool in Solidworks. An example comparing the approximated symmetric model and the actual model is shown in Figure 97 and Figure 98. In Figure 97 the currents in the +z, -z, +/-y direction poles are 11.2*amps*, 3.5*amps*, and 4.0*amps* respectively, which is set according to the coil currents of the designed system at point A at steady state operation. In Figure 98, all the poles have a coil current of 11.2*amps*, which is equal to the maximum coil current, occurring in the +z poles to counter the gravity force and the static load. A comparison between Figure 97 and Figure 98 shows that the symmetric assumption does not have too much impact on predicting a hot spot temperature. The hot spot temperature predicted is higher than the actual model by 2%, which is totally acceptable for a conservative model.

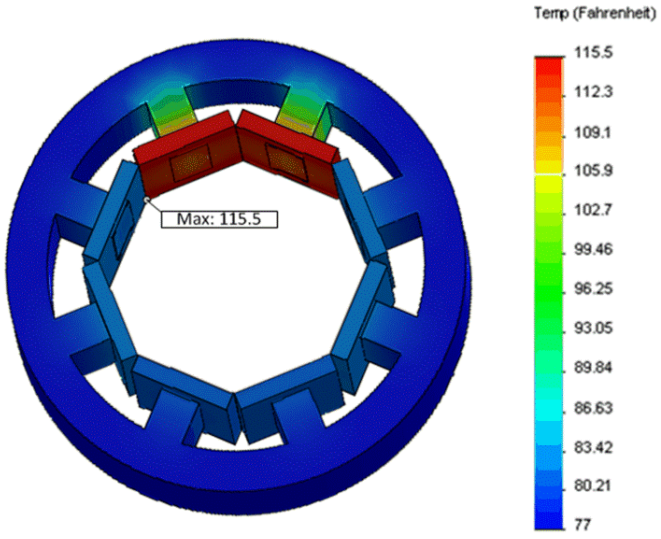

Figure 97 Solidworks thermal modeling with actual currents in the poles

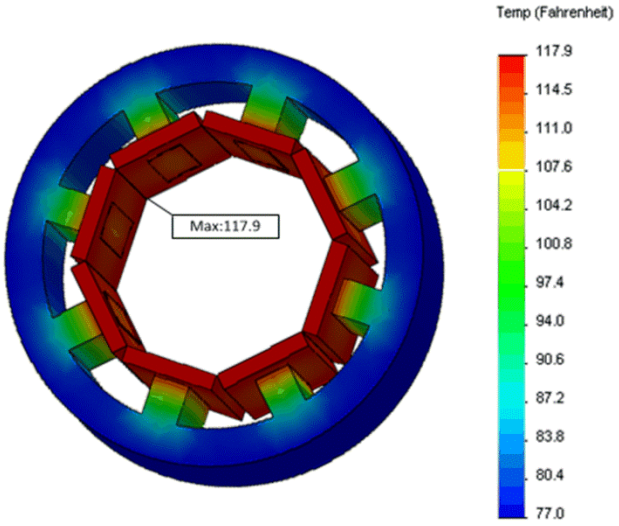

Figure 98 Solidworks thermal modeling under symmetric actuator model

A comparison between Figure 96 and Figure 98 shows that the 2D thermal model predicts a higher hot spot temperature since the 2D model neglects the natural convection in the axial direction. As a conclusion, the thermal modeling with 2D and symmetric assumptions is an efficient and conservative model in predicting the hot spot temperature using the minimum computation time.

The sensitivity margin of the designed AMB supported nonlinear system at point A is evaluated by linearizing the system with the rotor centered. A Bode plot of the sensitivity function and four different stability zones are shown in Figure 99. For the point A corresponding designed system, the value of the peak sensitivity magnitude is 3.7; thus is characterized as zone B which is acceptable for unrestricted long-term operation according to the zone limit values.

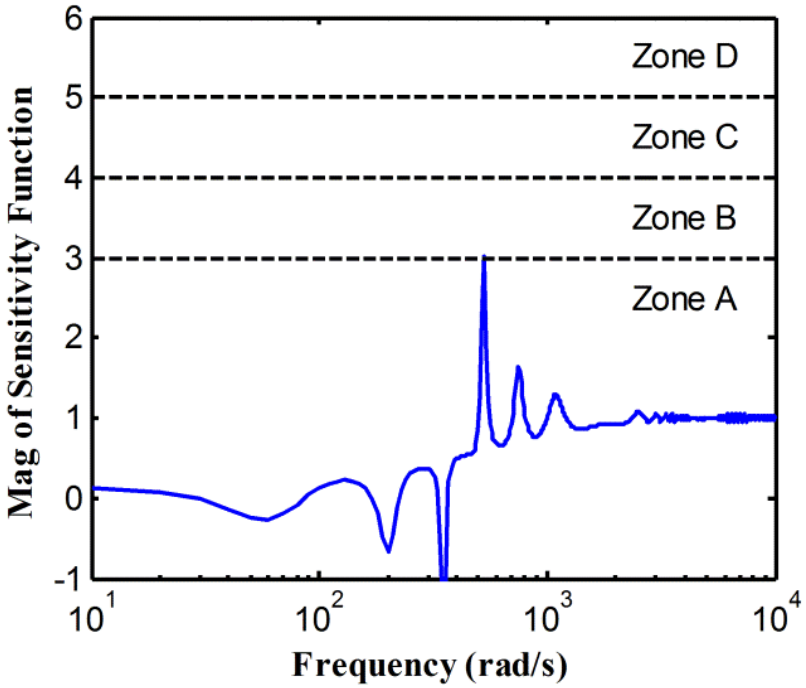

Figure 99 Evaluation of the stability margin of the designed system at point A

9.2.2 Optimization design with Isight

The study also uses the optimization software Isight to integrate the simulation into its optimization tool. In this optimization design of the magnetic bearings supported systems, the initial generations are produced randomly. Due to the large number of design variables and constraints, very few populations in the first generation are feasible solutions. Among the four available multi-objective optimization algorithms in Isight, only NCGA and NSGA-II work well for this complex system optimization design problem, developing more and more feasible solutions in the later generations and converging to find Pareto solutions efficiently. The Figure 100 shows the Pareto frontier of the optimization design with different algorithms.

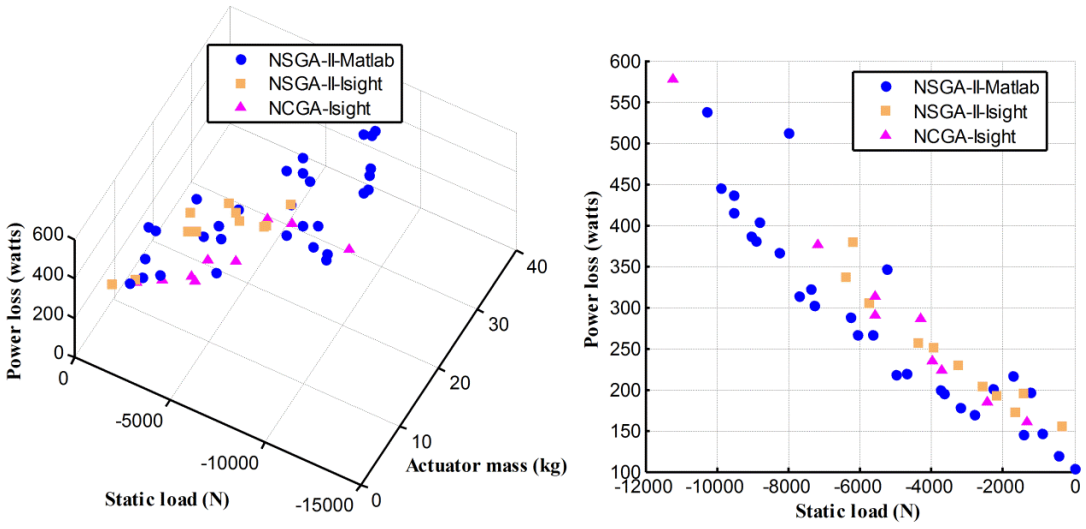

(a) *(b)*

Figure 100 Comparison of the MATLAB coded NSGA-II with NSGA-II and NCGA in Isight

Figure 100 shows that the NSGA-II in Isight is quite comparable to the Matlab NSGA-II, except that there are fewer Pareto solutions in a narrower range. The NCGA gives Pareto solutions in about the same range of the solutions by MATLAB NSGA-II, but with even fewer Pareto solutions. The MATLAB NSGA-II has the best performance in finding more Pareto solutions in a wider range.

9.3 Summary of the Heteropolar AMB Optimization Design

This example study focuses on the optimization design of the heteropolar magnetic bearing actuator and the controller simultaneously to make the desired system with the minimum actuator mass, minimum power loss, and the maximum static load applied at the center of the rotor. The optimization models a full nonlinear rotor-bearing

system, with simulation of levitation, imbalance transient and thermal modeling. Two multiple objective genetic algorithms, including NSGA-II and NCGA, were utilized and compared to find the Pareto solutions. The 2D finite element method (FEM) was used to determine the temperature distribution and find the hot spot temperature of the actuator. The vibration level and the stability margin of the designed rotordynamic system were checked with the ISO 14839 standards. Trade-off among the objectives and the compromise of the objectives can be achieved by the multi-objective optimization algorithms and presented with the Pareto frontier. The optimization result demonstrates that some extent of the power amplifier current saturation and the flux intensity saturation, especially in the levitation stage, helps in making actuators with smaller mass, higher static load, but higher power losses.

10. CONCLUSIONS AND FUTURE DIRECTION OF WORK

This study focused on optimization design of the active magnetic bearing supported flexible rotor with flexible support, considering the system nonlinearities, the temperature limits, and the ISO standards acceptance check. The study illustrated general objectives, constraints, and key parameters in the design of magnetic bearing systems, and presented the genetic algorithms as a tool to solve complicated optimization problems.

10.1 Conclusion of Completed Work

The current research focuses on the followings:

1) Model a full magnetic bearing system, including a flexible rotor, and flexible foundation effects. The flexible rotor is modeled with finite element method. A flexible rotor has a much wider mechanical bandwidth than a rigid rotor, which resulting in a much larger response to high frequency forces. Thus for flexible rotors, the controller design at high frequencies is much more important than for rigid rotors. Besides, this flexible rotor model allows non-collocated sensors and actuators, when there will be flexible modes with a node between a sensor-actuator pair. The flexible support is model with experimentally measured compliance frequency response function (FRF). The method does not require the acknowledgement of the mass of the stator, and is suitable for the support of any type of bearing. Besides, the method

uses state space representation form to deal with the highly cross-coupled dynamic compliances between different locations and directions. With this method, both the modal stability analysis and transient analysis of the system with the flexible support can be modeled.

2) Develop a reliable nonlinear model to predict the magnetic bearing supported rotor-bearing system. The nonlinearities include nonlinear magnetic material (flux saturation), nonlinear magnetic bearing force with respect to the rotor displacement and control current, the current and voltage saturation in the power amplifier, and the catcher bearing effects.
3) Besides the rotordynamic performances, other properties, including the power losses of the system, the thermal field of the actuator, and the vibration amplitude of the rotor as well as the sensitivity margin as required in ISO14839/API617, are analyzed to have a practically reliable design of the magnetic bearing system.
4) Apply the optimization techniques, including NSGA-II and NCGA into the optimization design of the complex magnetic bearing system. The optimization problem is designed to have multiple design variables, including actuator dimensional parameters, controller gains, and even external load, simultaneously vary in a range to find the best sets that can make all the desired objectives the best. As the design of the complicated magnetic bearing system is one of the major concerns that draw back the more wide spread of AMBs, this optimization methods present a tool for the successful

design of the system with large number of design variables, multiple objectives, and constraints.

10.2 Future Direction of Work

In the nonlinear analysis of this study, the catcher bearings are represented by a simplified model, which uses a constant stiffness coefficient, a constant damping coefficient, and a tangential friction coefficient. In the actual applications, the catcher bearing forces are much more complicated. A high fidelity catcher bearing model would be expected for a more accurate modeling of the magnetic bearing supported system.

The optimization of the system, which involves the iteration of various simulations, for example nonlinear transient simulation of the rotor, finite element thermal modeling of the actuator, and ISO/standard acceptance check, takes hours of computation time. For future study, it will be important for the researchers to perform optimization of the code to make it more effective and less computationally expensive. Two possible methods, one of the modal reduction of the rotordynamic system, and the other of the surrogate model to substitute any expensive objective function or constraint function in the optimization, are recommended for future researchers.

10.2.1 High fidelity catcher bearing model

Catcher bearings are designed for a limited number of rotor drops, rather than continuous operation. A proper design of the magnetic bearing supported rotors includes

the use of catcher bearing surfaces for both radial and axial loading considerations. The designed catcher bearings should satisfy the following requirements:

1) When the power to the magnetic bearing system is off, the rotor rests on the catcher bearings. The rotor should be able to roll over without destroying the magnetic bearing stator or the rotor.
2) When there are excessive loading forces, the catcher bearings should be able to provide support to prevent the rotor from contacting the AMB stator.
3) During power or component failures, the catcher bearings shall provide a specified number of safe drops from full speed or the worst case load conditions.

Lee et al. [34] employed a thermal-structural, fully nonlinear ball bearing to evaluate the life of catcher bearings in terms of number of drop occurrences to failure with the Rainflow counting approach. The result shows that decreasing rotor-inner race contact friction, reducing catcher bearing air gap, applying a constant side load after a drop event, reducing support stiffness and increasing support damping, and reducing speed (rpm) all increase the life of an AMB catcher bearing.

10.2.2 Modal reduction

In this study, the rotordynamic system is modeled with finite element method (FEM), using 6 DoFs Timoshenko beam element. With the electronics and flexible support included, the rotordynamic system would have thousands of state variables. Thus solution of the non-condensed equation of motion would require thousands of coupled, ordinary differential equations. In the heteropolar magnetic bearing system

optimization design example, during the optimization iteration, for each population in each generation, one unbalance transient analysis and one startup transient (levitation) analysis are conducted, which requires integration of the ordinary equation twice in each iteration. The computation is expensive even with a small number of rotor finite elements.

Modal reduction, which approximates the behavior of the original large-scale ones with reduced-order models and thus requiring much less computation time, offers a solution to the expensive computation problem. The basic idea of model reduction is to condense a large system to a similar much smaller substitute. According to Noor [35], the good global approximation vectors for model reduction must satisfy

1) Linear independence and completeness.
2) Low computational expense in their generation, and simplicity of automatic selection of their number.
3) Good approximation properties, in the sense of high accuracy of the solution obtained using these vectors.
4) Simplicity of obtaining the system response characteristics using these vectors.

Modal reduction methods have been applied to rotordynamic systems. The commonly used methods include Guyan reduction [36], model reduction by modal analysis [37], component mode synthesis (CMS) [38, 39], and balanced truncation [40, 41].

Guyan reduction, also known as static reduction, is the most popular reduction method. Guyan reduction reduces the system matrices of a system by removing the

DOFs not located at the substructure's boundary. For those remaining DOFs, which at located at the boundary, the stiffness of the local structure are retained, but the inertial terms are omitted to generate a more compact and efficient system. Guyan reduction and is only accurate for stiffness reduction, while the inertial forces are not preserved. Besides, eigenvalues of the reduced system are always higher than those of the original non-reduced system. The quality of the eigenvalue approximation depends on the location of the points preserved in the reduced model, and decreases as the mode number increases.

The modal analysis method of model reduction uses modal coordinates to represent the system and decouple the dynamic system equations of motion. The number of modes to retain is typically selected based on experience and checked by considering whether a convergence of the modal vectors has been reached. The damping ratio is assigned to each mode using measurements or experience data. The frequency can be twice the frequency of interest, or use a middle frequency range. The modally condensed system may include only about 5%-10% of the modes, requiring solution of only a few uncoupled ordinary differential equations compared with the thousands of DOFs coupled ordinary differential equations in the original system.

Component mode synthesis divides the system into smaller structures that are individually designed, analyzed, and then assembled into a full system model for a dynamic analysis. The selections of interface DOFs, the discretization of the full system, and the modes to be retained for each subsystem are determined by the user, similarly to those in a modal analysis method. One main disadvantage of the method is that the final

assembled equations could remain coupled. However, the modal representation in this method is independent of the boundary and interface coordinates. Thus this method is well suited for solving nonlinear supports such as bearings.

Balanced truncation is an important projection model reduction method which delivers high quality reduced models by making an extra effort in choosing the projection subspaces based on the controllability and observability of the system. Only the states or modes that are most observable and controllable are selected. The balanced truncation is based on removing the states of a balanced realization which correspond to singular numbers below a certain threshold. Balance truncation methods have been applied to rotor dynamic systems primarily focused on controller design for the rotor systems. For active magnetic bearings, the balance truncation method could be an effective method for the controller design.

10.2.3 Surrogate modeling

In general, the objective values and the constraint values can be evaluated by an explicit function or a computational simulation. However, in some cases, the evaluations of the objectives and the constraints can be difficult when the genetic algorithms are used to solve expensive optimization problem. The computational simulation for objectives and fitness functions could be very time consuming, or there does not exist an analytical function for them. In such cases, a surrogate modeling might be used to speed up the computation.

A surrogate model is an engineering optimization method that uses approximated surrogate modeling techniques in lieu of expensive experiments and simulations to mimic the behavior of the model to quickly find the local or global optima. The approach is also known as black-box modeling or behavior modeling, since that the inner working of the simulation is not assumed to be known or understood, but only the input-output behavior is important. A comparison between the conventional optimization and the surrogate optimization is presented in Figure 101.

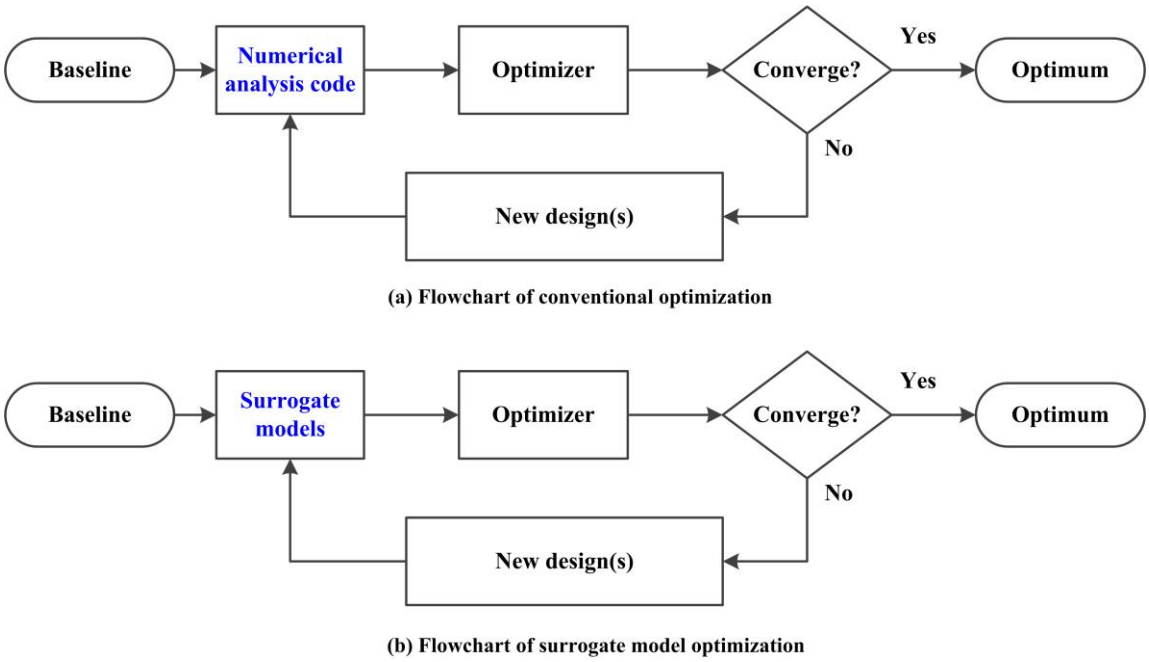

Figure 101 Flowcharts of a conventional optimization and a surrogate model optimization

As has been stated, the magnetic bearing system is complex with large number of variables, highly nonlinear matrix differential equations of large dimension, and complicated constraints of the system. In such cases, surrogate models can be used to

approximate the time consuming objective functions and constraint functions to reduce computation cost, since the prediction with a surrogate model is generally much more efficient than with a numerical analysis code. Once the surrogate models are built, the optimization algorithms, in this study, the NSGA-II or NCGA, can be used to search for the new designs.

This bi-level optimization, with surrogate models to run the expensive analysis code, and with genetic algorithms to determine new samples, is presented in the flowchart in Figure 102.

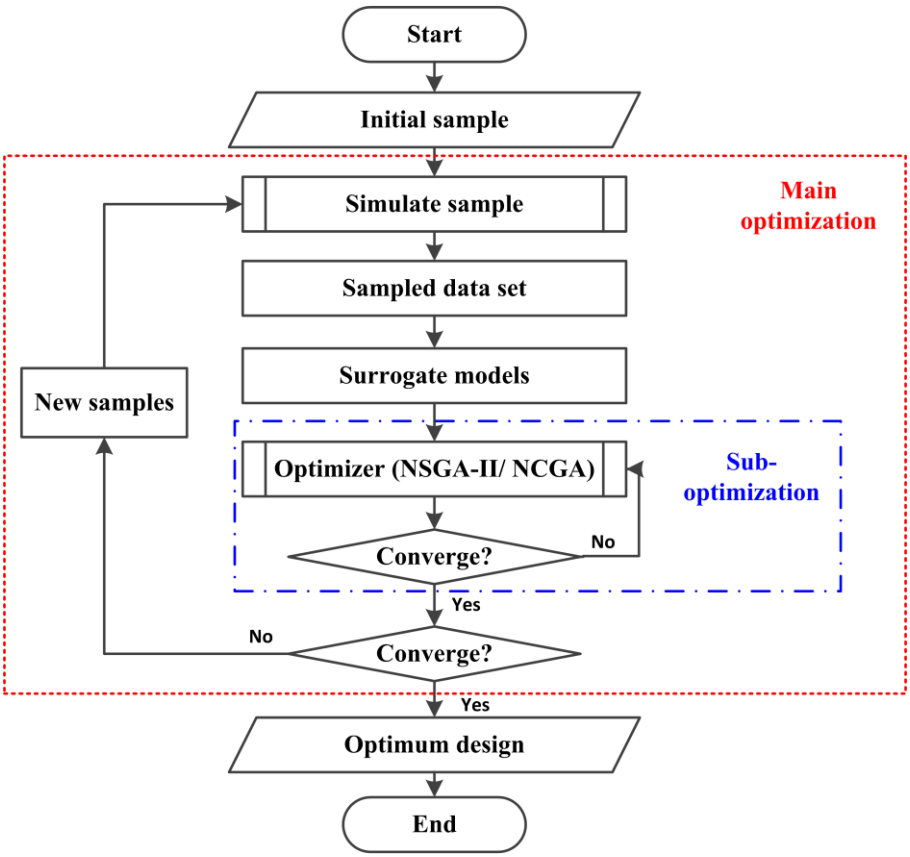

Figure 102 Flowchart of bi-level optimization with surrogate models and genetic algorithms

The process firstly selects the initial sample data from experiments or simulations to be run. Then, the surrogate models are constructed based on the sampled data set. Various techniques can be used to construct the surrogate models. The most popular surrogate models are polynomial response surfaces methodology [42], Kriging (also called DACE, design and analysis of computer experiments) [43], support vector machines [44], space mapping [45], and artificial neural networks [46]. Once the surrogate models are built, an optimizer, in this case, NSGA-II or NCGA can search the surrogate model extensively, since the model is cheap to evaluate. The experiments or simulations are simulated at new locations and added to sample. The process iterates until the code runs out of time or the optimum design is found.

REFERENCES

[1] ISO, Standard. "Mechanical vibration -- Vibration of rotating machinery equipped with active magnetic bearings -- Part 4: Technical guidelines," ISO 14839-4: 2012 (E) (2012).

[2] Chinta, M., and Palazzolo, A., 1998, "Stability and bifurcation of rotor motion in a magnetic bearing," Journal of sound and vibration, 214(5), pp. 793-803.

[3] El Hajjaji, A., and Ouladsine, M., 2001, "Modeling and nonlinear control of magnetic levitation systems," IEEE Transactions on Industrial Electronics, 48(4), pp. 831-838.

[4] Kang, K., and Palazzolo, A., 2012, "Homopolar magnetic bearing saturation effects on rotating machinery vibration," Magnetics, IEEE Transactions on, 48(6), pp. 1984-1994.

[5] Carlson-Skalak, S., Maslen, E., and Teng, Y., 1999, "Magnetic bearing actuator design using genetic algorithms," Journal of Engineering Design, 10(2), pp. 143-164.

[6] Shelke, S., and Chalam, R., 2011, "Optimum Power Loss Analysis of Radial Magnetic Bearing using Multi-Objective Genetic Algorithm," International Journal of Computer Applications, 27(6).

[7] Chang, H., and Chung, S.-C., 2002, "Integrated design of radial active magnetic bearing systems using genetic algorithms," mechatronics, 12(1), pp. 19-36.

[8] Schroder, P., Green, B., Grum, N., and Fleming, P., 2001, "On-line evolution of robust control systems: an industrial active magnetic bearing application," Control Engineering Practice, 9(1), pp. 37-49.

[9] Chen, H.-C., "Optimal fuzzy pid controller design of an active magnetic bearing system based on adaptive genetic algorithms," Proc. Machine Learning and Cybernetics, 2008 International Conference on, IEEE, pp. 2054-2060.

[10] Chen, H.-C., "Adaptive genetic algorithm based optimal PID controller design of an active magnetic bearing system," Proc. Innovative Computing Information and Control, 2008. ICICIC'08. 3rd International Conference on, IEEE, pp. 603-603.

[11] Chang, L.-Y., and Chen, H.-C., 2009, "Tuning of fractional PID controllers using adaptive genetic algorithm for active magnetic bearing system," WSEAS Transactions on systems, 8(1), pp. 158-167.

[12] Jastrzębski, R. P., and Pöllänen, R., 2009, "Centralized optimal position control for active magnetic bearings: comparison with decentralized control," Electrical Engineering, 91(2), pp. 101-114.

[13] Hsiao, F. Z., Fan, C. C., Chieng, W. H., and Lee, A. C., 1996, "Optimum magnetic bearing design considering performance limitations," Jsme Int J C-Dyn Con, 39(3), pp. 586-596.

[14] Lee, A.-C., Hsiao, F.-Z., and Ko, D., 1994, "Performance limits of permanent-magnet-biased magnetic bearings," JSME international journal. Ser. C, Dynamics, control, robotics, design and manufacturing(4), pp. 783-794.

[15] Fan, Y.-H., Lee, A.-C., and Hsiao, F.-Z., 1997, "Design of a permanent/electromagnetic magnetic bearing-controlled rotor system," Journal of the Franklin Institute, 334(3), pp. 337-356.

[16] Deb, K., Pratap, A., Agarwal, S., and Meyarivan, T., 2002, "A fast and elitist multiobjective genetic algorithm: NSGA-II," Evolutionary Computation, IEEE Transactions on, 6(2), pp. 182-197.

[17] Zitzler, E., Laumanns, M., Thiele, L., Zitzler, E., Zitzler, E., Thiele, L., and Thiele, L., 2001, "SPEA2: Improving the strength Pareto evolutionary algorithm," Eidgenössische Technische Hochschule Zürich (ETH), Institut für Technische Informatik und Kommunikationsnetze (TIK).

[18] Watanabe, S., Hiroyasu, T., and Miki, M., "NCGA: Neighborhood Cultivation Genetic Algorithm for Multi-Objective Optimization Problems," Proc. GECCO Late Breaking Papers, pp. 458-465.

[19] Coello Coello, C. A., and Lechuga, M. S., "MOPSO: A proposal for multiple objective particle swarm optimization," Proc. Evolutionary Computation, 2002. CEC'02. Proceedings of the 2002 Congress on, IEEE, pp. 1051-1056.

[20] Nam, D., and Park, C. H., 2000, "Multiobjective simulated annealing: A comparative study to evolutionary algorithms," International Journal of Fuzzy Systems, 2(2), pp. 87-97.

[21] Schweitzer, G., and Maslen, E. H., 2009, "Magnetic bearings: theory, design and application to rotating machinery (POD)."

[22] Gen, M., and Cheng, R., 2000, Genetic algorithms and engineering optimization, John Wiley & Sons.

[23] Sivaraj, R., and Ravichandran, T., 2011, "A review of selection methods in genetic algorithm," International Journal of Engineering Science and Technology (IJEST), 3(5), pp. 3792-3797.

[24] Haupt, R. L., and Werner, D. H., 2007, Genetic algorithms in electromagnetics, John Wiley & Sons.

[25] Lei, S. L., and Palazzolo, A., 2008, "Control of flexible rotor systems with active magnetic bearings," Journal of Sound and Vibration, 314(1-2), pp. 19-38.

[26] Vázquez, J. A., Barrett, L. E., and Flack, R. D., 2002, "Flexible bearing supports, using experimental data," Journal of Engineering for Gas Turbines and Power, 124(2), pp. 369-374.

[27] Barrett, L. E., and Flack, R. D., 2001, "A flexible rotor on flexible bearing supports: stability and unbalance response." Journal of vibration and acoustics 123.2 (2001): 137-144.

[28] Nicholas, J. C., Whalen, J. K., and Franklin, S. D., "Improving critical speed calculations using flexible bearing support FRF compliance data," Proc. Proceedings of the 15th Turbomachinery Symposium, pp. 69-78.

[29] Kasarda, M. E., 1997, Dissertation, "The measurement and characterization of power losses in high speed magnetic bearings," University of Virginia, Charlottesville, VA.

[30] Carpenter Technology, "Magnetic Alloys," C. Technology, ed., Carpenter Technology Reading, PA, 19612.

[31] Standard, A.P.I, 2004, "617, 2002,“," Axial and Centrifugal Compressors and Expander-Compressors for Petroleum, Chemical and Gas Industry Services,” Seventh Edition, American Petroleum Institute, Washington, DC.

[32] Standard, I.S.O, "Mechanical vibration-Vibration of rotating machinery equipped with active magnetic bearings-part 2: Evaluation of vibration." ISO 14839-2: 2006 (E) (2004).

[33] Standard, I.S.O,"Mechanical vibration-Vibration of rotating machinery equipped with active magnetic bearings-part 3: Evaluation of stability margin." ISO 14839-3: 2006 (E) (2004).

[34] Lee, J. G., and Palazzolo, A., 2012, "Catcher bearing life prediction using a rainflow counting approach," Journal of Tribology, 134(3), p. 031101.

[35] Noor, A. K., 1994, "Recent advances and applications of reduction methods," Applied Mechanics Reviews, 47(5), pp. 125-146.

[36] Guyan, R. J., 1965, "Reduction of stiffness and mass matrices," AIAA Journal, 3(2), pp. 380-380.

[37] Shaw, S. W., and Pierre, C., 1999, "Modal Analysis-Based Reduced-Order Models for Nonlinear Structures— An Invariant Manifold Approach," The Shock and Vibration Digest, 31(1), pp. 3-16.

[38] Craig Jr, R. R., 1985, "A review of time-domain and frequency-domain component mode synthesis method." Combined Experimental/Analytical Modeling of Dynamic Structural Systems (1985): 1-30.

[39] Glasgow, D., and Nelson, H., 1980, "Stability analysis of rotor-bearing systems using component mode synthesis," Journal of Mechanical Design, 102(2), pp. 352-359.

[40] Safonov, M., and Chiang, R., 1989, "A Schur method for balanced-truncation model reduction," IEEE Transactions on Automatic Control, 34(7), pp. 729-733.

[41] Moore, B., 1981, "Principal component analysis in linear systems: Controllability, observability, and model reduction," IEEE Transactions on Automatic Control, 26(1), pp. 17-32.

[42] Box, G. E., and Wilson, K., 1951, "On the experimental attainment of optimum conditions," Journal of the Royal Statistical Society. Series B (Methodological), 13(1), pp. 1-45.

[43] Lophaven, S. N., Nielsen, H. B., and Søndergaard, J., 2002, "DACE-A Matlab Kriging toolbox, version 2.0."

[44] Cortes, C., and Vapnik, V., 1995, "Support-vector networks," Machine Learning, 20(3), pp. 273-297.

[45] Bandler, J. W., Cheng, Q. S., Dakroury, S. A., Mohamed, A. S., Bakr, M. H., Madsen, K., and Sondergaard, J., 2004, "Space mapping: the state of the art," IEEE Transactions on Microwave Theory and Techniques, 52(1), pp. 337-361.

[46] McCulloch, W. S., and Pitts, W., 1943, "A logical calculus of the ideas immanent in nervous activity," The Bulletin of Mathematical Biophysics, 5(4), pp. 115-133.